Bose-Einstein condensation in higher Bloch bands of the optical honeycomb lattice

DISSERTATION

zur Erlangung des Doktorgrades

an der Fakultät für Mathematik, Informatik und Naturwissenschaften

im Fachbereich Physik

der Universität Hamburg

vorgelegt von

Tobias KLAFKA

Hamburg

2021

Gutachter der Disputation:	Prof. Dr. Klaus Sengstock Prof. Dr. Andreas Hemmerich Prof. Dr. Ludwig Mathey Prof. Dr. Henning Moritz Prof. Dr. Markus Drescher
Vorsitzender der Prüfungskommission:	Prof. Dr. Ludwig Mathey
Datum der Disputation:	20.08.2021
Vorsitzender des Promotionsausschusses Physik:	Prof. Dr. Wolfgang Hansen
Leiter des Fachbereichs Physik:	Prof. Dr. Günter H. W. Sigl
Dekan der Fakultät für Mathematik, Informatik und Naturwissenschaften:	Prof. Dr. Heinrich Graener

Abstract

Ultracold quantum gases in optical lattices provide a versatile platform for quantum simulations of solid state models. Preparing higher Bloch bands of optical lattices enlarges immensely the possibilities for realizations of unconventional superfluids emerging from the interplay of orbital degrees of freedom and lattice geometries.
This thesis reports on the experimental realization of Bose-Einstein condensation in the second and fourth Bloch band of the optical 2D-honeycomb lattice with ^{87}Rb. Reaching higher bands is an intrinsic out-of-equilibrium process that requires the transfer of a significant amount of energy. For that purpose different transfer methods have been tested. A Landau-Zener transfer has been realized by a rapid quench of the energy offset between the two sublattices of the honeycomb lattice.

The condensation dynamics in higher bands is intriguing due to the different geometries of the excited bands. The preparation of a many-body wave packet is especially interesting at the maximum of a band, where the initial dynamical evolution is dominated by interactions between the atoms. Consequently, the observed time scales for the condensation and subsequent loss of coherence depend crucially on the collision rates. At the optimal parameters, the loss of coherence is followed by band relaxation to the ground state on a longer time scale. The parameter space in the second and in the fourth Bloch band is explored for optimal condensation. The experimental results contribute to the engineering of unconventional superfluids with interaction-induced topological ordering.
Furthermore, three major upgrades were realized in the course of this PhD project. First, a Λ-enhanced gray molasses cooling was implemented reaching a temperature of $5.3(4)\,\mu$K and shortening the experimental cycle by 10 s. Second, a new intensity control for the optical honeycomb lattice with a bandwidth of $\sim$ 150 kHz was realized to investigate higher Bloch bands. Third, an active magnetic field compensation for quantum gas experiments was implemented. Using an anisotropic magnetoresistive sensor (AMR) in combination with an analogue control loop stabilized the magnetic field to $\sim$100 µG from DC up to frequencies of 3 kHz. Ramsey spectroscopy demonstrated a reduction of magnetic field fluctuations down to $\sigma = 130\,\mu$G. This technique will prove valuable for future experiments such as the realization of spin-orbit coupling involving the atomic internal degree of freedom.

Zusammenfassung

Ultrakalte Quantengase in optischen Gittern bieten eine vielseitige Plattform für Quantensimulationen von Festkörpermodellen. Die Präparation von höheren Blochbändern in optischen Gittern vergrößert beträchtlich die Möglichkeiten zur Realisierung von unkonventionellen suprafluiden Zuständen, die durch das Zusammenspiel von orbitalen Freiheitsgraden und der Gittergeometrien entstehen.

Diese Arbeit widmet sich der experimentellen Realisierung von Bose-Einstein Kondensation im zweiten und vierten Blochband des optischen 2D-Honigwabengitters mit ^{87}Rb. Das Erreichen von höheren Bändern ist ein intrinsischer Nichtgleichgewichtsprozess, der einen signifikanten Energietransfer benötigt. Für diesen Transfer wurden verschiedene Methoden getestet. Ein Landau-Zener Transfer wurde durch eine schnelle Veränderung der Energiedifferenz zwischen den beiden Subgittern des Honigwabengitters realisiert.

Die Kondensationsdynamik in höheren Blochbändern ist aufgrund der unterschiedlichen Bandgeometrien faszinierend. Besonders interessant ist die Präparation eines Vielteilchenwellenpaketes am Maximum eines Bandes, wo die anfängliche dynamische Entwicklung durch die Wechselwirkung zwischen den Atomen dominiert wird. Folglich sind die beobachteten Zeitskalen für die Kondensation als auch für den nachfolgenden Verlust der Kohärenz entschieden von den Kollisionsraten abhängig. Auf den Verlust der Kohärenz folgt die Bandrelaxation in den Grundzustand, die bei den optimalen Parametern über einen längeren Zeitraum stattfindet. Der Parameterraum im zweiten und vierten Band wird auf optimale Kondensation durch die Kontrolle der Bandstruktur untersucht. Die experimentellen Ergebnisse tragen zur Erforschung von unkonventionellen suprafluiden Zuständen mit wechselwirkungsinduzierten topologischen Ordnungen bei.

Darüber hinaus wurden im Rahmen dieses Dissertationsprojektes drei wichtige Verbesserungen am Experiment realisiert. Erstens wurde eine Λ-verstärkte Graue-Melassen-Kühlung implementiert, mit der eine Temperatur von $5.3(4)\,\mu$K und eine Verkürzung des experimentellen Zyklus um 10 s erreicht wurde. Zweitens wurde eine neue Intensitätsregelung für das optische Gitter mit einer Bandbreite von $\sim$ 150 kHz zur Untersuchung von höheren Blochbändern realisiert. Drittens wurde eine aktive Magnetfeldkompensation für Quantengasexperimente implementiert. Die Verwendung eines anisotropen magnetoresistiven Sensors (AMR) in Kombination mit einer analogen Regelung konnte das Magnetfeld auf $\sim$100 µG von DC bis zu Frequenzen von 3 kHz stabilisieren. Mit Ramsey Spektroskopie konnte eine Reduktion der Magnetfeldfluktuationen auf bis zu $\sigma = 130\,\mu$G gezeigt werden. Diese Technik ist für zukünftige Experimente, wie die Realisierung von Spin-Orbit Kopplung unter Einbeziehung des atomaren internen Freiheitsgrades, wertvoll.

Contents

Chapter 1

Introduction

Ultracold quantum gases offer versatile flexibility and controllability providing an attractive system for the simulation of quantum models. Since the first experimental realization of Bose-Einstein condensates (BEC) in 1995 [1–3], the field of ultracold quantum gases experienced a tremendous growth. Examples for seminal experiments include collective excitations [4, 5], interference of two condensates [6], long-range phase coherence [7] and vortices [8–10]. Equally important is the first realization of Fermi degeneracy [11] and the investigation of the BEC to BCS (Barden-Cooper-Schrieffer) crossover [12–14].

While optical lattices created by a standing light wave of interfering laser beams were already realized with cold atoms [15–17], the realization of ultracold quantum gases allowed for entering of the quantum many-body regime. Loading adiabatically a BEC into the ground state of an optical lattice constitutes an implementation of the Bose-Hubbard model [18], leading to the observation of the quantum phase transition from a superfluid to Mott-insulating state [19]. Since then a great number of experiments have exploited the variety of optical lattices as for example in terms of dimensionality, geometry, intensity, frequency or phase [20–23].

Preparing quantum gases in higher bands of optical lattices constitutes a unique method to bypass the no-node theorem of Feynman and to access the orbital degree of freedom [24]. This allows for the realization of unconventional superfluids with exotic properties [25, 26] such as quantum stripe ordering [27] or interaction-induced topological states [28]. States like these are challenging to prepare due to their metastable nature. Early experiments observed a coherent population transfer to higher bands for instance via lattice acceleration [29] or stimulated Raman transitions [30]. So far, the preparation of long-lived superfluid states has only been successful in the 2D bipartite square lattice by realizing a sudden quench of the unit cell [31–33]. Particularly intriguing is the formation of a superfluid at nonzero quasi-momenta in the second band [31] whose lifetime is determined by the rate of elastic collisions [34]. This remarkable state is characterized by a chiral superfluid order [35]. Its longevity originates from destructive quantum interference of two principal decay channels [36].

Despite this success, the preparation of metastable states in higher bands has so far remained largely unexplored in other lattice geometries. The central scope of this thesis is to bridge this gap for the bipartite hexagonal lattice, which constitutes an ideal candidate for unconventional superfluids with exotic properties as for instance the recently published Potts-nematic phase [37].

The transfer mechanism to higher bands relies on a rapid quench of the energy offset between the two sublattices of the bipartite hexagonal lattice. The energy offset can be controlled by a rotation of a magnetic field [38]. In seminal experiments the continuous tuning of the energy gap at the Dirac cones between the first and second band has been demonstrated [39]. Within this PhD project a time-dependent tuning of the energy offset has been implemented to populate higher Bloch bands by a Landau-Zener type transfer.

We have observed the formation of superfluid states in higher bands of the hexagonal lattice. One fascinating feature is the emergence of coherence in the second band where condensation occurs at non-zero quasimomenta. It is interesting to compare this with the condensate formation in the fourth band where the superfluid is realized at zero quasimomentum. Additionally, we have explored the lifetime of such superfluid states over a large parameter space of lattice configurations (i.e. lattice depth and energy offset) and have identified the key ingredients for the formation of superfluids in higher bands. These results pave the way towards tailoring states with rectified orbital angular momentum.
This thesis is structured in the following way:

- **Chapter 2** presents the experimental apparatus together with major upgrades implemented in the course of this PhD project. This chapter describes the implementation of Λ-enhanced gray molasses cooling for ^{87}Rb and the characterization of an active magnetic field compensation by Ramsey spectroscopy.

- **Chapter 3** introduces the optical potentials i.e. the dipole trap and the versatile optical lattice setup with a focus on the bipartite hexagonal lattice. The energy offset between the two sublattices of the hexagonal lattice and the measured harmonic confinement are pointed out, which are central for the preparation of higher bands. Further, the detection methods, time-of-flight and band mapping, are discussed. A high bandwidth intensity control together with an investigation of phase noise at the laser setup is presented.

- **Chapter 4** presents different transfer methods to higher Bloch bands. One implemented transfer method relies on a Landau-Zener type process by a rapid tuning of the energy offset between the two sublattices. Its experimental implementation by rotating the quantization axis is explained. The measured transfer efficiency exploring the parameter space for different lattice depths and energy offsets between the sublattices is discussed in detail.

- **Chapter 5** reports on the realization of Bose-Einstein condensates in the second and in the fourth Bloch band and analyzes the condensation dynamics at the optimal parameters. The parameter space controlling the band structure is explored in the second and in the fourth Bloch band for optimal condensation. The experimental results are compared to the bipartite square lattice and the key ingredients for condensation like lattice dimensionality and critical temperature are discussed. Finally, the precise tuning of the positions of the minima in the second band is investigated by the relative intensity between the lattice beams.

The experimental work presented in this thesis has been performed by the author in collaboration with his fellow PhD students Alexander Ilin and Julius Seeger, with the master's students Mario Großmann and Phillip Groß and with the support of several Bachelor students and student assistants. This PhD project has been conducted under supervision of Juliette Simonet and Klaus Sengstock, the principal investigators of the experiment. Works on a theoretical description of the condensation in higher Bloch bands of the hexagonal lattice are continuing in collaboration with Georgios Koutentakis, Simos Mistakidis and Peter Schmelcher.

Chapter 2

Experimental setup for a spinor BEC

In this chapter we present the experimental apparatus together with major experimental upgrades, which were implemented in the course of this PhD project. Noteworthy here is the implementation of a Λ-enhanced gray molasses for ^{87}Rb on the D_2-transition with a temperature of $5.3(4)$ µK. This resulted in a significantly shorter experimental cycle time, which we could reduce to 23 s. Further, we summarize how to switch the between the internal states $F = 1$ and $F = 2$ and between the different Zeeman sublevels, as these techniques are central in this thesis. Finally, we present the implementation of an active magnetic field compensation. It has been accurately characterized using Ramsey spectroscopy, which is a precise method to probe magnetic fields with quantum gases. The work presented in this chapter has been conducted with main contributions by the author. The collaborators are named in the introductory sections of the different projects.

2.1 Preparation of a spinor condensate

2.1.1 Experimental apparatus

The work in this thesis has been carried out at a quantum gas machine for ^{87}Rb. The first Bose-Einstein condensates have been realized by H. Schmaljohann [40] and M. Erhard [41]. Thereafter further experimental upgrades and many experiments have been pursued during the PhD theses of J. Kronjäger, C. Becker, P. Soltan-Panahi, J. Struck, M. Weinberg and C. Ölschläger [42–47].

The main setup consists of two glass cells, which are vertically connected via a differential pumping stage. The upper glass cell contains four dispensers. However, after about 15 years of operation the original dispensers had to be replaced at the beginning of this PhD project. Therefore, we flooded the apparatus with Argon, lifted off the upper glass cell and replaced the dispensers by two new Rubidium[1] and two Potassium dispensers[2]. We reached the original operational background pressures within 8 weeks. With ion-getter pumps the background pressure in the

[1]SAES: RB/NF/4.8/17 FT10+10
[2]SAES: K/NF/3.1/17 FT10+10, intended for the production of ^{39}K-BECs.

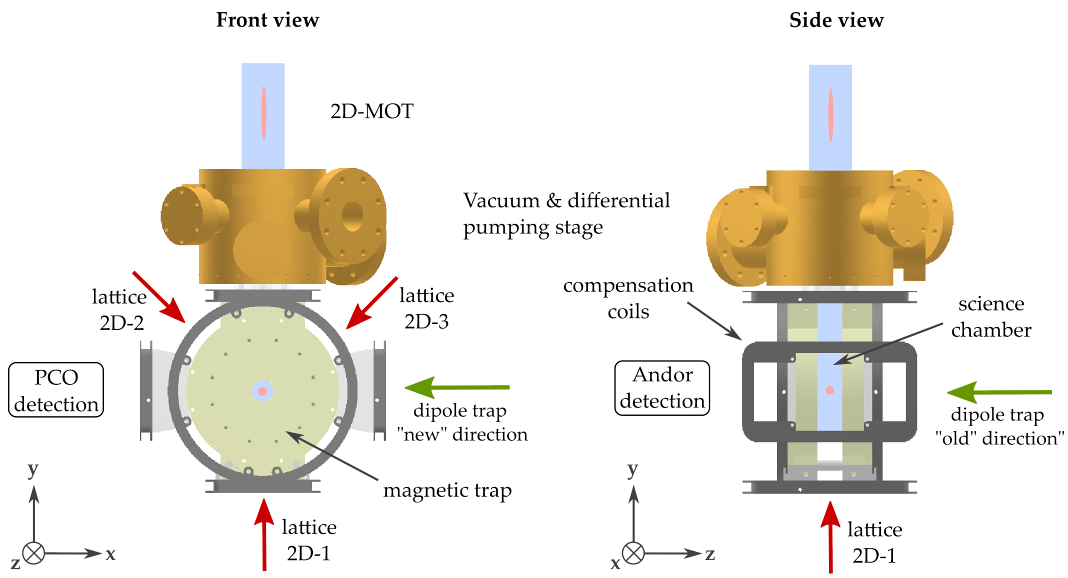

FIGURE 2.1: Front and side view of the experimental setup. From the 2D-MOT in the upper glass cell atoms are transferred through the differential pumping stage to the lower glass cell to a 3D-MOT. Further cooling steps are performed to obtain a Bose-Einstein condensate in the crossed dipole trap. In a typical experiment the BEC is then loaded into the optical honeycomb lattice, which consists of three overlapping Gaussian laser beams. Via absorption imaging after time-of-flight we can detect the atoms orthogonally to the lattice plane (Andor camera) or in-plane (PCO camera).

upper glass cell is kept at about 1×10^{-9}mbar and in the lower glass cell below 1×10^{-11}mbar to maintain an ultrahigh vacuum.

During operation a current of 5 A flows through one ^{87}Rb-dispenser, which emits atoms in the upper glass cell. From this background vapor a cigar-shaped two dimensional magneto-optical trap (2D-MOT) is loaded. With a near-resonant pushing beam ^{87}Rb-atoms are transferred through the differential pumping stage to the lower glass cell where they are captured in a 3D-MOT. After a typical loading time of 12 s we reach an atom number of about 3.8×10^8 and a temperature of about 420 µK. Subsequently, we employ a bright molasses phase with a final temperature of 25 µK. Towards the end of this PhD project this phase has been replaced with gray molasses (section 2.2) bringing the advantage of a significant shorter cycle time and more robustness against MOT-fluctuations. After the molasses phase, the atomic cloud in the state $|F = 1, m_F = -1\rangle$ is loaded into a magnetic 4-dee/cloverleaf trap [41, 48]. Here, forced radio-frequency evaporation over 15 s is performed to further cool the atomic gas. In the last cooling step towards quantum degeneracy, the atoms are transferred to a crossed elliptical dipole trap (XDT) in, which forced evaporative cooling takes place for 6 s. Depending on initial particle numbers and final XDT intensities with typical trap frequencies of $\omega_{x,y,z} = 2\pi \times (20, 50, 20)$ Hz, we can tune the atom number between 80k and 400k. As these values are crucially important for some of the presented experiments, the main characteristics of the dipole trap are further discussed in chapter 3. As the research conducted at the project focuses on optical lattices, versatile lattice geometries in 1D, 2D or 3D are available. Detection

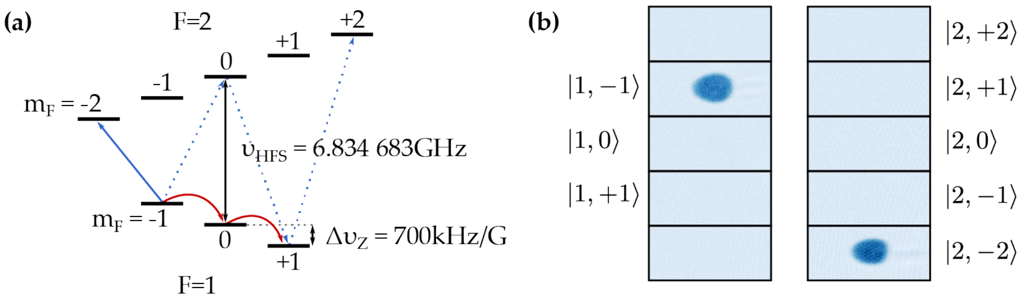

FIGURE 2.2: Spin state preparation. (a) A quantization field lifts the Zeeman degeneracy of hyperfine splitting of the $5^2S_{1/2}$ level. From the initial state $|1,-1\rangle$ we usually use a Landau-Zener sweep to $|1,-1;0\rangle$ (red) or $|2,-2\rangle$ (blue). The blue dotted transitions are also possible. (b) For probing the different sublevels we take absorption images after Stern-Gerlach separation and time-of-flight of the BEC.

is performed with absorption imaging after time-of-flight (TOF) along two different imaging axes. A sketch of the experiment is presented in figure 2.1.

2.1.2 Spin state preparation

At the end of the experimental cycle we obtain a spin-polarized BEC in the state $|F = 1, m_F = -1\rangle$ in the crossed dipole trap. For many experiments presented in this thesis changing this initial spin state has been a crucial requirement. Here, we have used mainly two methods, which were already implemented at the experiment [40–42]: microwave and radio frequency driven transitions.

The microwave transition is used to transfer the BEC between the hyperfine levels $F = 1$ and $F = 2$. The degeneracy of the m_F-sublevels is lifted by a quantization field. If the separation is large enough, which is the case for the used field strengths throughout this thesis of 1.1 G and 2.2 G, the different m_F-sublevels can be addressed specifically ($\Delta m_F = \pm 1$). Typically, we perform a Landau-Zener sweep for the transition from $|F = 1, m_F = -1\rangle$ to $|F = 2, m_F = -2\rangle$. A microwave source generates a 2 ms pulse at the hyperfine splitting $\nu_{HFS} \sim 6.8\,$GHz to which a modulation by a versatile frequency generator is added. In contrast to π-pulses for state preparation, Landau-Zener sweeps assure a high fidelity as they are less sensitive to magnetic field fluctuations [49].

For transitions between the m_F-sublevels we apply the same technique but in the radio frequency regime as the level separations are on the order of $\Delta\nu_Z = 700\,\mathrm{kHz/G}$. The spin-state preparation is illustrated in figure 2.2.

2.2 Implementation of gray molasses for ^{87}Rb

Laser cooling is the first step essential to obtain quantum degeneracy. While it was first believed that the Doppler limit $T_D = \hbar\Gamma/2k_B \simeq 146\,\mu$K (for ^{87}Rb) provided a fundamental limit, it was soon discovered that far lower temperatures could be reached [50]. This results from the interplay of atomic levels and the polarization of the light field, which is called Sisyphus cooling [51]. Atoms repeatedly climb up a potential hill loosing kinetic energy. At the top of the hill they have a higher probability to be optically pumped and reach a lower lying state where the process begins again.

Making use of Sisyphus cooling at our experiment we have implemented a bright molasses phase where we reach temperatures as low as 25 µK. This is still almost by a factor 70 larger than the recoil temperature $T_r = \hbar k^2/2mk_B \simeq 362\,\mathrm{nK}$ due to heating from spontaneous emission. Nevertheless, the temperature and the reached corresponding phase-space density allow for substantially reducing the duration of the BEC cycle. Still, spontaneous emission can be further reduced with different cooling schemes, which have already been proposed in the 90's. They make use of dark states being decoupled from light [52–55]. But as often also bright states are involved the term gray molasses is used. Especially in the last decade advances were pushed forward as light elements like ^{6}Li require efficient cooling schemes. Inspired by the substantial advantages of gray molasses in the Λ-scheme with elements like ^{4}He [56], ^{6}Li [57, 58] , ^{7}Li [59] or ^{39}K [60, 61], ^{40}K [58, 62], ^{41}K [63], we have implemented gray molasses to reach lower temperatures and higher phase-space densities (PSD), to eventually achieve a short cycle time of the experiment for data-intensive measurements.

Typically, gray molasses with alkali atoms have been implemented on the D_1 transition as the hyperfine energy splitting of the D_2 transition (e.g. ^{6}Li) is on the same order as the linewidth. Therefore, closed transitions are not possible. However, for ^{87}Rb this is not the case. A recent publication from Rosi et. al. [64] showed that the implementation of Λ-enhanced gray molasses on the D_2-transition of ^{87}Rb is possible with an increase by a factor of 10 in phase-space density. As we already use the D_2-transition for laser cooling, gray molasses cooling can be implemented in our experimental setup without requiring an additional laser. The experimental work presented in this section has been performed by R. Conrad, P. Groß and A. Ilin and the author of this thesis. Further information can be found in the Bachelor's thesis of R. Conrad [65].

A model system capturing qualitatively many features is the Λ-system consisting of two ground states g_1, g_2 and an excited state e (cf. figure 2.3). Two phase-coherent lasers can couple the two ground states g_1 and g_2 via the excited state e. From the Bloch equations an analytic expression for the steady state solution can be derived [66, 67]. Here we give the population of the excited state ρ_{ee}

$$\rho_{ee} = \frac{4(\Delta_1 - \Delta_2)^2 \Omega_1^2 \Omega_2^2 \Gamma}{Z} \tag{2.1}$$

where

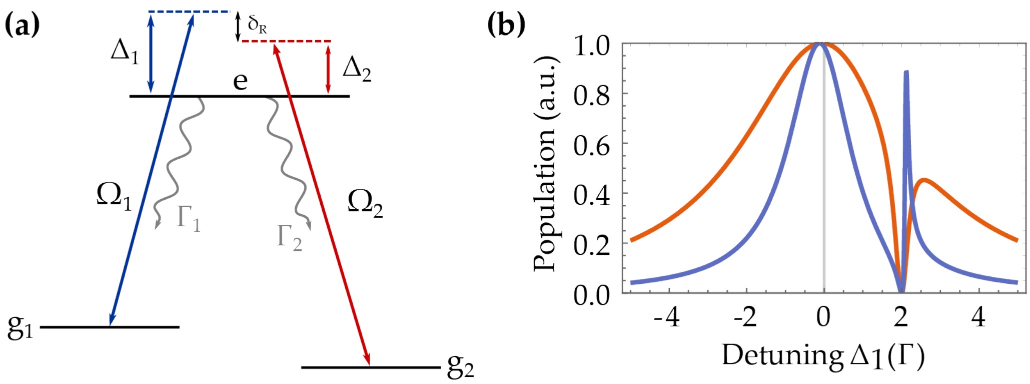

FIGURE 2.3: (a) Model system of the Λ-scheme. It consists of the two ground states g_1 and g_2 and the excited state e. The transition from g_1 (g_2) to e is characterized by the Rabi coupling Ω_1 (Ω_2) with a detuning Δ_1 (Δ_2) from e. Γ_1 and Γ_2 denote the spontaneous decay to the ground states. (b) The population of the excited state varies as a function of the detuning Δ_1. Two cases are plotted: equal Rabi frequency $\Omega_1 = \Omega_2 = 1$, $\Delta_2 = 2$ (red curve) and $\Omega_1 = 0.1, \Omega_2 = 1, \Delta_2 = 2$ (blue curve). At a Raman detuning $\delta_R = \Delta_1 - \Delta_2 = 0$ the absorption amplitudes from g_1 to e and g_2 to e interfere destructively. The population of the excited state is zero.

$$
\begin{aligned}
Z = {} & 8(\Delta_1-\Delta_2)^2\Omega_1^2\Omega_2^2\Gamma + 4(\Delta_1-\Delta_2)^2\Gamma^2(\Omega_1^2\Gamma_2+\Omega_2^2\Gamma_1) \\
& + 16(\Delta_1-\Delta_2)^2(\Delta_1^2\Omega_2^2\Gamma_1+\Delta_2^2\Omega_1^2\Gamma_2) - 8\Delta_1(\Delta_1-\Delta_2)\Omega_2^4\Gamma_1 \\
& + 8\Delta_2(\Delta_1-\Delta_2)\Omega_1^4\Gamma_2 + (\Omega_1^2+\Omega_2^2)^2(\Omega_1^2\Gamma_2+\Omega_2^2\Gamma)
\end{aligned}
\tag{2.2}
$$

with the Rabi frequency Ω_1, Ω_2, the detuning from e being Δ_1, Δ_2.

If the Raman condition is fulfilled $\delta_R = \Delta_1$ - $\Delta_2 = 0$, the amplitudes of the transition from g_1 to e and from g_2 to e interfere destructively. Then the atom is decoupled from light. A so-called dark state is created, which can be expressed as a linear superposition of g_1 and g_2. The corresponding population of the excited state in eq. (2.1) is displayed in figure 2.3.

Two cases can be distinguished. When the detuning Δ_1 is varied, while $\Delta_2 = 2\,\Gamma$ and the Rabi frequencies Ω_1 and Ω_2 are equal, the excited state is populated for $\Delta_1 \to 0$. When Δ_1 approaches Δ_2, the two ground states are coupled and for the Raman condition the excited state is completely depopulated. Thus, matching the Raman condition plays a crucial role in the cooling mechanism. For a given detuning $\Delta_{1,2}$ one can select different velocity classes of the atoms. However, experimentally the Rabi frequencies are often strongly different, here $\Omega_1 \gg \Omega_2$. This results in a strongly asymmetric profile where at the Raman condition a Fano type profile arises. This has been proven by Lounis et. al. [67] and is in good agreement with the experimental data. Further explanations can be found in Bardou et. al [68]. In Grier et. al [69] a more complete calculation of the cooling force is given.

A more thorough description of gray molasses relies on the combination of two

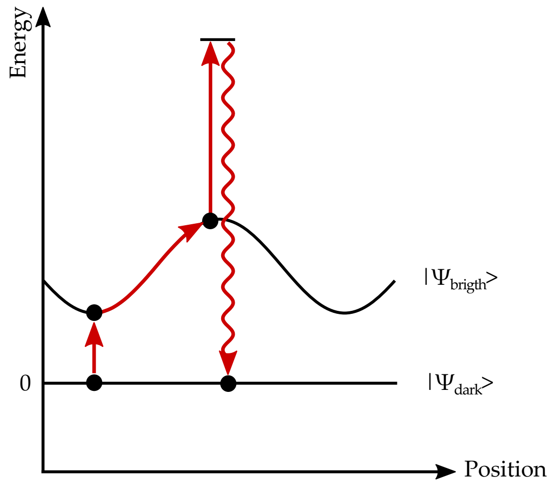

FIGURE 2.4: Principle of gray molasses. An atom in the dark state experiencing no light shift couples via motional coupling to a bright state with a blue detuned spatial light shift. After climbing up the potential hill an atom is optically pumped to the dark state loosing kinetic energy.

effects: velocity-selective-coherent-population-transfer (VSCPT) and Sisyphus cooling. During VSCPT atoms perform a random walk in velocity space and can eventually end up in the dark state, which is decoupled from light. The time an atom stays in the dark state is proportional to the inverse of its momentum squared. Combining this effect with Sisyphus cooling, Cohen Tannoudjii proposed the following picture: atoms in the dark state are repeatedly transferred via motional coupling to the bright state where they climb up the potential hills. Near the top of the hill they have a higher probability of being pumped to a dark state as illustrated in figure 2.4. A complete description of gray molasses with alkali atoms is challenging due to the complicated polarization pattern in the experiment, the hyperfine structure and the numerous Zeeman sublevels involved.

2.2.1 Experimental implementation

The magneto-optical trap (MOT) precedes the gray molasses phase in the experimental cycle. The MOT phase consists of three stages of 3 s, 4 s and 5 s duration whose main difference is the decreasing intensity of the cooling light and the pushing beam. At the end of the MOT-phase we typically reach an atom number of $(3.72 \pm 0.14) \times 10^8$ and a temperature of (418.0 ± 30.8) µK. After switching-off the magnetic fields (1 ms), we have previously run a bright molasses phase where we reached a temperature of (25.2 ± 0.3) µK and a phase-space density of $(18.29 \pm 1.35) \times 10^{-6}$. This has been replaced by a gray molasses phase whose implementation is inspired by the recent publication by Rosi et al. [64].

For the cooler we use a diode laser, which is frequency shifted with double-pass acousto-optical modulators (AOM) to the desired frequency as shown in figure 2.5.

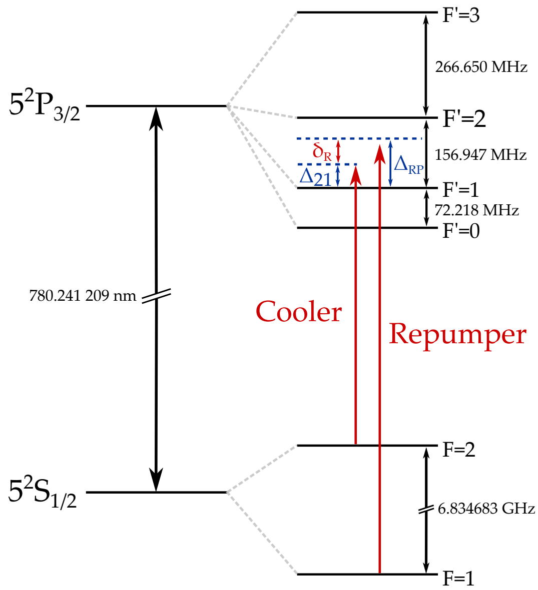

FIGURE 2.5: Energy level scheme of the D_2 transition of ^{87}Rb. We have implemented the Λ-scheme between the hyperfine levels $F = 1$ and $F = 2$ via coupling to the excited state $F' = 1$. The cooler (repumper) is blue-detuned Δ_{21} (Δ_{RP}) to the excited state. The Raman condition is given by $\delta_R = \Delta_{RP} - \Delta_{21}$. For experimental reasons we use the excited state $F' = 1$ instead of $F' = 2$ as reported in [64], but we observe no significant differences in the performance. Level splitting is adapted from [70].

The repumper is generated with an electro-optical modulator (EOM)[3]. It modulates small-amplitude sidebands onto the laser beam near the hyperfine splitting $F = 1$ and $F = 2$ at 6.83 GHz. This implementation guarantees the phase-coherence between the two laser beams, which is essential for the Λ scheme and for reaching very low temperatures.

For characterization we used absorption imaging after time-of-flight. As the magnification of the objective in place is too large for imaging gray molasses, we setup temporarily an objective with a magnification of 0.42. The atomic clouds were fitted with Gaussians to extract their size and temperature via

$$\sigma(t) = \sqrt{\sigma_0^2 + \frac{k_B T}{m_{Rb}} t^2} \tag{2.3}$$

with the initial size σ_0, the Boltzmann constant k_B, the temperature T, the mass of ^{87}Rb m_{Rb} and the time-of-flight t. The phase-space density is given by

$$\rho_{\text{PSD}} = n \cdot \lambda_{\text{dB}}^3 = n \cdot \frac{h^3}{(2\pi m_{Rb} k_B T)^{3/2}} \tag{2.4}$$

where n denotes the atomic density, h the Planck constant and λ_{dB} the thermal de Broglie wavelength.

[3]Qubig: PM-Rb87 6.8M2. With a signal generator (SMR20 by Rhode and Schwarz) and a 10 W Amplifier (KU PA 640720 -10A by Kuhne Electronic) we can apply up to 38 dBm input power to the EOM.

2.2.2 Optimization of experimental parameters

We have optimized the gray molasses phase with respect to the following experimental parameters.

Duration of gray molasses

For the optimal duration of the gray molasses a compromise between the lowest final temperature and maximum atom number needed to be found. We have varied the duration from 1 ms to 15 ms and found that already after 3 ms temperatures below 10 µK could be reached. As the cooling force is velocity dependent, longer durations led to slightly lower atom numbers, thus lower PSDs. However, experimentally a duration of 6 ms for gray molasses proved to be optimal for a transfer to the magnetic trap.

Laser intensity

The cooler intensity I_C and the repumper intensity I_R are simultaneously varied by the microwave power applied to the EOM. The cooler intensity follows the absolute square of the zeroth order Bessel function $|J_0|^2$ while the repumper sideband intensity follows the first order Bessel function $|J_1|^2$. The total laser power is kept constant $I_{tot} = I_C + 2I_R$. Here we used $I_{tot} = 0.75\, I_S$ with the saturation intensity $I_S = 2.5\,\mathrm{mW/cm^2}$. At a fixed molasses duration of 5 ms, a detuning of $\Delta_{21} = 2.6\,\Gamma$ (where the linewidth is given by $\Gamma = 2\pi \cdot 6.065\,\mathrm{MHz}$) and $\delta_R = 0$ we have varied the power applied to the EOM between 24 dBm and 36 dBm, which corresponds to $I_R/I_C = 0.05$ to 0.75. We found a rather weak dependence, which saturated once a threshold of $\approx$ 32 dBm was exceeded and thus settled for an input power of $I_R/I_C = 0.3$ (33 dBm).

Additionally, we have varied the total laser power. Above a certain threshold only minor influences could be observed. We settled for the maximum available laser power.

Detuning to $F' = 1$

The variation of the detunings Δ_{21} and Δ_R, which are blue detuned to the level $F' = 1$ exhibits a strong influence on the temperature, atom number and PSD. Near-resonance the temperature is high but it drops and reaches a plateau for $\Delta_{21} > 2\,\Gamma$. On the other hand the capture efficiency begins to drop slightly for $\Delta_{21} > 2\,\Gamma$. This results in a optimal detuning of $\Delta_{21} \approx 4\,\Gamma$ for the largest PSD.

Raman detuning δ_R

The Raman detuning is a very sensitive parameter for the efficiency of the gray molasses. At a detuning $\Delta_{21} = 4\,\Gamma$ we varied Δ_{RP}, which corresponds to a variation of the Raman detuning δ_R. We chose a span of ± 1 MHz as shown in figure 2.6. At a

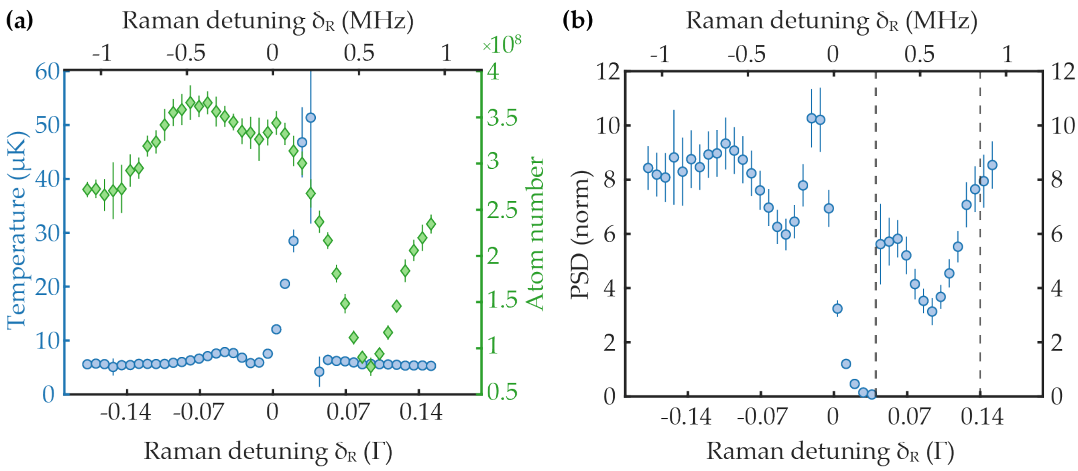

FIGURE 2.6: Characterization of the gray molasses. (a) Influence of the Raman detuning on temperature and atom number. The minimum temperature 5.3(4) µK is reached at $\delta_R = -0.01\,\Gamma$. We observe the characteristic steep increase in temperature for positive detunings. However, for smaller negative detunings the temperature remains below 8 µK and does not increase as in [64]. (b) From the measured temperature and atom number, the phase space density (PSD) is calculated. It is normalized to the PSD of the bright molasses and reaches an increase of 10 at $\delta_R = -0.01\,\Gamma$ as obtained in [64].

Raman detuning of $-0.01\,\Gamma$ we reached an increase of the PSD by approximately a factor of 10, which is the same as reached by Rosi et. al. [64]. For positive Raman detunings we observe a sudden increase in the temperature resembling the Fano type profile, which is the common feature for gray molasses. For detunings $\delta_R > 0.04\,\Gamma$ atomic clouds with different velocities can be observed. We suspect that they fulfill the Raman condition $(\boldsymbol{k_1} + \boldsymbol{k_2})\boldsymbol{v} = \delta_R$, thus their velocities should increase with increasing Raman detuning. This effect has also been reported in [71].

Optimal parameters

We have implemented the gray molasses in the experimental cycle with the following parameters.

duration t (ms)	detuning $\Delta_{21}\,(\Gamma)$	cooling intensity $I_C\ (I_S)$	repumper intensity $I_R\ (I_S)$	Raman detuning $\delta_R\,(\Gamma)$
3	4	0.67-0.55	0.05-0.10	-0.01

Repumping to $F = 1$

After the gray molasses phase atoms can be either in $F = 1$ or $F = 2$ whose fraction can be tuned to some extent by varying the detuning Δ_{RP}. In order to maximize the transfer efficiency for the loading of the magnetic trap via forced evaporation, the atom number should be in the low-field seeking state $|F = 1, m_F = -1\rangle$. Therefore, we optically pump the atoms after the gray molasses phase by switching-off the EOM and only keeping the cooler switched on for an additional 20 µs. We achieve complete transfer without any detectable atoms in $F = 2$.

phase	temperature T (µK)	atom number N (10^8)	cloud radius σ_0 (mm)	phase space density ρ (10^{-6})
MOT	418 ± 30.8	3.72 ± 0.14	0.96 ± 0.09	0.62 ± 0.17
BM	25.2 ± 0.3	3.83 ± 0.08	1.30 ± 0.03	18.29 ± 1.35
GM	5.3 ± 0.4	3.26 ± 0.23	1.15 ± 0.15	189.90 ± 1.54

TABLE 2.1: Characteric quantities of the laser cooling phases at the experimental setup.

2.2.3 Benefits for the overall experimental cycle

We have benchmarked the different laser cooling phases as displayed in table 2.1. By replacing bright molasses with gray molasses the increase in PSD allowed us to shorten two cooling phases. First, the starting frequency of the rf-evaporation in the magnetic trap could be lowered from 20.5 MHz to 7 MHz allowing us to reduce the exponential ramp by 5 s. Second, the MOT phase could be shortened to 6 s as the transfer efficiency has increased from GM to the magnetic trap. Further optimization in the experimental cycle lead to a record cycle time of 23 s providing great benefit for data-intensive measurements. However, operating the experiment constantly at cycle times like these requires modernizing devices like the arbitrary waveform generators for the lattice ramp with faster programming interfaces. Therefore, for daily operation cycle times of about 30 s are common.

2.3 Active magnetic field compensation

For many experiments, the ambient magnetic field must be controlled to a very high degree of accuracy and precision. This includes compensation of static stray fields, for instance the earth magnetic field (typically $\sim$500 mG), but also (and often more importantly) uncontrolled, time-dependent fields fluctuating with typical amplitudes of several mG and frequencies of up to 1 kHz. These fluctuations affect phase coherence [72] and are obstructive for many experiments. These include, for instance, quantum information processing with atoms and ions, quantum gases experiments involving multiple Zeeman states [73, 74], and high-precision atom interferometers and atomic clocks where the magnetic field fluctuations directly affect the accuracy and sensitivity [75].

A first solution is passive shielding by an enclosure with several layers of high permeability materials around the experimental region [76–78]. This is often the method of choice for a single-purpose instrument working near "zero field", *e.g.* high-performance Cesium atomic clocks [79]. Yet, shielding passively the entire experiment is impractical for most setups, which are relatively large and complex in shape. Also, mechanical stress at junctions and access holes for optical and electronic purposes reduce significantly the effectiveness of passive shielding.

A second, often more convenient solution is the active stabilization of the magnetic field using a feedback loop. This requires a magnetic field sensor that can be placed within or near the control volume, and a feedback circuit connected to a set of compensation coils. The advantage of active over passive shielding is that an existing experimental setup can be easily upgraded. Active magnetic field compensations have been sucessfully implemented previously using various sensor technologies including fluxgate magnetometers [80], SQUIDs [81], atomic magnetometers [82, 83] and specially constructed sensors [84]. For ultracold atom experiments, a compensation with a bandwidth of around 3 kHz was achieved using a two-sensor approach of a fluxgate magnetometer for DC- and a magnetic pickup coil for AC-field measurement [80].

In this section, we present a simple active compensation system, which relies on an anisotropic magnetoresitive (AMR) sensor with a high bandwidth. This sensor enables us to use a single sensor in order to achieve good DC and AC sensitivity. It is based on commercial components and can be replicated at low cost. As we intend to stabilize a directional finite magnetic field, we have implemented the system in one dimension, though it can be extended to three dimensions.

The performance of the compensation system can be characterized reliably with optical magnetometry [85]. Here, we use a Bose-Einstein condensate (BEC) as a magnetometer where Ramsey spectroscopy [86] gives access to the magnitude of the magnetic field. Additionally, we measure the influence of field fluctuations on Rabi oscillations, thereby demonstrating a substantial increase of the coherence time while using the active compensation.

This project has been planned as a collaboration with M. Brannan and F. Gerbier who both gave fruitful input on the electronic design. Together with C. Ölschläger and J. Simonet the author continued this work and implemented the use of the BEC as a magnetometer at the experiment [87]. At the beginning of this PhD project the author kept working full-time on the project in collaboration with J. Seeger as a master's student [88]. The results presented in this section stem from this time and were prepared for publication mainly in collaboration with J. Seeger, A. Ilin, C. Ölschläger, J. Simonet and K. Sengstock.

2.3.1 Electronic design

We stabilize the magnetic field along a single axis using a feedback loop illustrated in figure 2.7 (a). This system is integrated within the existing Bose-Einstein condensation apparatus, which is described in more details in section 2.1. The magnetic field sensor[4] is placed outside the vacuum chamber of the main experiment, 85 mm from the position of the atomic cloud. The amplified sensor signal is fed into a home-made PI controller, which regulates a bipolar current source[5]. The latter drives a pair of Helmholtz coils (diameter 212 mm; 0.33 G/A; 250 µH) to generate the compensating magnetic field.

[4] Honeywell, AMR sensor, single axis, HMC1001
[5] HighFinesse, bipolar current source BCS 5/12

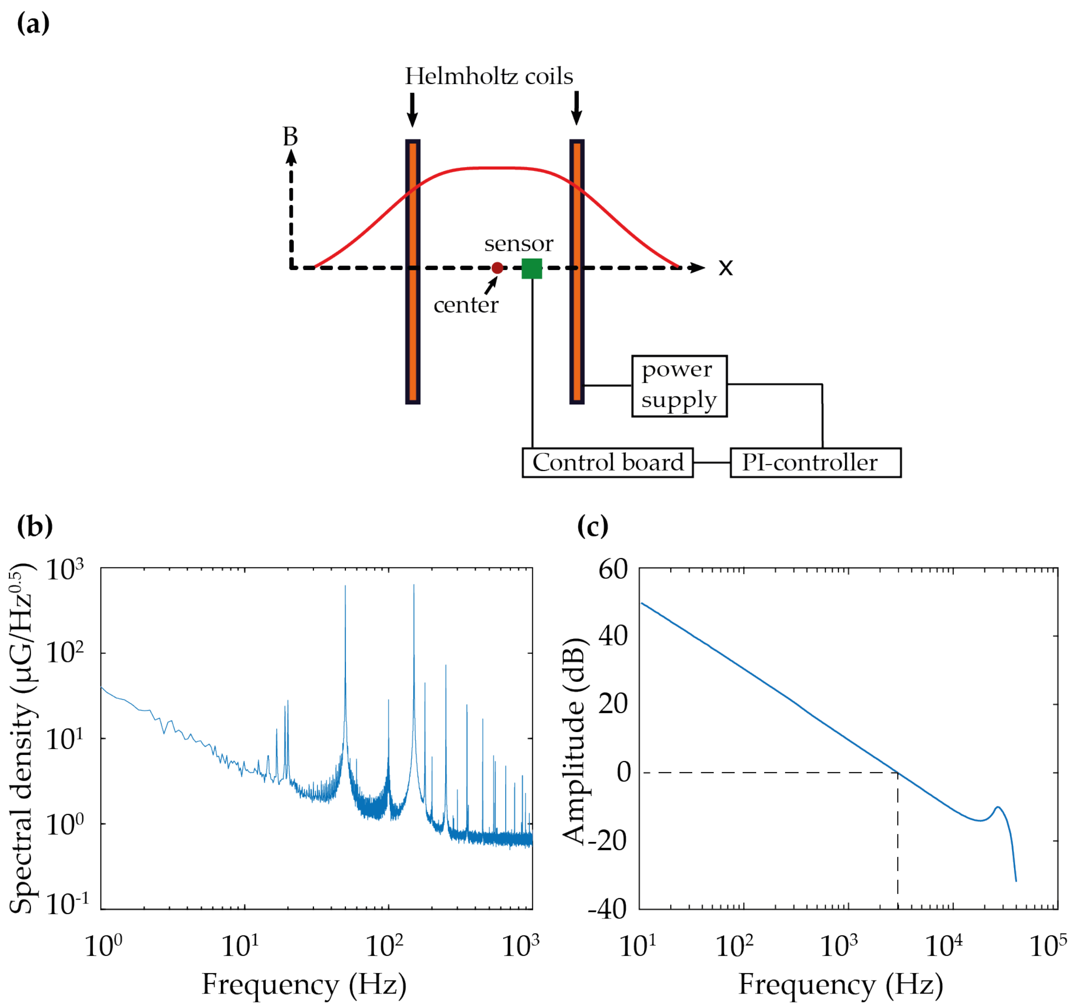

FIGURE 2.7: Setup and characteristics of the active compensation. (a) Schematic illustration of the single-axis negative feedback loop system. (b) Spectral density of the magnetic field noise in a typical laboratory environment. The line frequency and its higher harmonics are the main contributions to the noise. The $1/f$ noise floor is governed by the sensor and the instrumentation amplifier. (c) Measured attenuation for the compensation setup with the in-loop sensor. The bandwidth corresponds to approximately 3 kHz (dashed black line). At 50 Hz an attenuation of 36 dB is achieved.

The central component in this compensation system is the magnetic field sensor in combination with the corresponding amplification stage. The working principle of the chosen single-axis AMR sensor is based on four anisotropic magnetoresistive elements arranged in a Wheatstone bridge. We have favored an AMR sensor over a fluxgate implementation due to its higher bandwidth, which eliminates the need to use a two-sensor approach. Additionally, fluxgate sensors emit AC magnetic field noise at a frequency in the kHz regime, which could disturb the quantum gas experiments. Also, the occurrence of even moderate magnetic fields (see discussion below) during the experimental cycle could modify its zero-point due to hysteresis effects on the ferrite core of the fluxgate.

The main specifications of the AMR sensor are a typical sensitivity of 32 mV/G and a bandwidth of 5 MHz. To take advantage of the high bandwidth, we use an instrumentation amplifier[6] with a gain of 10^3 attaining a maximal sensitivity of 32 V/G for the combined system. Additionally, the amplifier's reference input voltage is controlled via a digital potentiometer[7] in order to adjust the signal offset.

Typical magnetic field fluctuations in our laboratory exhibit a sinusoidal waveform with a 3 mG peak-to-peak amplitude and a period of 20 ms. The dominant frequency contributions in this signal are the electric power line frequency at 50 Hz and its higher harmonics. The corresponding noise spectral density recorded in the laboratory is displayed in figure 2.7 (b). Here, the 1/f noise for low frequencies stems from the sensor and the instrumentation amplifier.

Figure 2.7 (c) shows the Bode diagram characterizing the response of our compensation system. We measured a linear decrease of 20 dB/dec and a bandwidth of 3 kHz where the gain reaches 0 dB. For usual laboratory conditions, this bandwidth is sufficient as only low frequency noise is present. The peak at 24 kHz originates from the LC-resonance of the Helmholtz coils and a built-in capacity within the current supply.

A feature of ultracold atoms experiments is the occurrence of relatively strong magnetic fields (larger than 5 G) during the experimental cycle. A typical cycle consists of two periods. In the first period, the quantum gases are produced using relatively large magnetic fields, for instance in the magnetic trap. In the second period a well-stabilized, low-magnitude magnetic field is required during the experiment. However, the application of magnetic fields during the first period can misalign the magnetic domains in the resistive elements of the AMR sensor and severely degrade the sensitivity. Fortunately, the domain alignment can be restored by an integrated reset function of the sensor. We have estimated its repeatability for our system to 65 μG (based on the datasheet [89]).

[6] Analog devices, AD524

[7] Analog Devices, AD5292

2.3.2 Magnetic field characterization with quantum gases

To characterize the performance of the magnetic field compensation, Bose-Einstein condensates can act as high precision magnetometers [90, 91]. This is particularly beneficial as the BEC is located exactly where the stabilized magnetic field is required. The experiment of [91] demonstrated a resolution on the order of 10 nG.

Our approach relies on Ramsey spectroscopy [86] allowing us to probe the magnetic field in a single measurement with a precision of $\sim$ 10 µG. By recording consecutive single measurements over the course of days we are able to determine the long term stability with and without active compensation. In addition, we monitor the coherence of Rabi oscillations driven by a radio-frequency (RF) resonant with a magnetic-field-sensitive transition. We demonstrate that the active compensation significantly improves the coherence when Rabi oscillation frequencies are on the order of the magnetic field noise.

2.3.3 Experimental protocol

We start the experimental procedure by preparing a spin-polarized ^{87}Rb-BEC in the state $|\mathrm{F}=1, \mathrm{m_F}=-1\rangle$ in a crossed optical dipole trap at a wavelength of 1064 nm with trapping frequencies of $\omega_{x,y,z} \approx 2\pi \times (20, 20, 50)$ Hz. We employ several pairs of Helmholtz coils for controlling the magnetic fields. For each spatial direction, we apply time-independent fields to cancel static fields at the location of the atoms, to approximately (0 ± 1) mG (static compensation).

We apply a bias magnetic field along the x direction, with strength $\mathrm{B_0} = 110$ mG stabilized by a pair of coils within the feedback loop (active compensation). The bias field lifts the $|\mathrm{F}=1\rangle$ hyperfine manifold into three resolved Zeeman sublevels $\mathrm{m_F} = 0, \pm 1$. We perform experiments with atoms which are initially in the sublevel $m_F = -1$ and experience a Zeeman shift $E_Z = \mu_B B/2$, with μ_B the Bohr magneton and with

$$B = \sqrt{(B_0 + \Delta B_x)^2 + \Delta B_y^2 + \Delta B_z^2} \approx B_0 + \Delta B_x + \frac{\Delta B_y^2 + \Delta B_z^2}{2B_0}, \tag{2.5}$$

the modulus of the magnetic field felt by the atoms. Here we introduced the desired bias field value B_0 and the fluctuating magnetic field $\boldsymbol{\Delta B}$ to be compensated, and assumed $|\boldsymbol{\Delta B}| \sim 1$ mG $\ll B_0$. The contribution of the transverse components of $\boldsymbol{\Delta B}$ are thus small corrections ($\sim$ 100 µG), and the component of $\boldsymbol{\Delta B}$ parallel to the applied field is therefore the most significant one. As a result, we only stabilize actively the field only in the x-direction and ignore the transverse components ΔB_y and ΔB_z.

Prior to any spectroscopic experiments the magnetic field sensor is reset to restore its zero point, which is altered by the strong fields we use to produce the BEC.

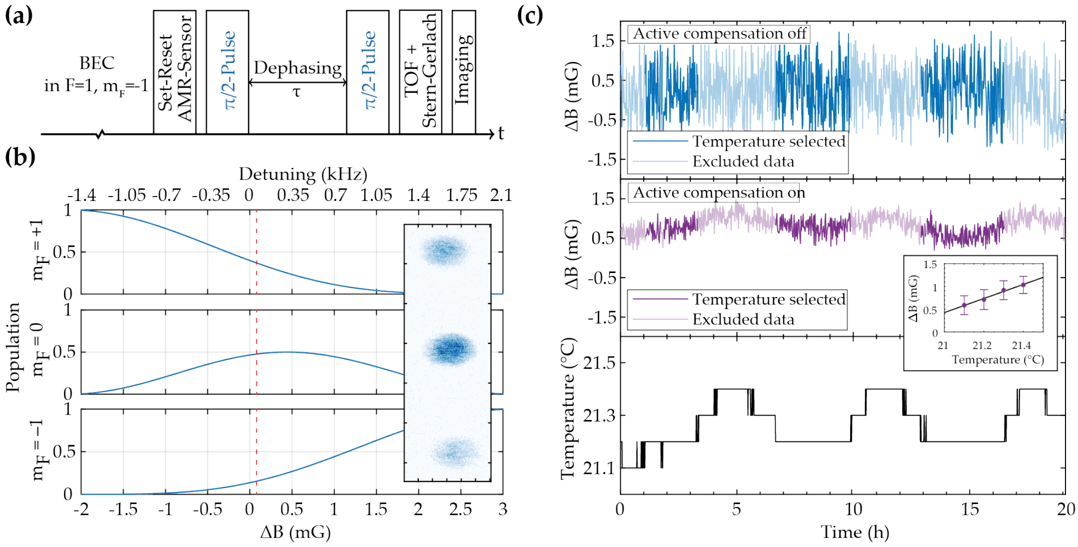

FIGURE 2.8: Magnetic field measurement with Ramsey spectroscopy. (a) Experimental sequence for Ramsey spectroscopy. Two phase-controlled RF pulses of 70 µs duration are separated by a wait time of $\tau = 50\,\mu s$. The Larmor frequency of the pulses is $\mu_B B_0/2 \approx 77.0$ kHz, and the detuning $\delta = \omega_{rf} - \mu_B B_0/2 \approx 1.5$ kHz. The Rabi frequency is $\Omega = 2\pi \cdot 3562$ Hz. (b) Theoretical prediction of the population of different Zeeman states versus deviation of the magnetic field strength ΔB from the set value. The inset shows an exemplary absorption image to illustrate the data evaluation procedure. The populations of the three m_F-components in $F = 1$ are mapped onto a magnetic field deviation ΔB (dashed red line). (c) Magnetic field deviation with (top panel, blue) and without active compensation (middle panel, purple) measured over 20 h. Additionally, the temperature logged at the experiment is shown (bottom panel, black). The statistical analysis of the data in figure 2.9 is performed for a temperature $T = 21.2\,°C$ (highlighted color). The inset depicts a linear fit yielding a temperature dependence of 1.5(1) mG/K of the magnetic field sensor. Error bars quantify the standard deviation of each temperature bin.

The active compensation is immediately switched on and the Ramsey or Rabi experiment **is** performed. Finally, the populations of the three Zeeman states are determined. The three components are spatially separated by a Stern-Gerlach magnetic field gradient during a time-of-flight of 33 ms and then imaged via absorption imaging. The measured populations allow us to infer the absolute magnetic field B with Ramsey spectroscopy as explained in the following section.

2.3.4 Long-term stability - Ramsey spectroscopy

Ramsey spectroscopy constitutes an ideal technique to characterize the long-term stability of the compensation as the magnetic field can be deduced from a single Ramsey experiment. As depicted in figure 2.8 (a), such a sequence consists of two phase-coherent RF pulses separated by a wait time τ. The two pulses respectively prepare and remix coherent superpositions of two Zeeman states. The populations at the end of the pulse sequence oscillate as a function of the detuning from the resonance $\delta = \mu_B B/\hbar - \omega_{\mathrm{rf}}$, resulting in a pattern known as Ramsey fringes. We focus on the central fringe near $\delta = 0$. A deviation of the magnetic field $\Delta B = |\mathbf{B} -$

$\mathbf{B}_0|$ from $B_0 = 110\,\text{mG}$ changes the detuning and thus modifies the final populations of the different Zeeman states.

Figure 2.8 (b) shows the populations in the three m_F-components as a function of ΔB. These Ramsey fringes are calculated numerically by solving the time dependent Schrödinger equation for a three-level system (thus neglecting any effect of interatomic interactions). We apply a static frequency detuning $\delta = 1.5\,\text{kHz}$ of the driving RF field, so $\Delta B = 0$ corresponds to the maximal slope of the Ramsey fringe, thereby maximizing the sensitivity. Inverting the calculated fringe pattern from the three-level model, we are then able to determine from the measured relative population the magnitude and sign of $B - B_0$ in a time-resolved fashion.

As a central result, we demonstrate a clear reduction of magnetic field fluctuations by the active compensation. Figure 2.8 (c) depicts the recorded field fluctuations obtained with Ramsey spectroscopy. Here, ΔB is probed every 40 s over a total time span of 20 h with and without the active compensation, each scheme being applied alternately in every second experimental realization.

Without the active compensation (top panel, blue) peak-to-peak fluctuations of about 2 mG prevail. They are clearly reduced when the active compensation is enabled (middle panel, purple). Nevertheless, the active compensation exhibits distinct oscillations with a period of 6 h. They occur due to temperature fluctuations (bottom panel, black), which have been measured during the Ramsey experiments. With a peak-to-peak amplitude of about $\sim$0.4 °C they bias the magnetic field sensor directly. By correlating ΔB to the measured temperature we quantify the temperature dependence for our system to $1.5(1)$ mG/K, consistent with the specifications from the manufacturer. In principle, this could be improved significantly by implementing a current source to supply the magnetic field sensor (e.g. [92] and references therein), or by directly controlling the sensor temperature using a dedicated feedback system.

In order to characterize the optimal performance of our system, the measured data is selected for a temperature of 21.2 °C (highlighted in darker colors). The selected data of ΔB is statistically analyzed and represented by normalized histograms in figure 2.9. The two statistical distributions, each containing approximately 500 measurements, are fitted with Gaussians yielding a standard deviation of $\sigma_{\text{off}} = 860\,\mu G$ without and of $\sigma_{\text{on}} = 240\,\mu G$ with the active compensation. The results demonstrate that the active compensation reduces the magnetic field fluctuations by a factor of 3.6.

Large fluctuations without the active compensation can be attributed mainly to magnetic fields oscillating with the line frequency. As depicted in the inset of figure 2.9, a time-resolved measurement of the present field with an independent AMR sensor shows a peak-to-peak amplitude of $\sim$3 mG, consistent with the width of the statistical distribution. Along these lines, we found that the use of a power line trigger, synchronizing the Ramsey sequence with the phase of the 50 Hz oscillations for each measurement, additionally improves the magnetic field stability for short

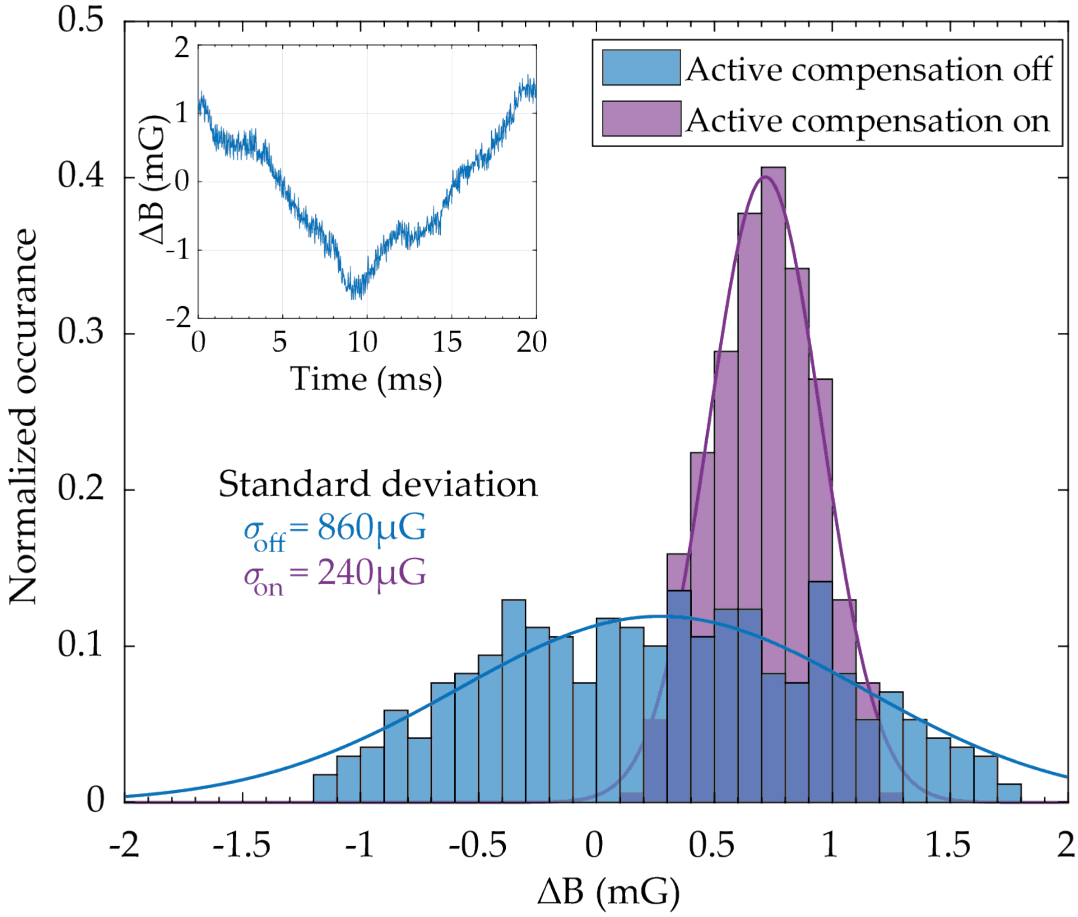

FIGURE 2.9: Statistical analysis of the Ramsey spectroscopy measurement. The histograms of the magnetic field deviation ΔB are shown with and without the active compensation. The normalized distributions are constructed from the temperature selected data from the Ramsey experiment and are fitted with a Gaussian distribution to estimate the standard deviation $\sigma_{\mathrm{off/on}}$. Note that the reference voltage of the control loop can always be set such that the mean of the active compensation is centered around zero. The inset displays the magnetic field measured for 20 ms with the AMR sensor during the experimental cycle without active compensation.

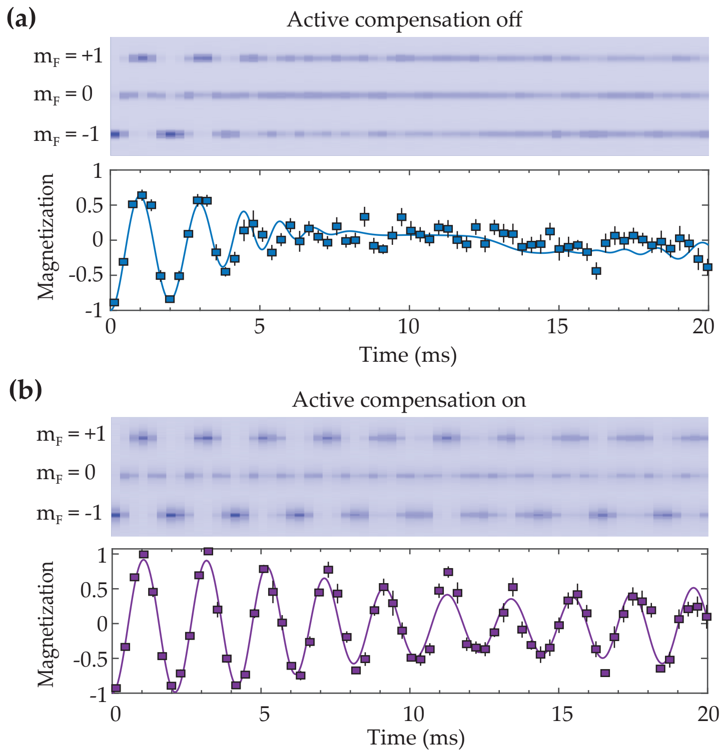

FIGURE 2.10: Rabi oscillations. (a) The data without the active compensation is shown while in (b) the data is shown with the active compensation enabled. The upper panels display averaged absorption images where the population of the three Zeeman components is monitored in time. The lower panels show the extracted longitudinal magnetization, defined as the population difference between $|m_F = +1\rangle$ and $|\mathrm{m_F} = -1\rangle$. The error bars show the standard deviations of the single measurements (approximately five per data point). The solid lines represent numerical simulations with parameters taken from the results of the Ramsey spectroscopy. The data has been temperature selected as described in section 2.3.4.

timescales ($\sim$1 ms). As a consequence, the standard deviations without and with active compensation are further reduced to $\sigma_{\mathrm{off}} = 305\,\mu$G and $\sigma_{\mathrm{on}} = 130\,\mu$G when using the power line trigger.

2.3.5 Probing coherence - Rabi oscillations

Rabi oscillations between the three Zeeman components in $|\mathrm{F} = 1\rangle$ with frequencies on the order of the line frequency are strongly affected by magnetic field fluctuations. Varying shot-to-shot fields as well as non-vanishing AC fields during the RF coupling induce effective detunings and lead to an overall dephasing when averaged over many experimental realizations. Therefore, we compare the coherence of the Rabi oscillations with and without the active compensation. Using the power line trigger is essential for this comparison. As the dephasing due to fluctuating fields at the power line frequency would be too large to observe any Rabi oscillations.

The experimental results shown in figure 2.10 clearly demonstrate the increased coherence time when the active stabilization is turned on. Without the active compensation (see figure 2.10 (a)) the absorption images show only three oscillation periods of up to 5 ms followed by an almost equal occupation of all three Zeeman states. In contrast, with the active compensation (see figure 2.10 (b)) distinct oscillations are present over a time span of 20 ms proving the clear reduction of dephasing.

For a quantitative analysis, we extract the magnetization, defined as the population difference between $|m_F = +1\rangle$ and $|m_F = -1\rangle$, and compare it including the field fluctuations at the experiment to numerical simulations performed by [88]. We numerically solve the time dependent Schrödinger equation of the coupled three-level system with fluctuating DC and AC fields including the results obtained from the Ramsey experiments as well as from the independent AMR sensor. The shot-to-shot fluctuations of the DC field are deduced from Ramsey spectroscopy where the power line trigger is used and are given by the widths $\sigma_{\mathrm{off}} = 305\,\mu\mathrm{G}$ and $\sigma_{\mathrm{on}} = 130\,\mu\mathrm{G}$. The phase and the amplitude of the AC field during the Rabi oscillations are inferred from the AMR sensor measurement (inset in figure 2.9) and a Ramsey experiment where the delay after the power line trigger is scanned. To model the AC field as measured in figure 2.7 (b), we superimpose a 50 Hz sine wave with its 3rd and 5th harmonics, *i.e.* $\Delta B_x = \sum_{n=1,3,5} a_n \cos(n\omega_{\mathrm{pw}}t + \phi_n)$ with $\omega_{\mathrm{pw}} = 2\pi \times 50\,\mathrm{Hz}$.

The dominant amplitude without (respectively with) active compensation yields $a_1 \approx 1\,\mathrm{mG}$ ($200\,\mu G$), whereas the phases are given by $\phi_1 = 0.75\pi$ ($\phi_1 = -0.25\pi$). We also obtain the Rabi frequency of $\Omega = 2\pi \cdot 464\,\mathrm{Hz}$ by fitting the first half period of the Rabi oscillations where the magnetic field has a minor influence.

The excellent agreement between the measurements and the simulations suggests that the observed behavior can be attributed to the field fluctuations determined in section 2.3.4 and that the active compensation increases the coherence time by at least a factor of 4.

2.4 Conclusion and outlook

In this chapter we have introduced the experimental apparatus together with major experimental upgrades, which were implemented during this PhD project. Especially important is the implementation of a Λ-enhanced gray molasses for ^{87}Rb on the D_2-transition with a temperature of 5.3(4) µK. This resulted in a significantly shorter experimental cycle time, which we could reduce by about 10 s to 23 s.

We have demonstrated an active magnetic field compensation, which is robust against strong magnetic fields and can be implemented at many quantum gas experiments. Although the active compensation has been realized in one dimension, the compensation can in principle be extended to three dimensions. We have studied in detail how the active stabilization improves the magnetic field stability by using the ^{87}Rb-BEC itself as a magnetometer with Ramsey spectroscopy. We achieve a standard deviation of the magnetic field fluctuations of $\sigma_{\mathrm{on}} = 240\,\mu\mathrm{G}$. This is further improved to $\sigma_{\text{on}} = 130\,\mu\text{G}$ by using a trigger to synchronize the experiment with the 50 Hz frequency of the power line. Additionally, we have demonstrated that the active compensation substantially increases the coherence time of the Rabi oscillations by a factor of 4.

The remaining limitations of the magnetic field stability are threefold: first, uncompensated transverse magnetic fields; second, the sensor noise (after amplification) and the residual lack of reproducibility of the set/reset sequence (see section 2.3.1); third, the fact that the sensor does not measure the field exactly at the atom location but at a slightly different position, which means that even in an ideal feedback system the fluctuations seen by the atoms would be only reduced, and not perfectly canceled. All these factors, with a magnitude of roughly $50 - 100\,\mu G$, contribute to the residual ΔB when the compensation is enabled. This indicates that the performances of the feedback system are close to the ones achievable with the AMR sensor.

The implemented active compensation allows for improving magnetic field sensitive studies especially for spinor or dipolar gases. For the experiment in higher bands it can be especially advantageous for preparing with π-pulses the internal state where magnetic field fluctuations are disturbing. Moreover, the increased coherence time is essential for novel Floquet engineering schemes involving internal degrees of freedom, especially for the realization of non-abelian artificial gauge fields such as spin-orbit coupling.

CHAPTER 3

The optical honeycomb lattice

Chapter 3

The optical honeycomb lattice

The optical lattice setup constitutes the heart of the experiment. It allows using different configurations of 1D, 2D or 3D lattices. The setup has been implemented and described in the PhD thesis of C. Becker [43]. More experiments and details on the characteristics of the lattice can be found in the PhD theses by P-Soltan-Panahi, J. Struck, M. Weinberg and C. Ölschläger [44–47]. This chapter presents the optical potentials with a focus on the dipole trap and and the bipartite hexagonal lattice, which is central for the results presented in this thesis. We give a brief introduction to its main characteristics as the lattice potential, band structure and harmonic confinement. The detection methods, time-of-flight and band mapping, are discussed. Further, a new high-bandwidth intensity control for the lattice beams together with an investigation of phase-noise is presented. The experimental data presented in this chapter has been measured with main contributions by the author and A. Ilin. For the development and setup of the intensity control the author has collaborated with J. Seeger. The analysis of the data presented in this chapter has been conducted by the author.

3.1 Optical potentials

3.1.1 Atom-light interaction

When describing the coupling of light to atoms a fundamental distinction is made between two types of interaction: dissipative forces exerted by absorption and emission of photons and dipole forces [53]. While the former are being used for laser cooling techniques the latter are also applied for trapping and realizing potentials such as optical lattices [93].

The mechanism of the dipole force stems from the interaction of the light field with a light induced electric dipole moment of the atom. This coupling of the quantized light field and the atomic eigenenergies leads to new common eigenstates, which are called dressed states [94]. Within perturbation theory the first order of the energy shift on a state i can be written as

$$\Delta E_i = \sum_j \frac{|\langle j|\hat{H}_{\mathrm{AL}}|i\rangle|^2}{\hbar(\omega_{ij} - \omega_L)} \tag{3.1}$$

with the reduced Planck constant $\hbar$, the atomic resonance ω_{ij} and the frequency of the laser light ω_L, the Hamiltonian for the atom-light interaction $\hat{H}_{\mathrm{AL}} = -\hat{\boldsymbol{\mu}}\hat{\boldsymbol{E}}$ with the dipole operator $\hat{\boldsymbol{\mu}}$ and the electric field operator $\hat{\boldsymbol{E}}$.

For our experimental realization the D1 and D2 lines of ^{87}Rb couple the ground state $5^2S_{1/2}$ to the states $5^2P_{1/2}$ and $5^2P_{3/2}$. Evaluating the above expression for the dipole potential of an atomic state $|F, m_F\rangle$ then yields

$$V_{\mathrm{dip}}(\mathbf{r}) = -\frac{\pi c^2}{2} I(\mathbf{r})(\mathcal{D}_1 + 2\mathcal{D}_2 - g_F m_F \mathcal{P}(\mathbf{r})(\mathcal{D}_1 - \mathcal{D}_2)) \tag{3.2}$$

where c is the speed of light, $g_F = \mp 1/2$ the Landé-factor of the hyperfine states $F = 1, 2$ and m_F the corresponding magnetic substate. I($\mathbf{r}$) denotes the intensity of the light field, the following abbreviation $\mathcal{D}_i$ the contribution of the D1 and D2 lines with its frequency ω_{D_i} and its natural linewidth Γ_{D_i}

$$\mathcal{D}_i = \frac{\Gamma_{D_i}}{\omega_{D_i}^3}\left(\frac{1}{\omega_{D_i} - \omega_L} + \frac{1}{\omega_{D_i} + \omega_L}\right). \tag{3.3}$$

The polarization of the light field is defined by

$$\mathcal{P}(\mathbf{r}) = \frac{I_{\sigma^+}(\mathbf{r}) - I_{\sigma^-}(\mathbf{r})}{I(\mathbf{r})} \tag{3.4}$$

and can take on values of $\mathcal{P}(\mathbf{r}) = 0, \pm 1$ for π and $\sigma^\pm$ polarized light. Especially the local polarization plays an important role for the honeycomb lattice (section 3.2) with the near-resonant laser wavelength $\lambda_L = 830\,\mathrm{nm}$ as this lifts the degeneracy between the A- and B-sites. In contrast, for the dipole trap with $\lambda_{DT} = 1064\,\mathrm{nm}$ the spin-dependency can be neglected. Thus, it is practical to split equation (3.2) into a spin-independent and a spin-dependent part

$$\begin{aligned} V_{\mathrm{dip}}(\mathbf{r}) &= V_{\mathrm{SI}}(\mathbf{r}) + V_{\mathrm{pol}}(\mathbf{r}) && (3.5) \\ &= V_{\mathrm{SI}}(\mathbf{r}) + g_F m_F \mu_B B_{\mathrm{eff}}(\mathbf{r}) && (3.6) \end{aligned}$$

with the Bohr magneton μ_B so that an effective magnetic field can be defined as

$$B_{\mathrm{eff}}(\boldsymbol{r}) = -\eta V_{\mathrm{SI}}(\boldsymbol{r})\mathcal{P}(\boldsymbol{r})/\mu_B. \tag{3.7}$$

The parameter $\eta = \dfrac{\mathcal{D}_1 - \mathcal{D}_2}{\mathcal{D}_1 + 2\mathcal{D}_2}$ describes the influence of the laser wavelength onto the spin-dependent potential. For the lattice wavelength it yields $\eta \approx 0.13$ whereas for large detunings compared to the D1 and D2 transitions ($\mathcal{D}_1 - \mathcal{D}_2 \approx 0$) it is negligible. For calculations of the dipole potentials it is useful to express the spin-independent potential with a conversion factor $u(\lambda)$ for the polarizability as $V_{\mathrm{SI}}(\boldsymbol{r}) = -u(\lambda)I(\boldsymbol{r})$. For the two wavelengths in the experiment the conversion factor yields $u(\lambda_{DT}) = 2.11 \times 10^{-36}\,\mathrm{m^2 s}$ and $u(\lambda_L) = 9.38 \times 10^{-36}\,\mathrm{m^2 s}$.

3.1.2 Crossed dipole trap

The dipole trap provides a reliable way to produce cold and dense Bose-Einstein condensates capturing all Zeeman substates. As the dipole trap laser with $\lambda_{\mathrm{DT}} = 1064\,\mathrm{nm}$ is far red-detuned, the atoms experience a conservative force towards the maximum laser intensity. Experimentally this is realized by superimposing two Gaussian laser beams onto the atoms. The intensity profile of a single elliptical Gaussian beam propagating along z, with beam power P and wavelength λ_L is given by

$$I(x,y,z) = \frac{2P}{\pi w_x(z) w_y(z)} \exp\left(-\frac{2x^2}{w_x(z)^2} - \frac{2y^2}{w_y(z)^2}\right). \tag{3.8}$$

Here the beam radius is $w_{x,y}(z) = w_{0_{x,y}}\sqrt{1+(z/z_R)^2}$ with the waist $w_{x,y}(0) = w_{0_{x,y}}$ at the focus of the beam and the Rayleigh length $z_R = \pi w_0^2/\lambda_L$. For two orthogonal Gaussian laser beams the intensity profile in vicinity of the focus for $|\boldsymbol{r}| \ll z_R$ then reads

$$I(\mathbf{r}) = \frac{2P}{\pi w_{0_h} w_{0_v}} \exp\left(\frac{-2y^2}{w_{0_v}^2}\right)\left[\exp\left(-\frac{2x^2}{w_{0_h}^2}\right) + \exp\left(-\frac{2z^2}{w_{0_v}^2}\right)\right]. \tag{3.9}$$

For weak potentials the influence of gravity needs to be considered by

$$V_{\mathrm{tot}}(\mathbf{r}) = V_{\mathrm{dip}}(\mathbf{r}) + mgy. \tag{3.10}$$

It leads to a shift of the minimum of the potential, which is called gravitational sag. As depicted in figure 3.1 (b) already small changes in the final power of the dipole trap beams lead to a shift of the trap position. This is especially critical for the alignment of the three lattice beams whose waists must be superimposed with the dipole trap minimum. Therefore, we have assured a high repeatability of the final trap depth. We have updated the version of the experimental control and have switched from an external waveform generator to the AdWin system allowing for faster programming.

To compensate for gravity the vertical beam waists $w_{0,v} \approx 82\,\mu\mathrm{m}$ were chosen to be much smaller than the horizontal beam waists $w_{0,h} \approx 245\,\mu\mathrm{m}$ resulting in an elliptical trapping geometry. As the harmonic confinement plays a crucial role for the condensation in higher bands, we have measured the trap frequencies by inducing oscillations of the BEC shining a near-resonant lattice laser beam slightly off-centered onto the atomic cloud for 500 µs. The absorption images after different holding times have been evaluated using principal component analysis (PCA). In figure 3.1 (c) the mean image of the measurement series and the first three principal components (PC) are shown. PC 1 and PC 2 correspond to the horizontal and vertical dipole mode. PC 3 shows a breathing mode as an example of a higher order excitation. The weight of PC 1 and PC 2 is plotted in dependence of time in figure 3.1 (d) to extract the horizontal and vertical trap frequency. A fit of the oscillations with a sine and an exponential decay yields a frequency of 20.2(5) Hz for the horizontal and 45.3(7) Hz for the vertical trapping frequency. Due to the versatile applications

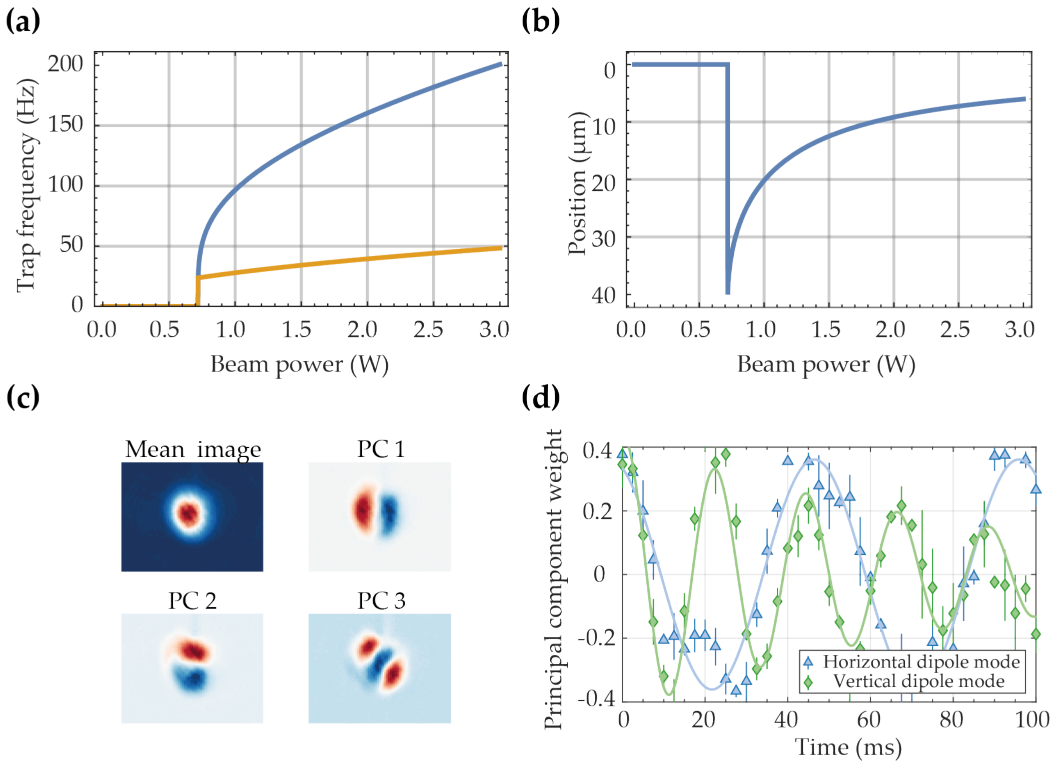

FIGURE 3.1: Properties of the elliptical crossed dipole trap. (a) Horizontal (yellow) and vertical (blue) trap frequencies in dependence of the power for each beam. The shallowest trap is reached at 750 mW per laser beam. (b) The minimum of the trap is shifted by gravity, the so-called gravitational sag (c) Mean image and principal components of a measurement to determine the trap frequencies. PC 1 and PC 2 correspond to the horizontal and vertical dipole mode. PC 3 shows a breathing mode. (d) PC 1 and and PC 2 are fitted with an exponentially damped sine yielding $\omega_h = 2\pi \times 20.2(5)$ Hz for the horizontal trap frequency and $\omega_v = 2\pi \times 45.3(7)$ Hz for the vertical trap frequency.

of PCA it has been implemented by the author as a standard evaluation method, e.g. to verify the correct alignment of the dipole trap or the lattice. In quantum gas experiments PCA has also previously been applied to analyze collective excitations by Dubessy et al. [95].

3.1.3 Optical lattices

Optical lattices are periodic light potentials, which are formed by the inference of Gaussian laser beams. They offer great flexibility for experiments with ultracold quantum gases as e.g. tuning of intensity, frequency, phase or polarization. Depending on the number of lattice beams and their alignment versatile geometries and dimensionalities are possible.

Our experiment uses different configurations of 1D, 2D or 3D lattices. The lattice setup consists of three traveling waves at 830 nm. They interfere in the x-y plane under angles of 120°. Using only two of the three lattice beams creates a 1D lattice with a lattice constant of $a_{1D} = 479\,\mathrm{nm}$. All three laser beams together realize different 2D lattices geometries by adjustment of the polarization: a triangular lattice for out of plane polarization, a polarization lattice for the polarization being $\sim 35°$ or a bipartite hexagonal lattice with a tunable energy offset between the A- and B-sites for a polarization pointing in the lattice plane. The A- and B-sites are separated by $a_{\mathrm{Hex}}/\sqrt{3} = 320\,\mathrm{nm}$. Additionally, orthogonal to the lattice plane a retro-reflected 1D-lattice at a wavelength of 1064 nm with a lattice constant $a_{\perp} = \lambda/2 = 532\,\mathrm{nm}$ can be superimposed to create a 3D lattice. The lattice setup has been implemented within PhD project of C. Becker [43]. More experiments and details on the characteristics of the lattice can be found in the PhD theses by P-Soltan-Panahi, J. Struck, M. Weinberg and C. Ölschläger [44–47]. Additionally, a thorough description of the bipartite spin-dependent honeycomb lattice is given by Lühmann et al. [38].

3.2 Honeycomb lattice

The 2D bipartite spin-dependent honeycomb lattice (see figure 3.2) constitutes the central element of the experiment. In this section we discuss the characteristics of the lattice, which are especially relevant for condensation in higher bands. (i) Relevant is the lattice potential, where the dynamical tuning of the potential offset ΔV_{AB} between the two sublattices controlled by a magnetic field allows us to populate higher bands. (ii) We present general characteristics of the band structure. (iii) The radial confinement at the lattice sites and the harmonic confinement along the tubes in z-direction of the lattice becomes important in deep lattices, where condensation in higher bands occurs.

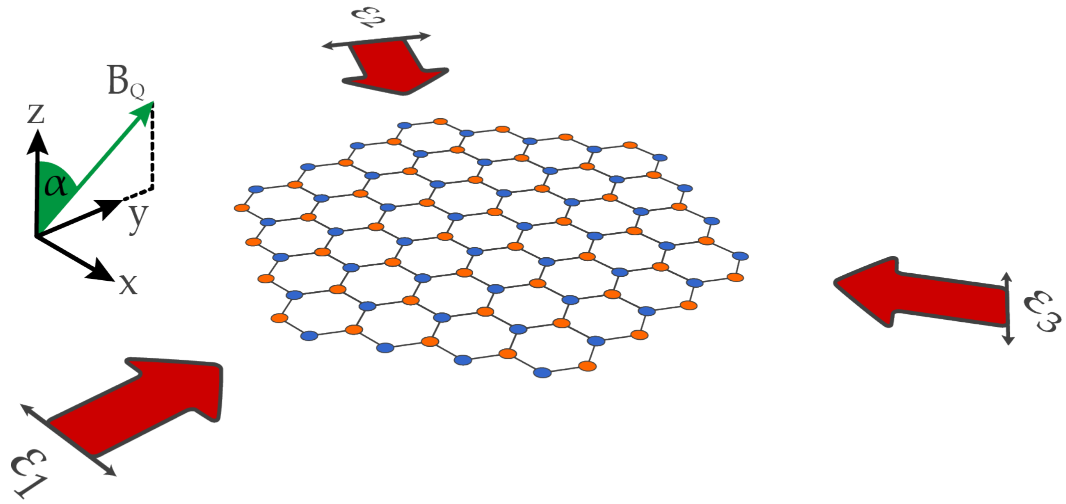

FIGURE 3.2: Lattice setup of the bipartite honeycomb lattice. The three laser beams intersect pairwise under an angle of 120° and are linearly polarized in the x-y lattice plane. A homogeneous quantization field $\boldsymbol{B}$ can be rotated continuously by an angle α to change the energy offset between the A- and B-sites. The energy offset is at its maximum for $\alpha = 0°$ and 180° and vanishes for $\alpha = 90°$.

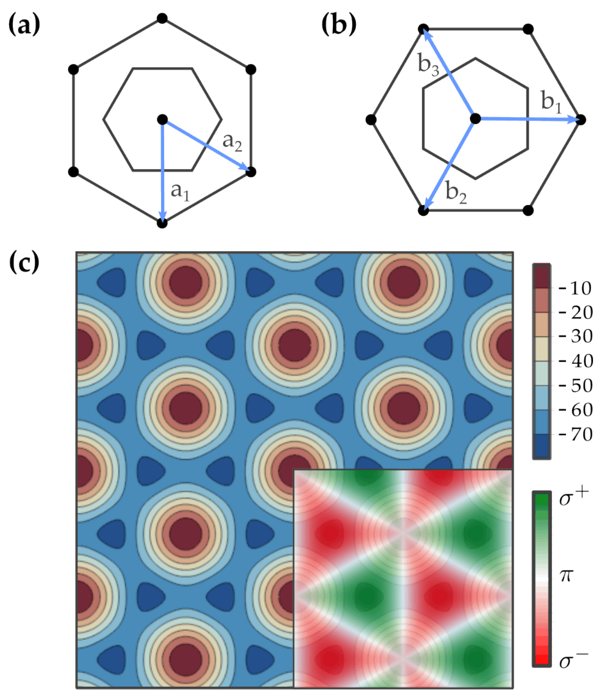

FIGURE 3.3: (a) Bravais lattice with the lattice vectors a_1 and a_2 as defined in this section. The inner hexagon resembles the Wigner-Seitz cell. (b) Reciprocal lattice with the reciprocal lattice vectors b_1, b_2 and b_3. The inner hexagon marks the first Brillouin zone. (c) Potential of the honeycomb lattice at $V_{2D} = 8\,\mathrm{E_{rec}}$ for $m_F = 0$. The inset shows the polarization pattern, which alternates from σ^+ to σ^- and lifts the degeneracy of the A- and B-sites.

3.2.1 Lattice potential

To obtain the potential $V_{\text{Lat}}(\boldsymbol{r})$ experienced by the atoms as described in section 3.1.1, the intensity needs to be calculated

$$I(\boldsymbol{r}) = \frac{1}{2}\epsilon_0 c \int |\boldsymbol{E}_{\text{Lat}}(\boldsymbol{r},t)|^2 \text{dt}, \tag{3.11}$$

where $\boldsymbol{E}_{\text{Lat}}$ is the sum of the electric fields of the three lattice beams $\boldsymbol{E}_{\text{Lat}}(\boldsymbol{r},t) = \sum_{i=1}^{3} \boldsymbol{E}_i(\boldsymbol{r},t)$. Here, the often used plane waves approximation is not sufficient when the harmonic confinement cannot be neglected. Thus, we employ the electric field of a Gaussian beam

$$\boldsymbol{E}(\boldsymbol{r},t) = E_0\, \boldsymbol{\epsilon}_i\, e^{-r^2/w_0^2} e^{-i(\boldsymbol{k}_i z - \omega_L t + \Phi_i)}. \tag{3.12}$$

We define the polarization $\boldsymbol{\epsilon}$ of the electric field orientated in the x-y-lattice plane, the beam waist w_0 and the wave vectors of the laser beams

$$\boldsymbol{k}_1 = k_L \cdot \begin{pmatrix} 0 \\ 1 \\ 0 \end{pmatrix}, \quad \boldsymbol{k}_2 = \frac{k_L}{2} \cdot \begin{pmatrix} \sqrt{3} \\ -1 \\ 0 \end{pmatrix}, \quad \boldsymbol{k}_3 = \frac{k_L}{2} \cdot \begin{pmatrix} -\sqrt{3} \\ -1 \\ 0 \end{pmatrix} \tag{3.13}$$

with $k_L = \frac{2\pi}{\lambda_L}$. For clarity we follow the definition and notation in the PhD thesis of M. Weinberg [46]. With the relation $\boldsymbol{b}_i = \epsilon_{\text{ijk}}(\boldsymbol{k}_j - \boldsymbol{k}_k)$ the reciprocal lattice vectors can be obtained

$$\boldsymbol{b}_1 = b \cdot \begin{pmatrix} 1 \\ 0 \\ 0 \end{pmatrix}, \quad \boldsymbol{b}_2 = \frac{b}{2} \cdot \begin{pmatrix} -1 \\ -\sqrt{3} \\ 0 \end{pmatrix}, \quad \boldsymbol{b}_3 = \frac{b}{2} \cdot \begin{pmatrix} -1 \\ \sqrt{3} \\ 0 \end{pmatrix}, \tag{3.14}$$

where $b = \sqrt{3}k_L$ and with the relation $\boldsymbol{a}_i \cdot \boldsymbol{b}_i = 2\pi\delta_{ij}$ the Bravais lattice vectors can be defined

$$\boldsymbol{a}_1 = a \cdot \begin{pmatrix} 0 \\ -1 \\ 0 \end{pmatrix}, \quad \boldsymbol{a}_2 = \frac{a}{2} \cdot \begin{pmatrix} \sqrt{3} \\ -1 \\ 0 \end{pmatrix}, \quad \boldsymbol{a}_3 = \frac{a}{2} \cdot \begin{pmatrix} \sqrt{3} \\ 1 \\ 0 \end{pmatrix}, \tag{3.15}$$

with the lattice constant $a = 2\lambda_L/3$. Choosing two of the respective vectors spans the Bravais and reciprocal lattice as depicted (see figure 3.3 (a), (b)). The lattice potential $V_{\text{Lat}}(\boldsymbol{r})$ can be calculated numerically by using eq. (3.5) and is illustrated in figure 3.3 (c). Neglecting the Gaussian beam character an analytic expression with a spin-independent and spin-dependent part can be given

$$V_{Lat}(\boldsymbol{r}) = -V_{2D}(V_{\text{SI}}(\boldsymbol{r}) + V_{\text{pol}}(\boldsymbol{r})) \tag{3.16}$$

where

$$V_{\mathrm{SI}}(\boldsymbol{r}) = 6 - 2\sum_{i=1}^{3}\cos(\boldsymbol{b}_i\boldsymbol{r} - \Delta\phi_{jk}) \tag{3.17}$$

$$V_{\mathrm{pol}}(\boldsymbol{r}) = \sqrt{3}(-1)^F m_F \eta \cos(\alpha)\sum_{i=1}^{3}\sin(\boldsymbol{b}_i\boldsymbol{r} - \Delta\phi_{jk}) \tag{3.18}$$

and $V_{2D} = 1/4u(\lambda_L)I_0$ with $I_0 = \frac{2P_0}{\pi w_L^2}\frac{1}{8E_{\mathrm{rec}}}$. Note that the lattice depth V_{2D} is normalized to the channel structure of the A- and B-sites to 1/8 of the overall lattice depth V_0. The angle α defines the orientation of the quantization field $\boldsymbol{B}_{\mathrm{Q}}$ for a rotation around the x-axis as depicted in figure 3.2. As the polarization of the lattice is defined with respect to $\boldsymbol{B}_{\mathrm{Q}}$, the energy offset between the A-B sites ΔV_{AB} can be tuned. Using eq. (3.18) it yields

$$\Delta V_{\mathrm{AB}} = 9\eta m_F V_{\mathrm{2D}}\cos(\alpha). \tag{3.19}$$

Thus, ΔV_{AB} is maximal for $\boldsymbol{B}_{\mathrm{Q}}$ pointing out of the lattice plane ($\alpha = 0°$ and $180°$) and minimal with degenerate A-B-sites for $\boldsymbol{B}_{\mathrm{Q}}$ pointing parallel to the lattice plane ($\alpha = 90°$). In section 4.3.1 the influence of $\boldsymbol{B}_{\mathrm{Q}}$ on the band structure is further elaborated. Note that the spin-dependent potential can also be defined with an effective magnetic quantum number $m = (-1)^F m_F \cos(\alpha)$ [38], which is useful for expressing the potential independently from the internal state.

3.2.2 Band structure of the honeycomb lattice

When neglecting interactions the energy spectrum of a quantum gas in an optical lattice can be reduced to solving the stationary Schrödinger equation for a single-particle wave function

$$\hat{H}\psi_{\boldsymbol{q}}^n(\boldsymbol{r}) = E_{\boldsymbol{q}}^n\psi_{\boldsymbol{q}}^n(\boldsymbol{r}) \tag{3.20}$$

where the Hamiltonian for the lattice is given by

$$\hat{H} = \frac{\hbar^2}{2m}\Delta^2 + V_{\mathrm{lat}}(\boldsymbol{r}), \tag{3.21}$$

n denotes the band index and q the quasimomentum. The lattice is periodic with the period of the lattice vectors $V_{\mathrm{lat}}(\boldsymbol{r} + \boldsymbol{a}_i) = V_{\mathrm{lat}}(\boldsymbol{r})$. This problem has been solved by F. Bloch for electrons in solid states [96, 97]. The solutions of $\psi_{\boldsymbol{q}}^n$ are the so called Bloch functions of the form

$$\psi_{\boldsymbol{q}}^n(\boldsymbol{r}) = e^{i\boldsymbol{q}\boldsymbol{r}}u_{\boldsymbol{q}}^n(\boldsymbol{r}) \tag{3.22}$$

having the same periodicity as the lattice potential in space. Also regarding quasimomentum the wave function $u_{\boldsymbol{q}+\boldsymbol{G}}^n(\boldsymbol{r}) = u_{\boldsymbol{q}}^n(\boldsymbol{r})$ and the eigenenergies $E_{\boldsymbol{q}+\boldsymbol{G}}^n = E_{\boldsymbol{q}}^n$ are periodic upon the reciprocal lattice vector $\boldsymbol{G}$. This allows us to define the lattice potential and the Bloch function as Fourier series

$$V_{\mathrm{lat}}(\boldsymbol{r}) = \sum_{G} V_{\boldsymbol{q}}e^{i\boldsymbol{G}\boldsymbol{r}}, \tag{3.23}$$

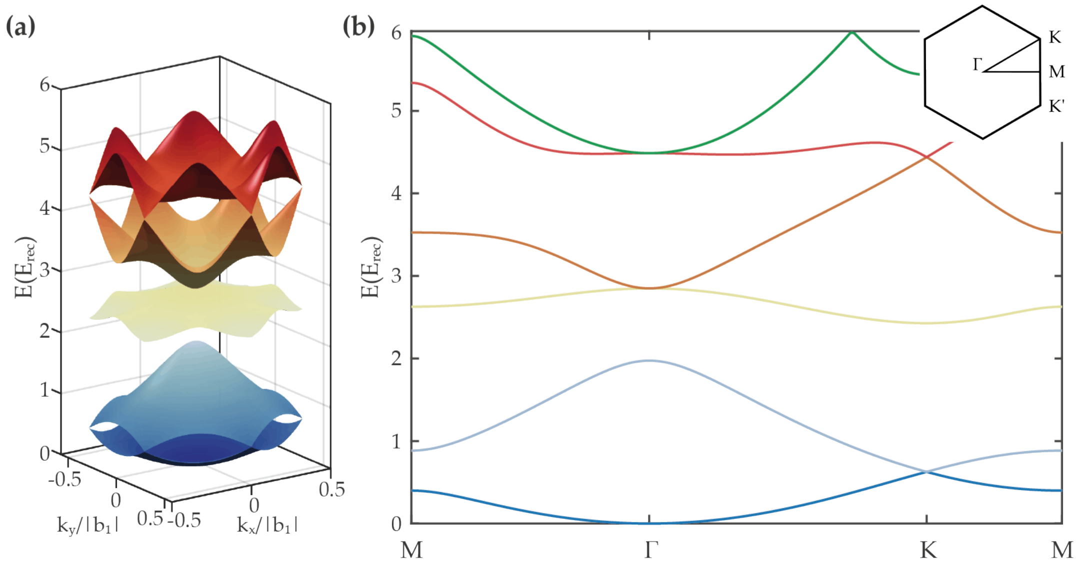

FIGURE 3.4: Band structure of the honeycomb lattice in the single particle approximation for a lattice depth of $V_{2D} = 1\,\mathrm{E_{rec}}$ for $|2,-2\rangle$ and a quantization-axis pointing in the lattice plane canceling the AB-offset ($\alpha = 90° \mathrel{\widehat{=}} \Delta V_{\mathrm{AB}} = 0$). (a) Shows the first five bands in the honeycomb lattice. For a shallow lattice as shown here, the bandwidth is on the order of $1\,E_{rec}$, which becomes smaller in deep lattices. (b) Band structure of the first six bands along the high-symmetry path of M, Γ, K and M-points. Clearly visible are the closed Dirac cones between the first and second band and between the fourth and fifth band at the K- and K'-points.

$$\psi_{\boldsymbol{q}}^{n}(\boldsymbol{r}) = \frac{1}{\sqrt{\mathrm{N}}}\sum_{\boldsymbol{G}} C_{\boldsymbol{q},\boldsymbol{G}}^{n} e^{i\boldsymbol{G}\boldsymbol{r}} \tag{3.24}$$

where the latter is normalized to the number of unit cells N of the considered system. Substituting this ansatz into eq. (3.20) reformulates the Schrödinger equation in reciprocal space and results in an eigenvalue problem

$$\sum_{j}\left(\frac{\hbar^2}{2m}(\boldsymbol{q}-\boldsymbol{G}_i)^2\delta_{ij} + V_{\boldsymbol{G}_j-\boldsymbol{G}_i}\right)C_{\boldsymbol{q}}^{n,j} = E_{\boldsymbol{q}}^{n} C_{\boldsymbol{q}}^{n,i}. \tag{3.25}$$

In principle a solution for many quasimomenta seems demanding, but in practice the determination of about 10 coefficients is sufficient. An efficient numerical calculation of the band structure of the hexagonal lattice has been implemented by Alexander Ilin and will be described in detail in his thesis. All band structure calculations presented in this thesis are based on this implementation.

An exemplary band structure of the hexagonal lattice for a non-interacting particle is depicted in figure 3.4. In this example, the lattice depth $V_{2D} = 1\,\mathrm{E_{rec}}$ is shallow and the quantization axis points in the lattice plane ($\alpha = 90°$), thus the energy offset between the A- and B-sites vanishes ($\Delta V_{\mathrm{AB}} = 0$). Here, the dispersion relation features a linear relation, the so-called Dirac cones, at the K- and K'-points between the first and second Bloch band and between the fourth and fifth Bloch band. Note that the K- and K'-points are energetically degenerate and inhibit a topological singularity with a Berry flux of π.

The control of Δ_{AB} is central for the Landau-Zener transfer to higher bands and allows for lifting the degeneracy of the A- and B-sites [38, 39]. The Dirac cones can be opened and the band gap between the different bands can be tuned continuously (see appendix A.1 for an overview of the band structure). Furthermore, the geometry of the Bloch bands defines the macroscopically occupied quasimomenta of the BEC. For the relevant bands in this thesis these are the Γ-points for the first and fourth band and the K- and K′-points in the second band.

3.2.3 Confinement of the lattice tubes

The lattice potential can be imagined as an array of tubes localized at the lattice sites. Thereby, the shape of the tubes is characterized by the radial and the longitudinal tube extension. Both quantities depend on the lattice depth V_{2D} and the energy offset ΔV_{AB}, respectively the angle α of the quantization axis. In the following the radial and the longitudinal confinement of the hexagonal lattice are presented.

The radial confinement for the central tubes of the hexagonal lattice is given by the following analytic expression

$$\omega_{\perp_{\mathrm{A,B}}}(V_{\mathrm{2D}}, \alpha) = \frac{3\pi}{\lambda_L}\sqrt{\frac{V_{\mathrm{2D}}}{m_{\mathrm{Rb}}}\Big(2 \mp 3(-1)^F m_F \eta(\lambda_L)\cos(\alpha)\Big)}. \tag{3.26}$$

The confinement scales with $\sqrt{V_{2D}}$ and depends on α. In figure 3.5 (a) the radial confinement is plotted for the realizable parameter range of the hexagonal lattice. With the current setup it reaches up to ∼50 kHz for $\sqrt{V_{2D}} = 20\,\mathrm{E_{rec}}$.A rapid tilt of the quantization axis changes significantly the radial confinement, e.g. from 33.3 kHz for $\alpha = 0°$ to 26.7 kHz for $\alpha = 106°$ at fixed $\sqrt{V_{2D}} = 8\,\mathrm{E_{rec}}$.

In contrast, in direction of the tubes, the longitudinal confinement is orders of magnitude lower (at $8\,\mathrm{E_{rec}}$ about 75 Hz), thus $\omega_z \ll \omega_{\perp_{\mathrm{A,B}}}$. The numerical calculations show only a weak influence of α as depicted in figure 3.5 (b) for α =0°, 90° and 180°. Neglecting the dependency of the energy offset an analytic expression for the longitudinal confinement of the hexagonal lattice yields

$$\omega_z = 2\sqrt{\frac{6V_{\mathrm{2D}}E_{\mathrm{rec}}}{w_L^2 m_{\mathrm{Rb}}}}. \tag{3.27}$$

The overall harmonic confinement including the confinement of the dipole trap is given by

$$\omega_{\mathrm{tot_z}} = \sqrt{\omega_{\mathrm{DT_z}}^2 + \omega_{\mathrm{Latt_z}}{}^2}. \tag{3.28}$$

The longitudinal confinement is straightforward to measure by exciting dipole oscillations along the z-direction. Therefore, we have ramped up the hexagonal lattice in 100 ms and excited center of mass oscillations for the ensemble of lattice tubes by applying a magnetic field gradient for 1 ms. From absorption images the center-of-mass position of the atomic cloud is extracted and fitted with an exponentially

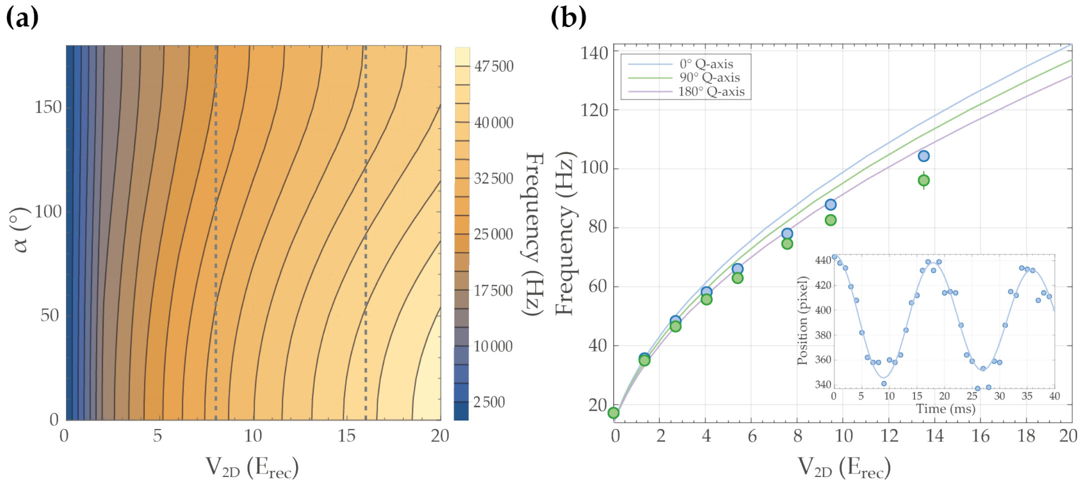

FIGURE 3.5: Radial and longitudinal confinement in the honeycomb lattice. (a) Radial confinement of a central lattice site as a function of lattice depth V_{2D} and quantization axis angle α. Vertical dotted lines mark $V_{2D} = 8\,\mathrm{E_{rec}}$ and $16\,\mathrm{E_{rec}}$, which are relevant in chapter 5. (b) Longitudinal confinement along the z-direction as a function of lattice depth V_{2D} and quantization axis angles α. The confinement for α =0°, 90° and 180° is obtained by numerical calculations for the central lattice tube (solid lines). This is compared to a measurement of dipole oscillations for α =0° and 90° (blue and green circles) excited along the tube direction (z-direction) by a magnetic field gradient. The inset depicts exemplarily the center of mass position of the atomic cloud for different holding times at $V_{2D} = 4\,\mathrm{E_{rec}}$. The fit with an exponentially damped sine yields a frequency of 55.7(3) Hz. The errors of the fits are typically smaller than the data points.

damped sine as illustrated in the inset of figure 3.5 (b). These measurements are repeated for different V_{2D} and α. The obtained oscillation frequencies are depicted in figure 3.5 (b) and show a good agreement with the numerically calculated longitudinal confinement for the central tube. Note that the case $\alpha = 180°$ is equivalent to $\alpha = 0°$ as always the deeper AB-lattice site is populated.

To conclude, the confinement of the lattice tubes changes over a large range in dependency of α and V_{2D}. A rapid modification of these parameters with a fast lattice ramp or a tilt of the quantization axis might thus excite dipole or breathing modes in the lattice as for example observed by Moritz et al. [98].

3.3 Detection methods

A BEC is typically detected after free ballistic expansion under gravity (∼38 ms at this experiment) by shining a collimated resonant light beam onto the atoms. The resulting absorption profile is imaged by an objective (here with a magnification ∼3) and a CCD camera. Similar detection methods can also be applied to optical lattices where one differentiates between two methods: time-of-flight (TOF) and band mapping (BM). The former reveals the quasimomentum distribution while the latter gives access to the momentum distribution [21]. At the experiment we have two imaging directions available: one in the lattice plane (x-y-plane) and one in the tube plane (y-z plane) of the 2D-hexagonal lattice (cf. section 1.1).

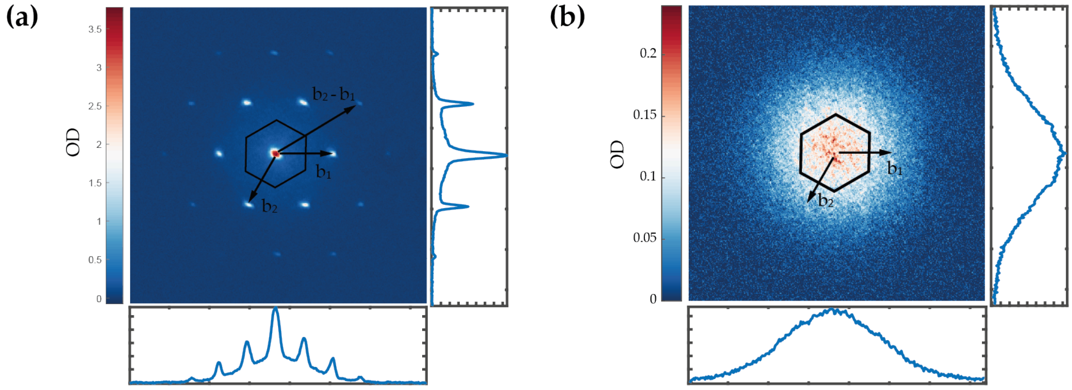

FIGURE 3.6: Time-of-flight (TOF). Absorption images of a BEC in the 2D-hexagonal optical lattice after a sudden release from the optical potentials and free-ballistic expansion of 35 ms. (a) TOF image of a shallow lattice $V_{2D} = 3\,E_{rec}$. The higher order Bragg peaks are clearly visible, indicating phase coherence and thus a large superfluid fraction. (b) TOF image of a deep lattice $V_{2D} = 8\,E_{rec}$ after 2 ms holding time. Bragg peaks are not visible indicating the absence of a global phase coherence in the system. The FWHM of Gaussian fits to the profiles yield 1.9 in units of the reciprocal lattice vector $\boldsymbol{b}_1$.

3.3.1 Time-of-flight

A time-of-flight measurement requires a sudden release from the confining potentials i.e. the dipole trap and the lattice followed by a subsequent ballistic expansion. After the release the matter-waves located at the different lattice sites expand and interfere. The expansion of the matter-waves results in a characteristic regular interference pattern when the spatial phase coherence is large compared to the lattice constant. Ideally assuming an infinitely long time-of-flight the inference pattern corresponds to the in-situ momentum distribution.

An exemplary TOF image is depicted in figure 3.6 (a) of the shallow 2D-hexagonal optical lattice $V_{2D} = 3\,E_{rec}$. Here, the interference peaks, also called Bragg peaks or coherence peaks are located at quasimomenta, which are linear combinations of the reciprocal lattice vectors. However, momentum space is only entered in the far-field, which here is not reached for a finite time-of-flight expansion of $\sim$38 ms. This aspect and finite size effects such as the harmonic trap, resolution and interactions can significantly alter the measured distribution [99] e.g. broadening of the Bragg peaks. These effects can be accounted for in ab-initio Quantum Monte Carlo simulations, which can be used to obtain the temperature in the lattice [100]. Experiments directly measuring in the far-field are very rare as for example the metastable Helium experiment in Orsay [101].

The Bragg peaks begin to blur in deeper lattices. They vanish completely for shorter coherence lengths (see figure 3.6 (b)). These effects are typically captured by the visibility which is defined as

$$\mathcal{V} = \frac{n_{\mathrm{TOF}}(\boldsymbol{k}_{\max}) - n_{\mathrm{TOF}}(\boldsymbol{k}_{\min})}{n_{\mathrm{TOF}}(\boldsymbol{k}_{\max}) + n_{\mathrm{TOF}}(\boldsymbol{k}_{\min})} \tag{3.29}$$

where n_{TOF} is the density distribution around the maximally occupied momenta and the minimally occupied momenta located at the same radius from the center of the image. This formulation cancels the envelope of the Wannier function [99]. An example for evaluation of the visibility is discussed in appendix C.2. Further observables can be obtained by bimodal fits to the Bragg peaks in order to estimate the superfluid fraction or by evaluating the optical density.

3.3.2 Band mapping

Band mapping is the adiabatic ramping down of the lattice potential followed by ballistic expansion. With this method the band population and the quasimomentum $\boldsymbol{q}$ can be mapped to the respective Brillouin zones. Figure 3.7 (a) illustrates the technique. The first and second Bloch band are depicted in the reduced zone scheme with occupied quasimomenta at Γ- and at K-points. The adiabatic ramping down of the lattice potential maps the quasimomentum $\boldsymbol{q}$ onto the harmonic confinement of the dipole trap, which approximately corresponds to the free particle momentum $\boldsymbol{p}$. The different momentum intervals can be associated with the nth Brillouin zone of the lattice. The quasimomenta are preserved when the ramp time of the lattice potential is slow compared to the band gap $\Delta/\hbar$. This condition becomes increasingly difficult to fulfill in very shallow lattices e.g. at the edge of the Brillouin zone at the K- and K′-points, where the band gap is small or even closed (depending on ΔV_{AB}). Furthermore, the ramp down should be fast compared to the redistribution of $\boldsymbol{q}$ within the band and fast with respect to dipole oscillations ($< 5\,\mathrm{ms}$). The ramp down time thus depends on the starting lattice depth i.e. in deep lattices typically an exponential ramp fulfills the adiabatic condition. In figure 3.7 (b) a realization of a linear and exponential ramp of 2 ms are compared. The band gaps between the first and second Bloch band $\Delta_{\Gamma\Gamma}$ and $\Delta_{\Gamma K}$ first decrease linearly, while they increase for very shallow lattices. Experimentally the exponential ramp showed a better mapping to the different Brillouin zones depicted in figure 3.7 (c). An exemplary band mapping image is shown in figure 3.7 (d). The atoms were loaded in a deep lattice of $V_{2D} = 8\,\mathrm{E_{rec}}$, where we observe a broadening of the distribution at the Γ-point and a significant spread of the population in the Brillouin zone. The FWHM is half the length of a reciprocal lattice vector. Band mapping images with population in higher bands are presented in chapter 4 and 5.

3.4 Upgrade of the intensity and phase control

For both detection methods the new intensity control proved valuable. Its high band width ensures that not only in shallow but also in deep lattices a fast exponential ramp for band mapping can be performed. Here, the most critical point is the transition from holding the lattice depth to the steep exponential ramp of 2 ms. The slopes for all three lattice beams must be equal in shape and begin simultaneously in order to image a symmetrical Brillouin zone. In this regard also for TOF imaging the simultaneous switch off of all trapping potentials ($\sim 1\,\mu\mathrm{s}$) is crucially important.

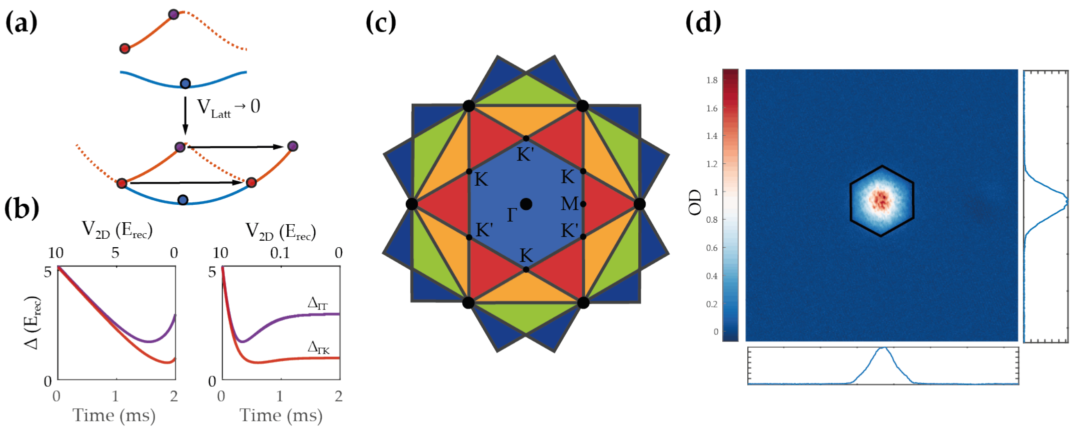

FIGURE 3.7: Band mapping. (a) Adiabatic ramping down of the lattice potential maps the quasimomentum $\boldsymbol{q}$ onto the free particle momentum $\boldsymbol{p}$ in the nth Brillouin zone of the lattice. The first and second Bloch band are depicted in the reduced zone scheme with occupied quasimomenta at Γ and at K-points, which are preserved during ramping down. (b) Band gap Δ of the 2D-hexagonal lattice for a linear (left) and exponential ramp down (right) of the lattice depth V_{2D} in 2 ms. Δ is depicted between the first and second Bloch band from $\Gamma \rightarrow \Gamma$ (violet) and $\Gamma \rightarrow K$ (red) for $\alpha = 106°$ and $|2,-2\rangle$. (c) The first five Brillouin zones of the honeycomb lattice with the characteristic symmetry points: Γ, M, K and K'. (d) Absorption image after band mapping for a lattice depth $V_{2D} = 8\,E_{rec}$ and holding time of 2 ms with horizontal and vertical profiles. The FWHM of Gaussian fits to the profiles yield 0.5 in units of the reciprocal lattice vector $\boldsymbol{b}_1$.

3.4.1 Optical setup of the honeycomb lattice

The light source of the lattice setup is a titanium-sapphire laser (Ti:Sa) which is pumped with an 18 W diode laser at 524 nm. The Ti:Sa is a tunable ring laser at 830 nm with an output power of 4.3 W. The laser itself contains a sophisticated lock technique to ensure single mode operation at a bandwidth smaller than 80 kHz. It contains thick and thin etalons and a reference cavity which if adjusted properly assure a stable wavelength. The downside of the etalon lock technique are small intensity modulations in our case at 91 kHz and its higher harmonics. The development of a high bandwidth intensity control has the potential to reduce these modulations.

The Ti:Sa beam is split into three laser beams (see figure 3.8 for the lattice setup). Each one passes through two acousto-optical modulators (AOM). One is dedicated for shaking the lattice by frequency modulation (e.g. [102]) and one for the intensity control. After the AOMs, the beam is coupled into a single mode fiber of about 30 m length. At its end a circular Gaussian beam with a focus at 60 cm to 80 cm and waist of 115 µm is created. Before it is propagated to the experiment, a small fraction is used for a photodiode for the intensity control. We reach maximum intensities on the order of 300 mW directly in front of the science chamber. In practice this corresponds to lattice depths in the range of $V_{2D} = 20$ Erec though for an ideal lattice setup higher lattice depths should be achieved with the available laser power.

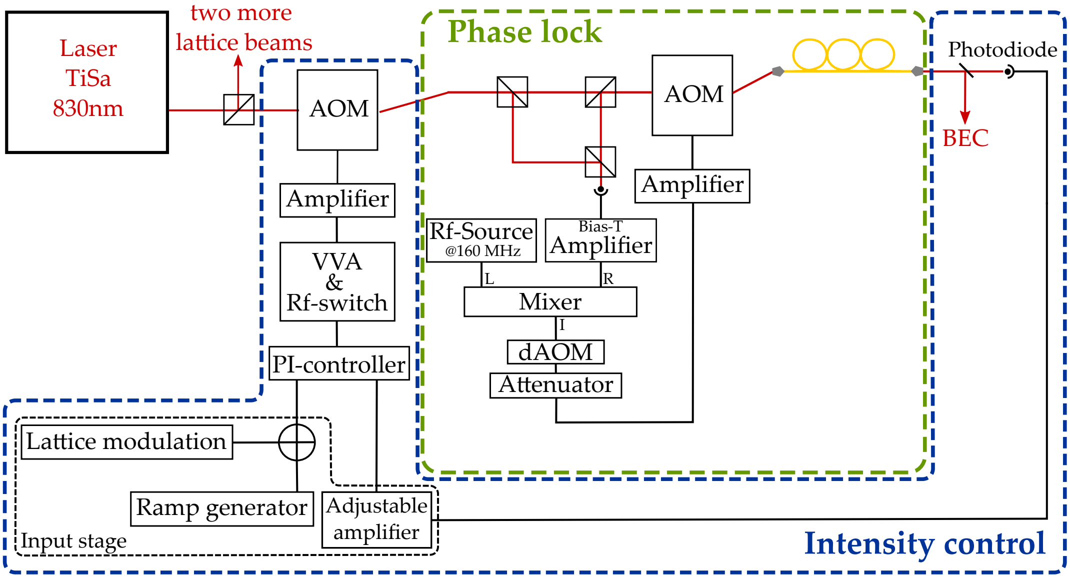

FIGURE 3.8: Schematic of the intensity control and phase lock of the lattice laser system. After the TiSa the beam is split into three parts for the lattice beams. Each arm contains two AOMs, one for the intensity control and one for the phase lock. The newly developed intensity control works with a voltage variable attenuator (VVA) instead of a mixer for compatibility with high-bandwidth PI-controllers. The phase lock stabilizes the phase up to the end of the fibertip. It has been tested with a digital AOM driver (dAOM).

3.4.2 Intensity control

A typical experimental sequence for the lattice intensity control first begins with an exponential ramp of about 100 ms to a certain intensity level, followed by a variable hold time for an experiment in the lattice and at the end a sudden switch-off to perform time-of-flight imaging or a fast exponential ramp down of $\sim$ 1 ms to perform band mapping. In addition, lattice calibration via amplitude modulation requires an modulation of up to $\sim$ 50 kHz. Last but not least, the intensity noise of the light should be reduced significantly. At the beginning of this PhD project the intensity control built originally at the experiment was not able to provide all these features accurately enough for measurements in deep lattices with high laser power. Therefore, the author set in cooperation with J. Seeger to develop three independent intensity controls.

The electronic part of the intensity control has been designed as follows. The main part constitutes the PI(D)-controller for which we choose a commercial solution[1]. This in turn required electronic development on our side in order to integrate all requirements for an intensity control:

- a high-bandwidth input stage in front of the PI-controller. It contains an input port for the photodiode[2] with a high precision potentiometer adjusting the

[1]Newport LB1005 Servo Controller
[2]Thorlabs PDA155

gain up to a factor of 10. This feature is especially valuable for the lattice calibration. In addition, it contains monitor ports for each voltage signal and a reference voltage stage, where the lattice modulation is added.

- a voltage-variable attenuator (VVA) board. It contains a VVA[3] replacing the mixer[4] used in our group. The main reason is that to our knowledge no commercially available PI-controller could drive the current-driven mixer. In addition, the VVA features a high bandwidth, though in the implemented surrounding circuits of the VVA a significant phase lag is accumulated, which limits the bandwidth of the intensity control to several hundred kilohertz. The board also contains an rf-switch[5] ($< 1\,\mu s$) for an immediate and simultaneous switch off of all three laser beams, which is important to obtain a symmetric ordering of the Bragg peaks. The output rf-signal of the VVA unit is amplified[6] by 45 dB before being send to the AOM in the lattice setup.

- a reference voltage programming unit. To drive three independent lattice ramps which are phase locked to each other we implemented a commercial arbitrary waveform generator[7]. It is programmed over a GPIB-port via a Rasperry-PI set up as a server for receiving commands of the LabView experimental control.

The most important characteristics of the intensity control are summarized in figure 3.9 (a)-(c). To summarize an intensity control with a bandwidth of $\sim 150\,\mathrm{kHz}$ has been setup, which fulfills all the requirements stated above. The low frequency noise is clearly reduced as well as the intensity modulations of the lattice laser at 91 kHz which are damped by 20 dB. We have ensured that the lifetimes are similar to the previously used intensity control. Room for optimization is left for the implementation of a feed forward control in order to perform Kapitza-Dirac [103] and in order to use a sequence of short light pulses for loading the lattice [104]. Recently also a new design of a PID controller has been started in our group with an integrated the input stage with support from the author.

3.4.3 Phase noise

As the condensate lifetime in higher bands is short compared to other experiments [33], we considered phase noise as a possible limiting factor for the lifetime. In a first step we replaced the rf-sources[8] of the AOMs, which increased the duration of the visibility in the lowest band. In a second step we characterized the phase noise present at the lattice setup. We measured the relative phase noise in a Mach-Zehnder interferometer and compared it to the lattice setup. The setup of the Mach-Zehnder

[3] Analog HMC346AMS8GE
[4] Mini-circuits ZAD-3
[5] Mini-circuits RSW-2-25PA+
[6] Mini-circuits ZHL-5W-2G+
[7] TTI TGA12104
[8] Rhode & Schwarz: SMA and SMB

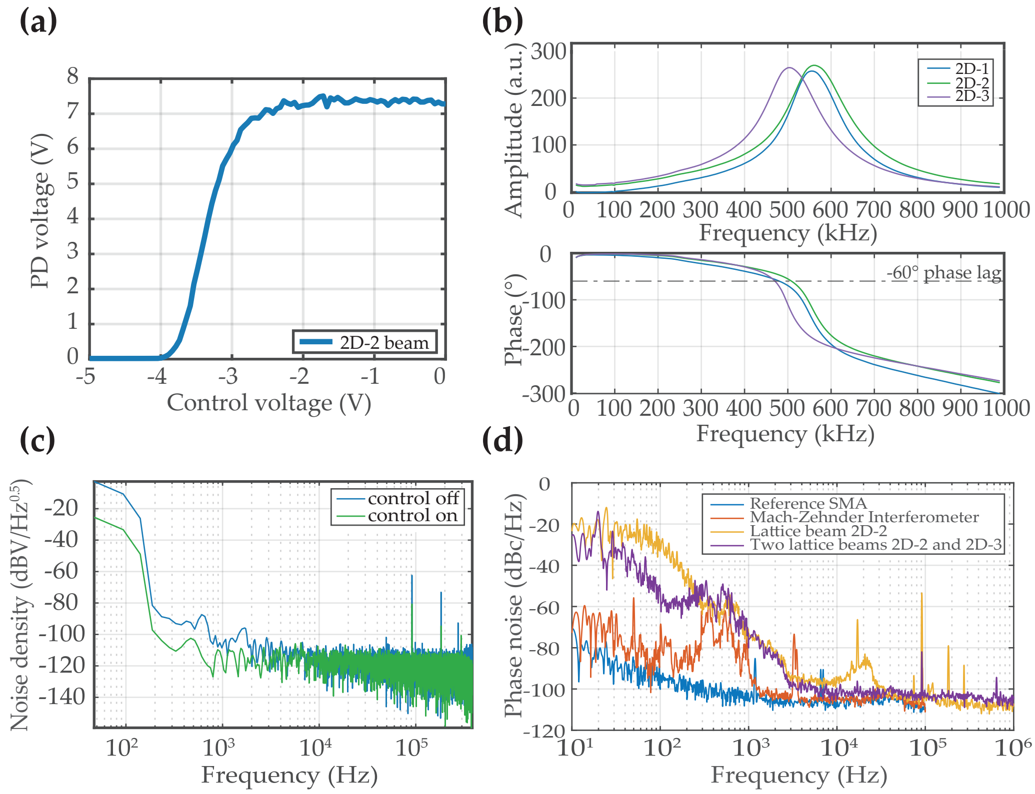

FIGURE 3.9: Characteristics of the intensity control and phase noise. (a) Photodiode voltage versus the control voltage at the VVA. The behavior can be linearized in a future development of the circuit. (b) Bode diagram of the control loop without the PI-controller. The strong resonance at 500 kHz imposes an upper limit on the bandwidth. (c) Noise density of the intensity control. The low frequency noise is clearly reduced as well as the intensity modulations of the lattice laser at 91 kHz which are damped by 20 dB. (d) Phase noise of different test setups for comparison with the lattice setup. The phase noise in the fibers of the lattice beams is significantly higher than in a separate Mach-Zehnder inferometer.

interferometer contains two arms. In one arm the frequency is shifted by 80 MHz with an AOM. The light of the two arms is superimposed via a beam splitter onto a fast low-noise high-pass photodiode[9]. Its signal is amplified[10] and connected to an spectrum analyzer[11] to measure the relative phase noise between the different arms. In figure 3.9 (d) the results are depicted. For reference an electronic rf-device has been measured (blue curve). The Mach-Zehnder interferometer only shows a slightly higher phase noise (red curve).

The measurement of the relative phase noise of the lattice beams is significantly higher, which is measured as follows. The light travels trough an approximately 30 m long fiber. At the end of the fiber tip 4 % are reflected back and superimposed at the photodiode (compare figure 3.8 for a sketch of the setup). Especially for lower frequencies below $\sim$ 400 Hz the phase noise in the fibers is about 20 dB higher than in the small Mach-Zehnder setup consisting only of few mirrors. Furthermore, the phase noise between two of the long lattice fibers is still on a considerable level (violet curve). These measurements suggest that a reduction of the phase noise is desirable.

To do so, we have tested a phase lock system developed in our group. It is based on a digital AOM driver with real time units. For a short general introduction see the PhD theses of A. Kerkmann [105] and D. Vogel [106]. The electronic tests of the phase lock implemented in our setup have been successful. However, in the experimental cycle two main issues need to be solved. For very small lattice depths the photodiode signal is too small to determine the phase of the laser beams. This requires switching on the phase lock at intermediate lattice depths, which causes a sudden phase shift with oscillations around the setpoint. The mixer used for measuring the phase can determine the phase up to π and not 2π. Due to the complexity of a phase lock, which is required for at least two lattice beams, it is best to avoid it and optimize the passive phase stability of each lattice beam as good as possible.

3.5 Conclusion and outlook

In this chapter, important characteristics of the central optical potentials, the dipole trap and the optical honeycomb lattice, have been introduced. The tunability of the AB-energy offset is emphasized, which is central for the transfer to higher Bloch bands. In addition, the radial and the longitudinal confinement of the lattice sites have been calculated as they are relevant in deep lattices. The longitudinal harmonic confinement in the 2D-honeycomb lattice has also been measured resolving the influence of the AB-potential offset. In order to characterize superfluids in higher bands the detection methods, time-of-flight and band mapping, have been discussed.

[9]Hamamatsu G8370-03 with a Bias-tee ZFI3T-6GW
[10]Mini-circuits ZFL-500
[11]Rhode & Schwarz: FSV7

Furthermore, a new intensity control for the three lattice beams with a bandwidth of $\sim$ 150 kHz has been presented. It consists of voltage-variable attenuators (VVA) in combination with analogue PIDs. The implemented precision gain has paved the way for engineering the band structure via intensity adjustments of the lattice beams. Detection with time-of-flight and band mapping measurements has been improved by the rapid switching and ramping capabilities.

Finally the phase noise of the three lattice beams has been characterized as it can be one of the limitations for the lifetime of superfluids in higher bands. On the one hand the measurements indicate that a reduction is desirable, which could be already achieved by relocating the lattice setup to shorten the optical fiber (3 m instead of 30 m). An active phase stabilization requires further development effort. On the other hand similar three beam lattice setups report no significant disturbance by phase noise [107, 108]. To clarify direct measurements with a quantum gas are planned. First, a measurement of the atom loss from the ground band in dependence of the lattice depth and the holding time gives access to heating rates following the approach for a low-noise optical lattice [109]. Second, translations of the lattice potential are induced by phase noise. They can be measured with single-site resolution by implementing the recently published quantum gas magnifier in our setup [110].

Chapter 4

Transfer to higher Bloch bands

Preparing condensates in higher Bloch bands promises vast possibilities to realize exotic states. This requires a reliable preparation of the system. As bosons in optical lattices are typically prepared in the ground state, the challenge is to implement an optimal transfer method. In this chapter we present the basic working principle of the transfer and discuss a selection of methods, which strongly differ in transfer efficiency and experimental practicability to prepare metastable condensates in higher bands. Our method of choice is the rotation of the quantization axis corresponding to a rapid quench of the AB-offset of the hexagonal lattice. We discuss its experimental implementation, the experimental sequence and the measured transfer efficiency to higher Bloch bands. In addition, we perform a coherent transfer to the second Bloch band forming a superposition state between the first and the second band. For the condensation dynamics and the lifetime of metastable states in higher Bloch bands we refer the reader to chapter 5. The experimental data presented in this chapter has been measured with main contributions by the author in collaboration with A. Ilin and J. Seeger. The data evaluation presented in this chapter has been conducted by the author.

4.1 Working principle

Typically BECs are prepared in a harmonic trap from which they are loaded into the ground state of an optical lattice assuming adiabacity. In the superfluid phase the momentum spread of the condensate is small and its phase is uniform across the occupied lattice sites. The ground state in the first Bloch band of the hexagonal lattice has a minimum at the Γ-point from which various transfer paths to higher Bloch bands are possible. The state in the higher Bloch bands is different from the ground state in terms of tunneling, interaction and the form of the Bloch state itself. The final characteristics of the prepared state can widely be modified by lattice depth and energy offset. Before discussing this it is of course first desirable to optimize the transfer such that the population in the excited Bloch band is maximized.

A precondition is that the overlap of the initial state with the final state is nonzero. This on the one hand reduces the available parameter space and on the other hand sets an upper limit for the maximum possible transfer efficiency. Further, the transfer

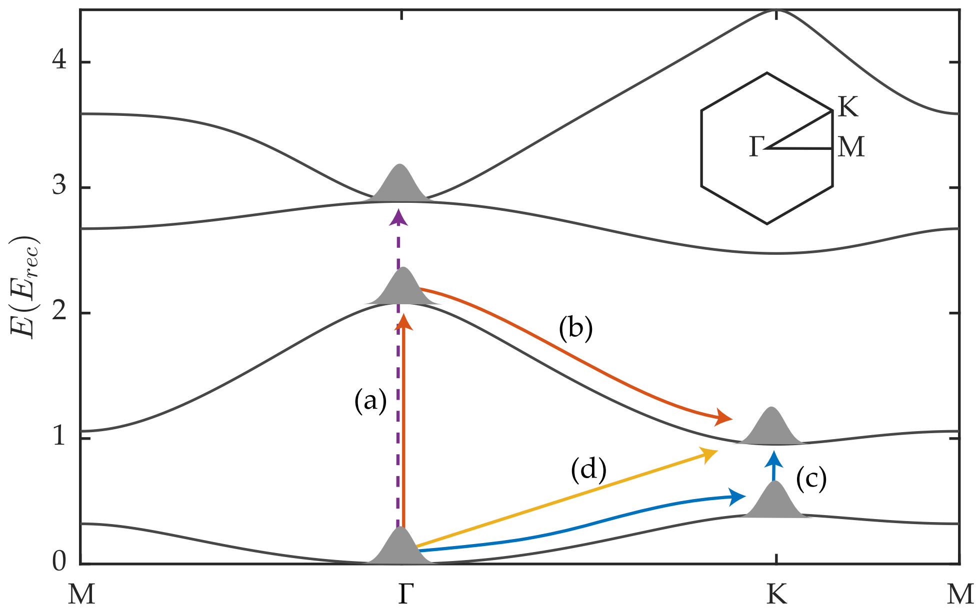

FIGURE 4.1: Transfer paths to higher Bloch bands in an optical lattice. The band structure is sketched up to the fourth Bloch band of the hexagonal lattice at a lattice depth $V_{2D} = 1\,E_{rec}$ with an AB-offset $\Delta V_{AB} = 1\,E_{rec}$. Initially the condensate is prepared at the Γ-point at quasimomentum $\boldsymbol{q} = 0$. Via a resonant transition (a) the minimum of the fourth band can be populated. In order to populate the minimum of the second band (K-points, $\boldsymbol{q} \neq 0$) different transfer paths (b), (c) or (d) are possible involving both an energy and momentum transfer.

efficiency depends on the chosen experimental transfer method either transferring energy or energy and momentum. Some possible methods are amplitude modulation, lattice acceleration or Raman transitions.

Therefore, different transfer paths to higher Bloch bands are illustrated in figure 4.1. The simplest transfer is a resonant transition without any momentum transfer. In figure 4.1 this corresponds to path (a). The transfer occurs to the minimum of the fourth band located as well at the Γ-point. In contrast in path (b) the transfer occurs to the second Bloch band where the atomic ensemble is transferred to the maximum located at the Γ-point. Thus, an intriguing physical question is how the process of relaxation to the energetic minimum of the second band at the K-points occurs and what the consequences are for the lifetime compared to transition (a).

In (c) first the momentum and then the energy are transferred, which can be realized by a combination of transfer methods. In (d) both occurs simultaneously. For example, this transfer can be realized by Raman transitions, where the energy dissipation from path (b) is circumvented. Thus, it is interesting to compare different transfer methods. In chapter 5 implementations of path (a) and (b) are compared also with respect to the lifetime of the prepared states. In the following we focus on the transfer efficiency of several implemented transfer methods.

4.2 Transfer methods

4.2.1 Resonant transitions

Already early with the emergence of optical lattices various methods have been used experimentally to populate higher bands [111]. Since then further methods have been developed not always with the aim to populate higher bands but instead often being a tool to perform lattice spectroscopy or analyze prepared states. In the following we discuss a selection of resonant transfer methods we have investigated experimentally.

Amplitude modulation

Amplitude modulation relies on sinusoidal periodic intensity modulation [112] conserving the quasimomentum. It can be used as a spectroscopy method for lattice calibration in 1D, 2D and 3D optical lattices. Two different regimes are distinguished. Parametric heating relies on small modulation amplitudes on the order of 2 % of the lattice depth and long modulation times of $\sim$80 ms. In contrast, strong modulations of $\sim$ 20 % of the lattice depth and short durations $<$ 5 ms permit a transfer to higher Bands limiting the temperature increase. Experimentally we have implemented the latter case in order to populate higher bands for the 2D-hexagonal lattice.

In figure 4.2 two exemplary absorption images after band mapping are depicted. Part (a) shows the transfer of a small fraction ($\sim$ 10 %) to the second band in a shallow lattice $V_{2D} = 1E_{rec}$. The population of the second band is localized at the Γ-point at the maximum of the second band (transfer from $\Gamma \rightarrow \Gamma$). After the short modulation of 1 ms three features are observed. First, the population in the second band decays rapidly $<$ 1 ms to the ground band. Second, during the decay oscillations on the Bragg-peaks are present indicating a superposition state between the first and second Bloch band as described in section 4.3.5. Third, during the decay the atomic distribution remains at the Γ-point and does not move towards the K-points. An energy redistribution within the second band does not occur on this time scale (cf. chapter 5).

For comparison figure 4.2 (b) illustrates a different regime at $V_{2D} = 3E_{rec}$with a transfer to the fifth band. In contrast to figure 4.2 (a) the atomic density is homogeneously distributed over the respective Brillouin zones. Especially in the ground band this indicates strong heating processes. Here, different parameter regimes are required.

In conclusion, it is possible to populate higher Bloch bands with amplitude modulation but the method requires a careful parameter choice. As the transfer efficiency to higher bands is small, different transfer methods are suited better.

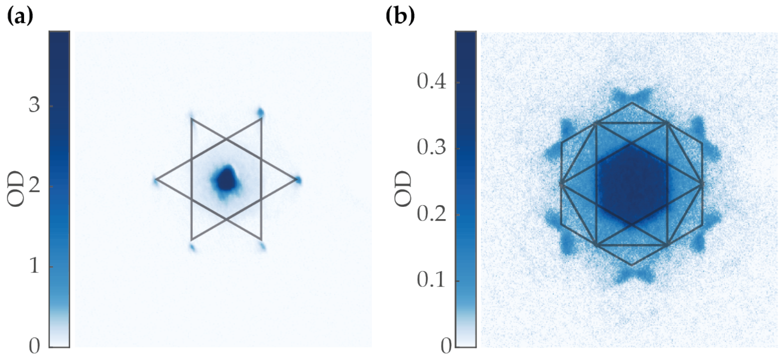

FIGURE 4.2: Transfer to higher Bloch bands in the 2D-hexagonal lattice via amplitude modulation. (a) Band mapping image at $V_{2D} = 1\mathrm{E}_{\mathrm{rec}}$ with a modulation of 1 ms. The first and second Brillouin zones are indicated in grey. A small fraction is transferred to the Γ-points in the second Bloch band in the shallow lattice. (b) Band mapping image of the 2D-hexagonal lattice at $V_{2D} = 3\mathrm{E}_{\mathrm{rec}}$ with a modulation of 1 ms, where the 5th band is populated via amplitude modulation.

RF- and MW-transitions

Two further implemented methods are radiofrequency (RF) and microwave transitions (MW), which both make use of the internal atomic degree of freedom and impart a negligible momentum transfer. The RF-transitions allow for the switching of the $\mathrm{m_F}$-sublevels, while the MW-transitions allow for switching of the $F = 1, 2$ hyperfine manifold (see section 2.1.2). A transfer to higher bands is possible due to the spin-dependency of the hexagonal lattice (compare section 3.2.1). Here, the RF- or MW-frequency is chosen such that the transfer occurs to a higher band in a different atomic state. The additional tuning of the energy offset ΔV_{AB} allows for the realization of versatile band configurations.

For deep enough lattices meaning well separated Bloch bands the transitions can be treated as a two level Rabi problem whose transition probability is strongly governed by the spatial overlap of the initial and final Bloch band. Seminal experiments have been performed in the honeycomb lattice with a superimposed 1D-lattice by M. Weinberg et al. [39, 46]. A fraction of 0.6 could be transferred to the second band.

During this PhD-project we have implemented RF-transitions to higher bands in the 2D-honeycomb lattice. We have used this method for preparing condensates at nonzero quasimomentum in the second band. This transfer method can be used for a direct comparison to the typically used transfer method, the rotation of the quantization axis. A direct comparison of the resulting condensation dynamics is presented in section C.1.

However, all the presented methods require a precise lattice calibration in order to resonantly transfer to higher bands. In deep lattices also interaction shifts should be considered. Thus, the in the following presented methods are more suited when large parameter spaces are explored.

4.2.2 Landau-Zener type transitions

The Landau-Zener model describes a quantum mechanical transition at an avoided crossing. In the simplest case it is analytically solvable for two level systems (Landau, Zener, Stückelberg 1932) but can be also extended to multilevel systems or to several subsequent transitions with a phase accumulated in between realizing Stückelberg interferometry. The two level system is described by a time dependent Hamiltonian. If for $t \to -\infty$ the system is prepared in one adiabatic state then it has a finite probability to populate the other adiabatic state for $t \to \infty$. The probability for such a diabatic transition is given by

$$P_{LD} = \exp(-\pi/\gamma) \tag{4.1}$$

with $\gamma = \frac{4\hbar\beta}{\Delta^2}$ where β is the rate of change of energy levels in time and Δ denotes the coupling between the states. In the following we discuss two methods to realize this kind of transfer.

In the last decade the experimental advances in preparing condensates in higher bands have mainly been driven by the Hemmerich group in a bipartite square lattice [31–33, 35, 36, 113]. The lattice setup features an inferometer like setup, which allows for controlling the phase between the two lattice arms. This allows for changing the AB-energy offset on an extremely short time scale of $\sim$100 µs resulting in a Landau-Zener transfer. With this technique a good transfer efficiency ($\sim$ 60 % to 90 %) can be realized but it is not directly transferable to our three beam running-wave lattice setup of the hexagonal lattice. However, the rotation of the quantization-axis or the a rotation of the polarization of the lattice beams implement physically similarly a tuneable AB-energy offset. Its working principle for the hexagonal lattice is depicted in figure 4.3.

Also possible is the acceleration of lattices in order to exert a force onto the BEC. If the forcing is strong enough a transfer to higher bands is possible in a Landau-Zener type process. In seminal experiments this has been investigated in a 1D optical lattice [114–116]. Browaeys et al. realized transitions up to the third band [29]. Worthwhile mentioning is also Stückelberg interferometry [117]. In brief, it consists of two partical Landau-Zener transitions. A part of the BEC remains in the first band while another part takes the other interferometer path in the second band. After a second Landau-Zener transition, a Stückelberg interference pattern can be observed allowing to determine the band gap, which can then be used to calibrate precisely the lattice depth. In a third set of exemplary experiments, here in a hexagonal lattice, the lattice acceleration was chosen extremely large essentially rendering the two lowest bands degenerate. These strong dynamics can be described in the context of Wilson lines [118].

Inspired by these publications we have also begun first measurements accelerating the lattice in order to transfer atoms to the second band. Problematic here is that the original aim of preparing long lived metastable condensates in the second band

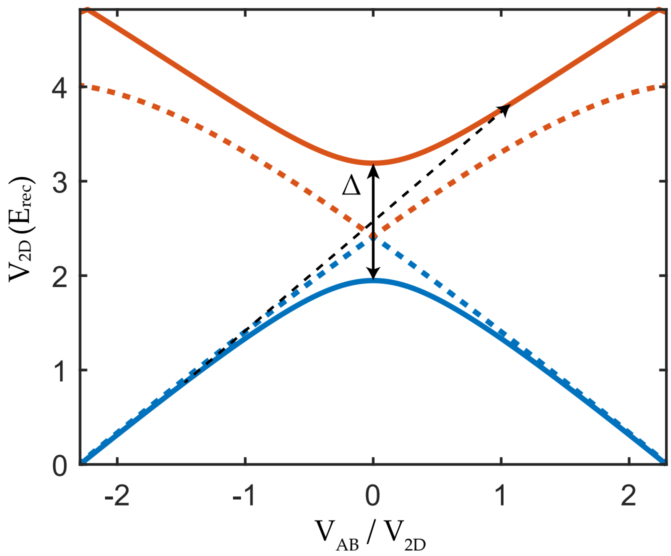

FIGURE 4.3: Principle of the Landau-Zener transfer to higher Bloch bands exemplarily sketched for the bipartite hexagonal lattice at 3 E_{rec}. The first (blue) and second (red) Bloch band are depicted with their respective bandwidth from the Γ (continues line) to K-points (dashed line). Δ denotes the minimal bandgap between the minimum of the first band (Γ-point) and the maximum of the second band (Γ-point). The dashed arrow illustrates a diabatic transfer from $\Gamma \rightarrow \Gamma$. For vanishing ΔV_{AB} the bandgap at the K-points is closed allowing direct transfer to the second band.

is in conflict with the large momentum, which has been transferred to the atoms. However, other interesting effects could be observed, which will be discussed in the PhD thesis of A. Ilin.

4.3 Landau-Zener transfer in the spin-dependent bipartite honeycomb lattice

4.3.1 Rotation of the quantization axis

The rotation of the quantization axis provides the possibility to tune the energy offset ΔV_{AB} in a time-dependent manner, thus realizing the time-dependent Hamiltonian for the Landau-Zener transfer to higher Bloch bands. As depicted in figure 4.4 (a) the system is prepared in the initial state strongly localized on the deeper A-sublattice sites. According to the Landau-Zener model a fraction of the population is transferred to the second Bloch band via a rapid rotation of the quantization axis of more than $\alpha = 90°$ in order to pass over the avoided crossing (see figure 4.4 (c)). Different final states can be engineered depending on the angle α. For instance, the sketched final state here in between the two band crossings (grey circle) shows an s-wave like shape and is as the initial state localized on the A-site (see figure 4.4 (b)). For deep lattices and when further increasing α subsequent Landau-Zener tunneling to higher bands can occur. The probability for such a diabatic transition can be estimated with eq. (4.1). Thus, the faster the energy offset ΔV_{AB} respectively α is tuned, the higher

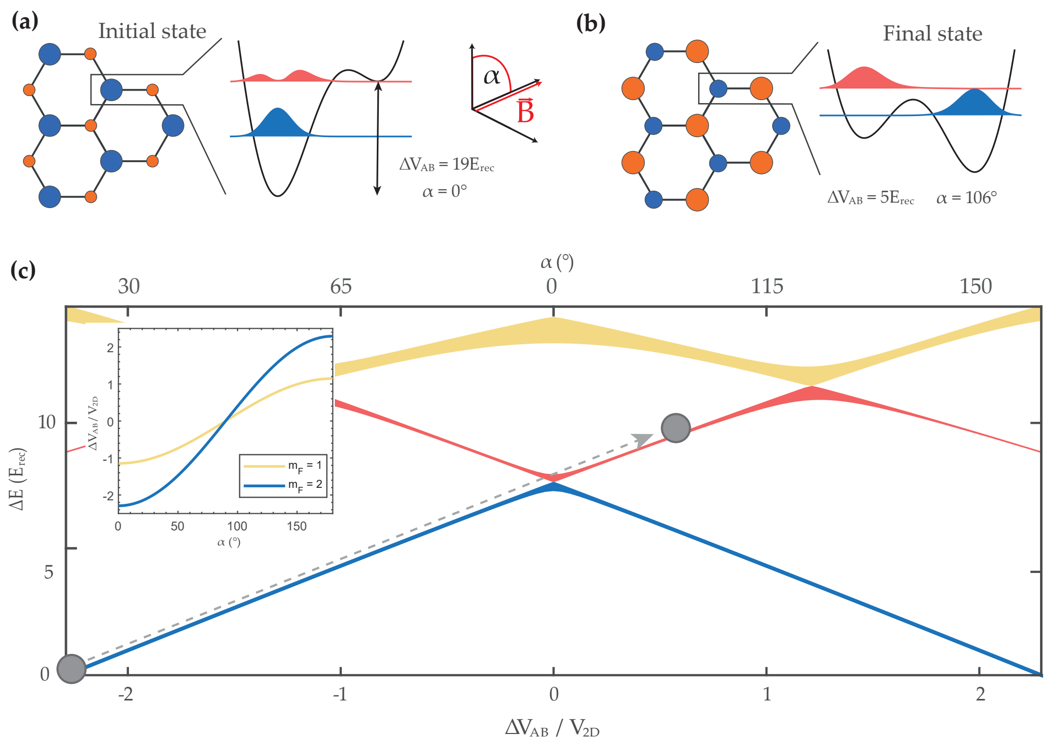

FIGURE 4.4: Transfer to higher Bloch bands. (a), (b) Sketch of the lattice potential with the deep A-sites (blue) and lower B-sites (orange). A cut along the two sites shows a double well with the first (blue) and second Bloch band (red) for the initial state for $\alpha = 0°$ and for an exemplary final state $\alpha = 106°$. (c) Sketch of the Landau-Zener transfer for a lattice depth of 8 E_{rec} and $|2, -2\rangle$ from the initial state to the final state in the second band. Inset: influence of the quantization axis angle α on the AB-energy offset normalized to the lattice depth V_{2D}.

is the transition probability. This circumstance can be further exploited by choosing the energy offset as large as possible: ΔV_{AB} is twice as large when using $m_F = \pm 2$ instead of $m_F = \pm 1$ as shown in the inset of figure 4.4.

4.3.2 Experimental implementation

Initially a quantization axis $\boldsymbol{B}_Q = 2.2\,\mathrm{G}$ is generated by a pair of Helmholtz coils (0.66 G/A) and points in z-direction, which is orthogonal to the lattice plane (cf. section 2.1). Further available pairs of coils in x- and y-direction allow for rotations with arbitrary orientations [47]. We implemented a rotation around the y-axis for which the coil currents follow the form of

$$I_z(t) = I_z(t=0)\cos(\omega t), \ I_x(t) \propto \sin(\omega t) \tag{4.2}$$

as depicted in figure 4.5 (a). The current through both coils is driven by precise bipolar power supplies[1]. The precision on the adjustment of α can be estimated to

[1] High-Finesse BCS 5/12. It contains internal capacitors which connected with a coil function as an RLC. Too short switching times can drive the circuit into resonance. At the experiment the power supplies are voltage driven by an arbitrary waveform generator (TTI 1244), which is programmed by a RaspberryPi-Server connected to the experimental control.

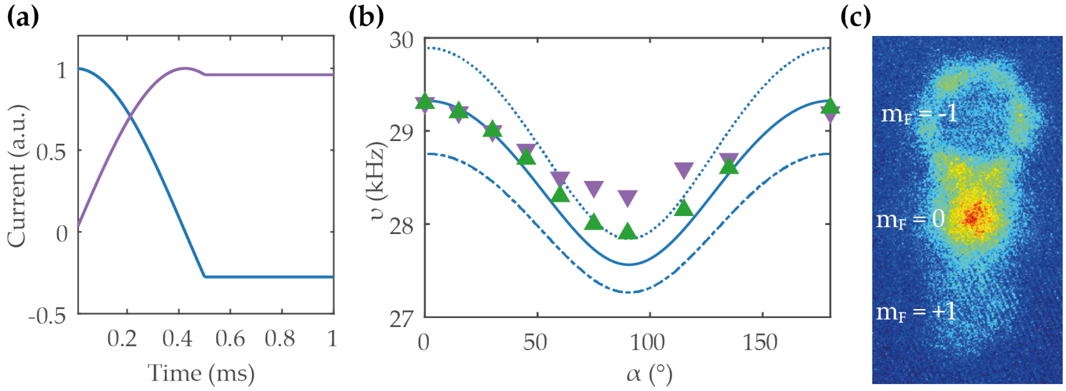

FIGURE 4.5: Rotation of the quantization axis. (a) Currents through the two pairs of Helmholtz coils for a rotation quantization field to $\alpha = 106°$ (blue z-direction, violet x-direction). (b) Influence of α onto the band gap between the first and seventh band at $V_{2D} = 2.9\,\mathrm{E_{rec}}$ (blue line). The band gap is also plotted for $V_{2D} = 3.0\,\mathrm{E_{rec}}$ (blue dotted) and slightly lower $V_{2D} = 2.8\,\mathrm{E_{rec}}$ (blue dashed). Via parametric heating the influence of α is measured. The parametric resonances are depicted for a very shallow dipole trap (green) and for a 5% deeper trap shifting some of the resonances (violet). (c) Spin-flips from the initial state $|1, -1\rangle$ to the other two m_F-components during a transfer to the second band. Absorption image after band mapping and Stern-Gerlach separation ($\boldsymbol{B}_Q = 0.33\,\mathrm{G}$ and $\tau_{rot} = 30\,\mu\mathrm{s}$).

$\alpha \pm 2°$ from the coil characteristics [47] and from assuming a large magnetic field deviation of 100 mG.

We have verified experimentally the influence of α on the band structure with two methods: (i) via parametric heating and (ii) via the Gutzwiller-mean field approximation. (i) The band gap between the first and seventh band in dependence of α is measured via parametric heating. We chose this transition due to its strong resonances at a lattice depth of $2.9\,\mathrm{E_{rec}}$. The measured resonances (green triangles) resolve the dependency on α as depicted in figure 4.5 (b). However, in vicinity of $\alpha = 90°$ the measured resonances are shifted upwards by approximately 200 Hz compared to the single-particle calculation (blue line). This discrepancy increases with a higher dipole trap depth ($\sim$5 %) suggesting interaction effects like mean-field shifts as possible explanations. This effect should be investigated in future studies as we also observe a dependence of the transfer efficiency on the dipole trap depth. (ii) The visibility of first-order Bragg peaks in dependence of V_{2D} and ΔV_{AB} has been compared with a Gutzwiller mean-field approximation. For further information we refer the reader to the master's thesis of M. Neundorf [119].

Rotation speed

In terms of maximum transfer efficiency it is desirable to perform the rotation of the quantization field as fast as possible. However, the rotation frequency ω_{rot} has a twofold limit: (1) the inductance of the used coils and (2) the preservation of a spin-polarized BEC.

(1) The switching time of the coils can be estimated by assuming an RL-circuit $\tau = R/L = 110\,\mu\mathrm{H}/0.5\,\Omega = 220\,\mu\mathrm{s}$. This time is close to the realized switching time

at the experiment. However note that the bipolar power supplies contain internal capacitors, which effectively form an RLC-circuit. On the one hand this can further reduce the switching time. On the other hand the resonance frequency of the circuit can be excited ([87]). In order to avoid overshooting of the current and thus pointing instabilities of the magnetic field $\boldsymbol{B}_Q$ we have typically operated with rotation times $> 200\,\mu s$.

(2) Despite the technical limitations the rotation frequency ω_{rot} cannot be increased arbitrarily. To ensure that the spin-polarized state adiabatically follows the rotation of the quantization axis, the Lamor precission $\Omega_L = \frac{g_F \mu_B B}{\hbar} = 2\pi\, 700\,\mathrm{kHz/G} \cdot |\boldsymbol{B}|$ should be much larger than the rotation frequency ω_{rot}. Complete rotations of $\boldsymbol{B}_Q = 2.2\,\mathrm{G}$ around 360° in $500\,\mu s$ guarantee a spin-polarized BEC, which we have verified with imaging after TOF and Stern-Gerlach separation. Faster rotation times maintaining the spin-polarization are possible ($< 500\,\mu s$) when reducing the strength of $\boldsymbol{B}_Q$ in combination with smaller rotation angles. In contrast figure 4.5 (c) illustrates an example of a very rapid rotation, where spin-flips to other m_F-components occur.

Experimental artifacts due to the rotation of $\boldsymbol{B}_Q$ remain. For example center-of-mass movements of the BEC are most likely induced by magnetic field gradients. A fast oscillation as large as the radius of the BEC is observed within the first 2 ms after the rotation.

4.3.3 Experimental sequence

The initial state of the system significantly influences the transfer efficiency and condensate fraction of the superfluids in higher bands. In general our measurements suggest that it is especially sensitive to quantities like atom number, temperature or interaction. In the following we give a short description of the experimental sequence and focus especially on two important preparation steps, which are the generation of the BEC in the dipole trap and the subsequent lattice ramp.

We start the experimental procedure by preparing a spin-polarized ^{87}Rb-BEC in the state $|\mathrm{F}=2, \mathrm{m_F}=-2\rangle$ in the optical dipole trap with trapping frequencies of $\omega_{x,y,z} \approx 2\pi \times (19, 45, 19)\,\mathrm{Hz}$ and atom numbers of $\sim 1.3 \times 10^6$. Subsequently the first band of the optical honeycomb lattice is loaded via an exponential intensity ramp of 100 ms. After a short waiting time of typically 2 ms the energy offset between the two sublattices is tuned via rapid rotation of the quantization axis in 0.5 ms. To observe the emergence of coherence in higher bands we let the system evolve. However, for measuring the transfer efficiency we simply wait for 0.5 ms and probe the state via band mapping (see section 3.3.2).

Dipole trap depth

The final dipole depth after evaporative cooling determines the temperature and atom number of the BEC. For lower depths with weaker harmonic confinement the temperature and atom number decrease at the expense of a lower detection signal but longer coherence times in higher bands. Thus, experimentally a compromise is chosen and the trap is adjusted only very slightly above the threshold imposed by gravity ($\Delta \sim 5\,\mathrm{mW}$). This tuning knob allows for adjusting the atom number between 8×10^4 to 4×10^5 atoms but changes at the same time coupled quantities like temperature. Measuring directly the temperature of a BEC is complicated as there is no discernible thermal fraction rendering impossible a bimodal fit with a Thomas-Fermi profile and Gaussian thermal background. Yet, the temperature can be estimated from the measured trapping frequencies. In the literature (see e.g. Pitaevskii, Stringari [120]) the critical temperature for an ideal Bose gas in a harmonic trap is given as

$$k_B T_c^0 = \hbar\omega_{ho}\left(\frac{N}{\zeta(3)}\right)^{1/3} = 0.94\hbar\omega_{ho}N^{1/3} \tag{4.3}$$

with $\omega_{ho} = (\omega_x\omega_y\omega_z)^{1/3}$. Without a discernible thermal fraction, the actual temperature is far below T_c. Assuming a remaining thermal fraction of 0.03, the temperature will be $T < 0.3\,T_c^0$, which yields temperature values of $T_c = 76\,\mathrm{nK}$ and $T = 23\,\mathrm{nK}$ for trapping frequencies of $\omega_{x,y,z} = 2\pi \times (19, 45, 19)\,\mathrm{Hz}$ and for 3×10^5 atoms. The radius of the BEC yields $r_{TFx,y,z} = (19, 8, 19)\mu\mathrm{m}$ using the Thomas-Fermi approximation and the chemical potential $\mu = 450\,\mathrm{Hz}$.

Lattice ramp

Often taken for granted but not at all trivial is the circumstance that the loading of the lattice should occur adiabatically. It has been controversially debated in the literature both theoretically also with a focus on 3D lattices including the Mott transition [121–125] and experimentally [100, 126–128]. To verify experimentally the absence of heating caused by the lattice ramp is a tedious work. In order to avoid excitations and interband transitions a slow ramp time with respect to the band gap should be chosen. This in practice means that the ramp speed can increase with increasing lattice depth, which is often realized experimentally with an exponential ramp. The absence of interband transitions can be verified via band mapping. A different aspect is adiabacity with respect to the many-body state. It is violated especially for deep optical lattices where the tunneling time $\hbar/J$ for one atom is usually larger than the complete lattice ramp. Here, different more complex ramp shapes improve the adiabacity of ramps in the 3D-lattice [124]. A further point to mention is the increasing harmonic confinement of the Gaussian lattice beams in deep lattices (see section 3.2.3). As F. Gerbier [122] points out it can increase the overall temperature, thus lead to heating, analogous to compression of harmonic traps.

At our experiment we have replaced the s-shaped lattice ramp. In deep lattices long hold times at the upper plateau of the s-ramp lead to significant heating for the deep hexagonal lattice ($V_{2D} > 8\,\mathrm{E_{rec}}$) rendering impossible the emergence of coherence for the second band. The chosen exponential ramp of 100 ms duration

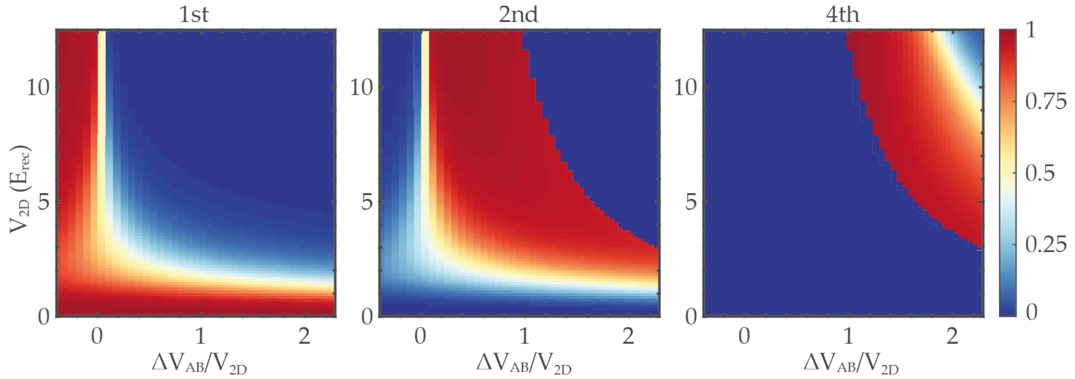

FIGURE 4.6: Overlap of the initial and final state after a rotation of the quantization axis. The overlap with the first, second and fourth Bloch band as a function of the normalized AB-Offset $\Delta V_{AB}/V_{2D}$ and the lattice depth V_{2D} is plotted. The overlap with the third band is zero and therefore not shown.

circumvents this problem. Note that a shorter duration of the exponential ramp times did excite transitions to higher bands.

4.3.4 Transfer efficiency with respect to AB-offset and lattice depth

Knowing the transfer efficiency of the used method is central for its characterization as this influences the lifetime of the prepared state. The transfer method of choice, the rotation of the quantization axis, is especially well suited to explore the transfer efficiency in a large parameter space. In the following the measurement of the transfer to higher bands is compared to the overlap of Bloch states and the transfer probability in the Landau-Zener model.

A theoretical upper limit for the transfer is given by the overlap of the initial and the final Bloch states defined as

$$\int \psi_f^n(\boldsymbol{r})\psi_i^1(\boldsymbol{r})d^3r. \tag{4.4}$$

The initial state for the first band is defined at $\boldsymbol{k} = \Gamma$ by V_{2D} and $\alpha = 0° \mathrel{\widehat{=}} \Delta V_{AB}/V_{2D} \approx -2.1$. The spatial overlap with the final state also at $\boldsymbol{k} = \Gamma$ is depicted in in figure 4.6 for the first, second and fourth band in dependence of V_{2D} and $\Delta V_{AB}/V_{2D}$. When a certain threshold of V_{2D} and the band crossings to the the second or fourth band are crossed, the overlap yields 100 % in a large parameter region. Thus, the transfer efficiency to higher bands should be high regarding only the spatial overlap of the Bloch states. A transfer to the third band is not expected as the overlap is zero.

In order to include the limited rotation speed of the quantization axis the transfer can be compared to the Landau-Zener model. We assume a diabatic transfer to the second using eq. (4.1). Here the transition probability depends on the minimal band gap at the band crossing from the Γ-point of the first band to the Γ-point of the second band and the rate of change of the bandgap between the initial and final state. First, figure 4.7 (a) shows the transition probability in dependence of V_{2D} and the

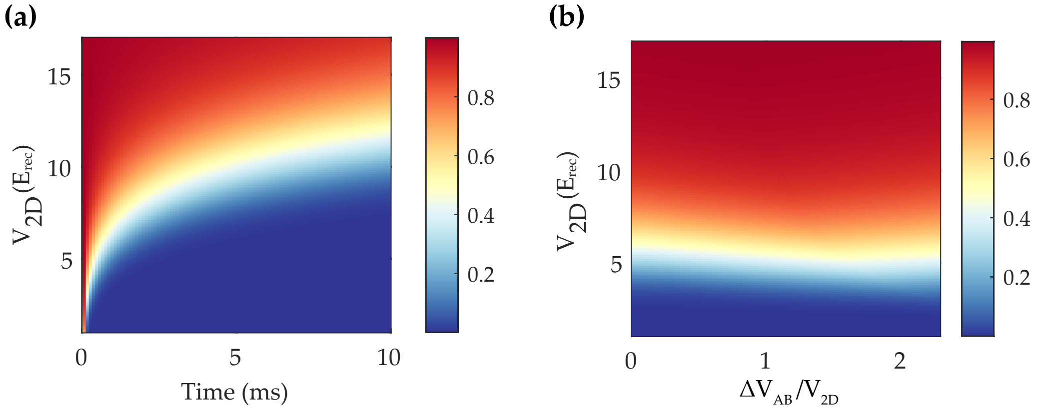

FIGURE 4.7: Calculated Landau-Zener transfer to the second Bloch band in the hexagonal lattice. (a) Diabatic transfer for varying rotation times and lattice depths V_{2D} at fixed $\Delta V_{AB}/V_{2D} = 0.63$ corresponding to $\alpha = 106°$. (b) Diabatic transfer as a function of lattice depth V_{2D} and energy offset ΔV_{AB} for a fixed rotation time of 0.5 ms. Higher band crossings are not considered here.

rotation time τ_{rot} for fixed $\Delta V_{AB}/V_{2D} = 0.63$ ($\alpha = 106°$). For shallow lattice depths significant transfer can only be reached for very fast rotations of $\sim 200\,\mu$s. Thus, we can expect that with the experimentally implemented $\tau_{rot} = 500\,\mu$s significant transfer occurs above $V_{2D} > 5\,E_{rec}$. Second, figure 4.7 (b) shows the transfer probability for the implemented τ_{rot} in dependence of V_{2D} and $\Delta V_{AB}/V_{2D}$. In this case the dependence on $\Delta V_{AB}/V_{2D}$ is negligible as the dominant factor only is the band gap between the first and second band being small above $V_{2D} > 5\,E_{rec}$ at the avoided crossing $\Delta V_{AB}/V_{2D} = 0$.

For comparison the transfer efficiency is measured by the following sequence in section 4.3.3. The parameters have been scanned from $\Delta V_{2D} \approx\sim 1\,E_{rec}$ to $\sim 15\,E_{rec}$ and from $\Delta V_{AB} \approx -0.5$ to 2.2 corresponding to angles α between 80° to 180°. After band mapping of 2 ms followed by 36 ms TOF, resonant absorption images were taken. For the respective Brillouin zones we placed masks onto the band mapping images as illustrated in figure 4.8. Despite the short holding time of 0.5 ms after the rotation atoms already accumulate in a region around K-points of the second band or around Γ-points of the fourth band. They overlap with either the third or second Brillouin zone. Therefore the masks on the absorption images are extended compared to the definition of Brillouin zones. We then evaluate the relative atom number and obtain transfer efficiencies for the first four Bloch bands as depicted in figure 4.8. Evidently the transfer to the second band is limited by the band crossings to the band itself and to the fourth band. In agreement with the Landau-Zener calculation transfer occurs for $V_{2D} \gtrapprox 5\,E_{rec}$. A transfer efficiency of about 65% is reached. Similar observations hold for the fourth band, which is populated via two subsequent Landau-Zener transfers. The maxium achieved transfer rate yields $\approx 35\,\%$. The transfer to the third band is expected to be zero. On the one hand the overlap is zero. On the other hand also an intuitive explanation exists. The Γ-point of the third band is degenerate with the fourth band, thus the Landau-Zener transition will

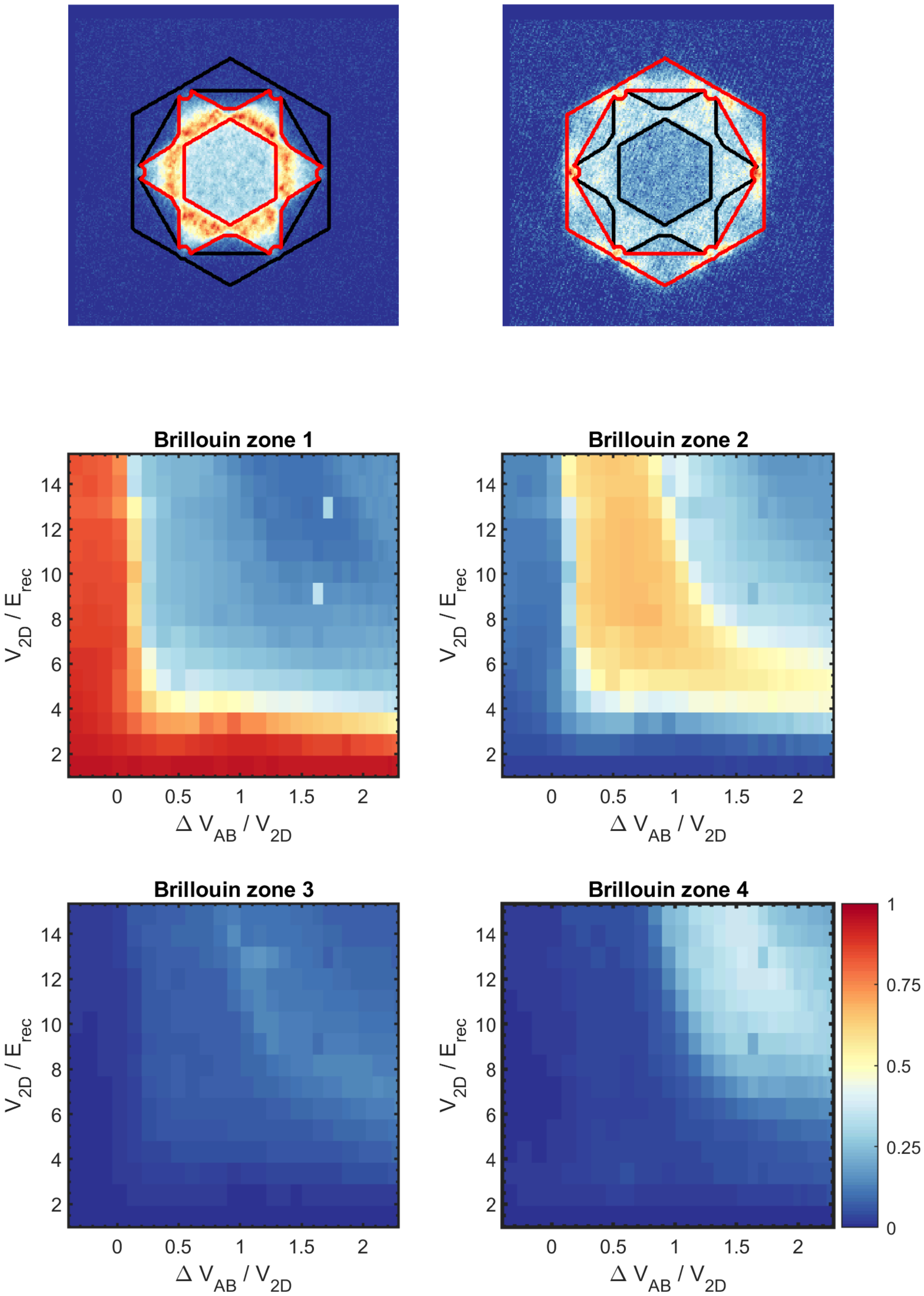

FIGURE 4.8: Measured transfer efficiency. *Upper row:* Masks on exemplary band mapping images for counting the relative atom number in the different Brillouin zones. The red Brillouin zones for the second and fourth band (red) have been corrected for experimental artifacts. A Also visible are the first and third Brillouin zone. *Middle and lower row:* Relative transfer efficiency to the first four bands obtained from the Brillouin zone masks. About 65 % of the atoms are transferred to the second band while about 35 % are transferred to the fourth band. The third band is less populated.

directly occur to the fourth band. Yet, we still observe a relative small occupation of about $\approx 15\,\%$.

Both the Landau-Zener transfer and the overlap calculations already give a good impression for the experimental transfer efficiency although for quantitative predictions precise evolution for the complete Hamiltonian should be considered. Especially for deeper lattices the spread of the populated quasimomenta becomes significant and the interaction increases. Further, we have observed a significant effect on the transfer efficiency from the dipole trap depth (atom number, temperature). This has been similarly resolved by amplitude modulation in section 4.3.2.

4.3.5 Coherent transfer

The rotation of the quantization axis permits Landau-Zener tunneling of a coherent matter wave to the second Bloch band. In order to demonstrate this we prepare a superfluid state in the first Bloch band at shallow lattice depths of $V_{2D} = 1.6\,\mathrm{E_{rec}}$ and $2.95\,\mathrm{E_{rec}}$, here in $|1,-1\rangle$. The transfer occurs via a rapid rotation of 250 µs duration to $\alpha = 180°$. As mainly quasimomenta $\boldsymbol{q} = 0$ are populated, the transfer should occur from $\Gamma \to \Gamma$ revealing a two-level superposition state of the form

$$|\psi(t)\rangle = c_1|1\rangle + c_2 e^{-i\Delta E t/\hbar}|2\rangle \tag{4.5}$$

where a different phase between the two Bloch bands $|1\rangle$ and $|2\rangle$ is acquired. The experimental signature can be distinguished clearly from the pure ground state in momentum space via TOF imaging. Oscillations appear in the Bragg peaks due to the phase evolution. They are clearly visible when separating the first order Bragg peaks into two groups as depicted in figure 4.9 (b) by the red and blue circular masks. With the same frequency oscillations are also present on the zero-order Bragg peak shifted by $\pi/2$. The oscillations have been fitted with an exponentially damped sine yielding $7033(18)$ Hz for $V_{2D} = 1.6\,\mathrm{E_{rec}}$ and $8551(30)$ Hz for $V_{2D} = 2.9\,\mathrm{E_{rec}}$. These frequencies deviate from the expected calculated single-particle band difference being 6770 Hz and 8750 Hz. A small positive deviation from the experimentally measured frequency can be expected due to interaction shifts but the different signs of the deviations for the respective lattice depths are dubious. A possible explanation is that at the time of the measurement etalon effect yielding lattice calibrations imprecise over time. Nevertheless, this demonstrates the preparation of a coherent superposition state which however is short-lived. The damping of the oscillations occurs mainly due to band relaxations to the ground band.

Note that such a superposition state has also been observed using a microwave sweep from $|2,-2\rangle$ to $|1,-1\rangle$ for the transfer to the first and second band [44]. Here, also further information can be found regarding interaction effects with spin-mixtures.

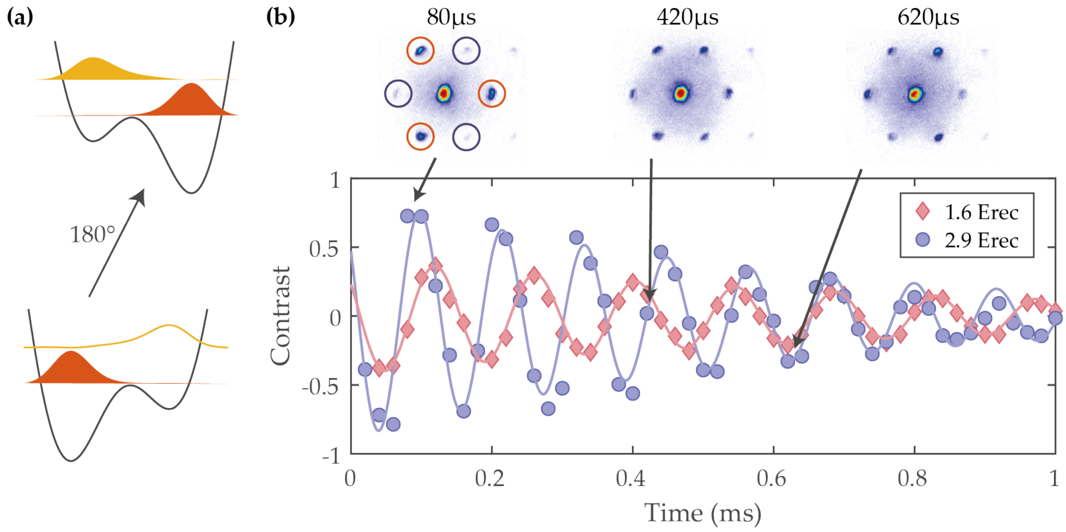

FIGURE 4.9: Coherent transfer to the second Bloch band. (a) Potential cuts of the well-structure in the honeycomb lattice with the Bloch states in the first (red) and second (yellow) Bloch band before and after the rotation of the quantization axis by 180°. The density distribution for the respective bands is either localized mostly only on the A- or B-sites. (b) Superposition at the Γ-points of the first and second Bloch band. The triangular contrast (red and blue circular masks on the TOF image), which oscillates in the first order Bragg peaks in the TOF-images is evaluated. The frequency of the oscillations is fitted with an exponentially damped sine yielding 7033(18) Hz for $V_{2D} = 1.6\,\mathrm{E_{rec}}$ and 8551(30) Hz for $V_{2D} = 2.9\,\mathrm{E_{rec}}$.

4.4 Conclusion and outlook

In this chapter, different transfer methods to higher Bloch bands are compared. Implemented transfer methods include amplitude modulation, RF-transitions and the rotation of the quantization axis. The latter can be pictured as a Landau-Zener transition and is the method of choice to explore a large parameter space. The transfer efficiency to higher Bloch bands in dependence of the lattice depth and the AB-energy offset is measured. It is constant over larger region yielding $\sim 65\,\%$ for the second band and $\sim 35\,\%$ for the fourth band. Thus, after the transfer a significant fraction remains in the first band, which can influence the prepared states in the higher bands. As an example, we report on a coherent transfer to the second Bloch band, which results into a superposition state at the Γ-points between the first and second Bloch band.

The transfer method, the rotation of the quantization axis, is limited by the rotation speed and induces movements onto the BEC. Therefore, in the following we outline two more possible paths to higher bands.

Lattice loading using a pulsed sequence

A new shortcut method to load bosonic species into an optical lattice has been proposed and realized in 2018 by Zhou et al. [104]. The typically long time $\sim$100 ms of ramping up the lattice intensity is replaced by a specially designed pulsed sequence with only a few microseconds of duration. This sequence cannot only be used to load BECs into the first band but also into any other higher lying bands. Preparations at non-zero quasimomenta are possible. Already other experiments have implemented successfully on this technique in order to load into higher bands of optical lattices [129, 130]. A further advantage of this method is the remarkably reduced switch-on time of the optical lattices. Heating by sponteous emission for very near resonant lattices is thus negligible during the lattice ramp. Thus, it should be possible to realize even higher lattice depths, which are not possible to address with our present laser setup. This method also provides further potential for sophisticated probing methods, e.g. a Ramsey inferometer for atoms in optical lattices [131]. However, to the author's knowledge an investigation of the lifetime in higher bands has not been published with this method. Still, it is possible to implement this loading method with the newly implemented lattice control presented in this thesis and investigate its preparation fidelity.

Raman transitions

Raman transitions do not only change the energy but also impart a momentum. For a transfer to the second band this means that direct transfers to specific momenta are possible, e.g.from $\Gamma \to K$ in the honeycomb lattice or from $\Gamma \to X$ in the square lattice. In a deep cubic 3D lattice experiment with ^{87}Rb this was done by Müller et al. [30]. The two lowest Bloch bands (vibrational levels) were coupled coherently with a stimulated two-photon Raman process. However, in their experiments either one or two of the lattice directions were frozen out thus creating a strongly asymmetric lattice in order to suppress tunneling in these directions. Also, the coherence in the higher Bloch band has been small and very limited in lifetime $<$1 ms.

Nevertheless, this method is promising since it enables the population of higher bands in the 2D-honeycomb lattice at chosen quasimomenta. In addition, it allows for probing the system via Bragg spectroscopy. Here, preparatory work by designing a new hybrid trap allowing for more optical access and conceptional considerations on the implementation on Bragg spectroscopy has been done by our master's student Phillip Groß [132].

Chapter 5

Condensation in the second and fourth Bloch band

The main motivation to investigate condensation dynamics in higher Bloch bands has been the prospect to realize unconventional superfluids with exotic phases. For this, most effort during this PhD project has been dedicated to maximizing the lifetime of the prepared excited states. This includes e.g. numerous technical optimizations (see section 3.4) but also the analysis of the condensation process in the second and fourth Bloch band in the 2D-honeycomb lattice. In this chapter, we first focus on the experimentally optimal parameters for condensation and prove that condensation is indeed realized experimentally. Further, the following four stages of the condensation dynamics can be distinguished: (1) the transfer to the higher band, (2) the emergence of coherence, (3) its subsequent decay and (4) the relaxation to the ground state. We analyze theses stages in the lattice plane, their timescales as well as differences between the second and the fourth Bloch band. The parameter space is explored regarding the control of the band structure. Additionally, we compare our findings directly with experiments in the bipartite square lattice conducted by the group of A. Hemmerich [36]. Finally, we summarize the key ingredients for condensation.

The experimental data presented in this chapter has been measured with main contributions by the author in collaboration with A. Ilin, J. Seeger and P. Groß. The data evaluation presented in this chapter has been conducted by the author. A theoretical description of the condensation process continues in collaboration with G. Koutentakis, S. Mistakidis and P. Schmelcher.

5.1 Condensation dynamics

In this section we discuss the characteristic features of the condensation dynamics in the second and fourth Bloch band. Therefore, we explored the parameter space controlling the band structure by varying lattice depth V_{2D} and energy offset ΔV_{AB}, which depends on the angle α of the quantization axis. We have identified an island of stability providing a maximum lifetime in the excited bands. The optimal parameters yield

$$\begin{array}{llll} 2^{\mathrm{nd}}\text{ band} & V_{2D} \approx 7.5\,\mathrm{E}_{\mathrm{rec}} & \text{and} & \Delta V_{\mathrm{AB}} \approx 5\,\mathrm{E}_{\mathrm{rec}},\ \alpha = 106^\circ \\ 4^{\mathrm{th}}\text{ band} & V_{2D} \approx 15\,\mathrm{E}_{\mathrm{rec}} & \text{and} & \Delta V_{\mathrm{AB}} \approx 12\,\mathrm{E}_{\mathrm{rec}},\ \alpha = 122^\circ. \end{array}$$

For these two parameter sets we present measurements and show that we realize superfluids in higher bands.

5.1.1 Evidence for condensation

The emergence of phase coherence is observed shortly after the transfer to the higher Bloch band. For simplicity we first describe the process in the fourth band and then in the second band.

Condensation in the fourth band

The experimental sequence begins by loading the BEC into the first band of the deep hexagonal lattice. At $V_{2\mathrm{D}} = 15\,\mathrm{E}_{\mathrm{rec}}$ the ground band has a small bandwidth of $\sim 0.1\,\mathrm{Hz}$. For this initial state no spatial phase coherence is observed in the lattice. Subsequently the transfer to the higher Bloch band is performed by a rapid rotation (0.5 ms) of the quantization axis tuning the AB-energy offset ΔV_{AB}. This time-dependent control over the band structure allows us to realize Landau-Zener transitions. The transfer to the fourth Bloch band requires two subsequent diabatic passages. Finally, the transferred population thermalizes in the higher band whose properties can be tuned by the potential offset ΔV_{AB} and lattice depth $V_{2\mathrm{D}}$. An illustration of the band structure during the transfer is depicted in figure 5.1 (a).

The population transferred to the fourth band suddenly experiences a larger bandwidth ($\sim 250\,\mathrm{Hz}$). As the bandwidth is proportional to the tunneling, this results into the emergence of spatial coherence in the system. Due to the band structure of the fourth band we expect the macroscopic occupation of the minima at the Γ-point. The population reaches a maximum after 4 ms of holding time for the optimal parameters. At these parameters we analyze exemplary TOF and band mapping images (figure 5.1 (b), (c)) to prove the existence of a superfluid in the fourth bands and to quantify the superfluid fraction.

In the TOF image in figure 5.1 (b) the optical density yields 1.2. Bragg peaks are visible up to the second order and indicate spatial coherence in the system [19, 133]. The coherence can be quantified by evaluating the visibility (section 3.3 and 5.1.2). We obtain peak values of ~ 0.55. However, a direct connection to the condensate fraction, which would quantify the system, is not available. In principle this can be done with ab initio quantum Monte Carlo simulations where a direct comparison to TOF images determines the temperature [100] or by employing single-atom detection in momentum-space [101]. Yet, a more practicable implementation is the recently published 'quantum magnifier' using matter-wave magnification [110].

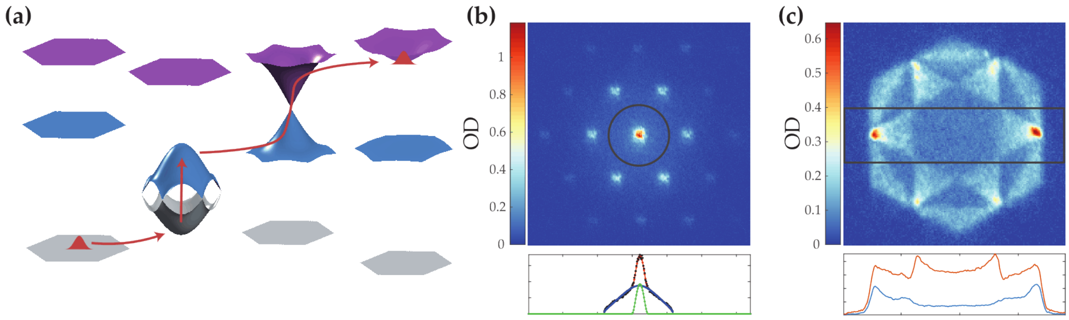

FIGURE 5.1: Evidence for condensation in the fourth band. (a) Transfer to the fourth band in momentum space. Two subsequent Landau-Zener transitions are driven to reach the fourth Bloch band (violet). In contrast to the first band crossing, the band gap between the second and fourth Bloch band is closed at the Γ-point. The minimum of the fourth band is located as for the first band at the Γ-point. Note, as the overlap with the third band is zero, it is omitted in the illustration. (b) TOF image with a superfluid in the fourth band and a bimodal 2D-fit of the zero-order peak (grey circular mask). The parabola fit of the condensate (green) and the Gaussian fit to the thermal fraction (blue) fit nicely yielding a condensate fraction of 12(3) %. (c) Band mapping image with the profile of the complete image (red) and the rectangular grey box (blue).

Bearing the limitations of TOF in mind [99] we can still estimate the condensate fraction by employing bimodal 2D-fits to the TOF images. This works especially well for the fourth band. First the realized condensate fraction is medium high yielding a clear bimodal distribution. Second the zero-order peak has a certain width, which can be fitted reliably. For the fit shown below the TOF image in figure 5.1 (b) we obtain an overall condensate fraction of 12(3) %, which corresponds to $\sim$ 35 % of the population in the fourth band taking the transfer rate into account. This fit to determine the condensate fraction can be also extended to different holding times. The condensate fraction resembles that of the visibility. This will be shown in the thesis of A. Ilin.

Condensation in the second band

A similar emergence of phase coherence is observed in the second Bloch band, yet the minima of the second band are located at the K- and K′ points. This is fundamentally different from the first and fourth band, where the minima are located at the Γ-point. Thus, assuming initially a many-body wave packet occupying predominantly the Γ point, the maximum of the second band, an intriguing condensation process for the formation of phase coherence in the minima in the second band takes place. The transfer and condensation process of such a wave packet is illustrated in figure 5.2 (a).

The population at the K- and K′-points in the second band reaches a maximum after 7 ms holding time after the transfer. This is clearly visible in the TOF image in figure 5.2 (b). Bragg peaks are visible up to the second order and the visibility reaches peak values of $\sim$ 0.4. An estimation of the condensate fraction by using bimodal fits is not as conclusive as presented for the fourth band. They are limited

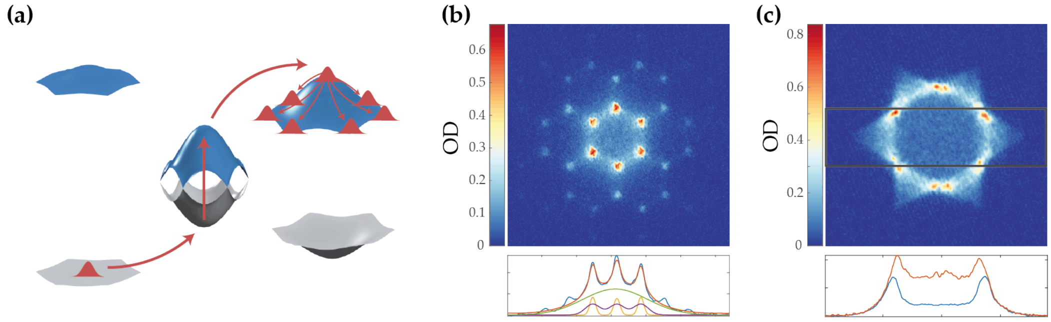

FIGURE 5.2: Evidence for condensation in the second band. (a) Transfer to the second band in momentum space. The condensate is prepared initially at the Γ-point in the first Bloch band (grey). A Landau-Zener transition to the second band is driven via a rapid tuning of the energy-offset ΔV_{AB} controlling the bandgap between first and second Bloch band (blue). At vanishing ΔV_{AB} the bandgap at the K-points is closed whereas it remains finite at the Γ-points. In the second Bloch band the red wave packets illustrate the condensation process in the band minima at the K and K′-points. (b) TOF image with a superfluid in the second band and the corresponding profile (blue) with bimodal 2D-Gaussian fits (red). The condensate (yellow) and thermal distributions (violet) at the the K- and K′-points and a global incoherent background attributed to the remaining atoms in the first band were fitted with Gaussians. (c) Band mapping image with the profile of the complete image (red) and of the rectangular grey box (blue).

by the small width of the Bragg-peaks and the small distance between the K- and K′-points. Furthermore, many fit parameters are required. The number of available parameters is reduced by subtracting the incoherent background and distinguishing only between K and K′-points. Yet, the fits prove less reliable than desired but still allow us to estimate the condensate fraction in figure 5.2 (b) to $\sim 15\,\%$ corresponding to about 25 % of the population in the second band. Also the detection via band mapping reveals a population of the K- and K′-points as depicted in figure 5.2 (c). From this image the condensate fraction is estimated to $\sim 15\,\%$ by placing masks around the K-region as described in section 5.2.3.

In summary, these results show that a significant condensate fraction is observed at the optimal parameters either at nonzero quasimomenta in the second band or at zero-quasimomentum in the fourth band. Note that even though the transferred fraction to the fourth band is about 20 % smaller than to the second band, the fitted condensate fraction, the optical density and the visibility are larger indicating a higher degree of coherence. A possible explanation for this is the difference in the condensation process due to the different geometry of the excited bands. This subject is further elaborated in the following sections.

5.1.2 The four stages of the condensation dynamics

In the following the condensation dynamics is analyzed in dependence of the holding time after the transfer to the lattice. In general the behavior and time scales of the condensation dynamics are similar in both bands. They exhibit four characteristic steps. Before the discussion of the dynamics first the experimental sequence and analysis of the TOF and band mapping images are presented.

The experimental sequence has already been described in detail in section 4.3.3. We recall that we initially prepare a spin-polarized ^{87}Rb-BEC in $|2,-2\rangle$ in a dipole trap with a harmonic confinement of $\omega_{x,y,z} \approx 2\pi \times (19, 45, 19)$ Hz at a temperature $T \approx 23$ nK and atom numbers of about 1.7×10^5 atoms. Subsequently the 2D-honeycomb lattice is exponentially ramped up to a lattice depth V_{2D} in 100 ms. After a short holding time of 2 ms in the lattice the quantization axis is rotated in 0.5 ms to a final angle α. In the following we present measurements, which were performed with optimal parameters for the maximum lifetime (see table 5.1). Interestingly the engineered band structure for the respective higher band is very similar in terms of bandwidth and band gap to the lower lying band.

transfer to band	probing	V_{2D} (E_{rec})	α (°)	ΔV_{AB} (E_{rec})	band gap Δ (E_{rec})	bandwidth Λ (E_{rec})	atom # $\times 10^3$
2	TOF	7.4	106	4.7	3.63	0.096	176(18)
	BM						195(17)
4	TOF	14.7	122	17.8	4.03	0.074	130(23)
	BM	14.9		18.1	4.17	0.071	212(30)

TABLE 5.1: Experimental parameters of the presented measurements in state $|2,-2\rangle$. The band gap given for the fourth band denotes the band gap between the fourth band and second band.

To analyze the condensation dynamics we took typically four absorption images per time step after TOF and band mapping, which give access to the phase coherence and the band population. As a measure for coherence we evaluated the visibility in the TOF images. The visibility is defined by circular masks placed at and in between the K-points for the second band and at the Γ-points for the fourth band (cf. inset of figure 5.3 (c)). The obtained visibility depends on the circle size. For the here presented data we choose a radius of 10 pixels. Smaller circle radii increase the visibility but movements of the Bragg peaks are more pronounced as analyzed in appendix C.2. We obtain the band population by counting the atom number in band mapping images in the respective masks for each Brillouin zone. The masks used in the inset of figure 5.3 (b) are slightly extended from the strict definition in order to account for experimentally induced movements and deformations in the quasimomentum during band mapping.

Figure 5.3 depicts the direct comparison of the separate measurements for the second and the fourth Bloch band. We categorize the description into four stages.

Stage 1: transfer to the higher Bloch band

Initially, the atomic ensembles are transferred with a transfer efficiency of $\sim 55\%$ to the 2nd band and with $\sim 30\%$ to the 4th band. The TOF images show an atomic distribution with a broad distribution in momentum space.

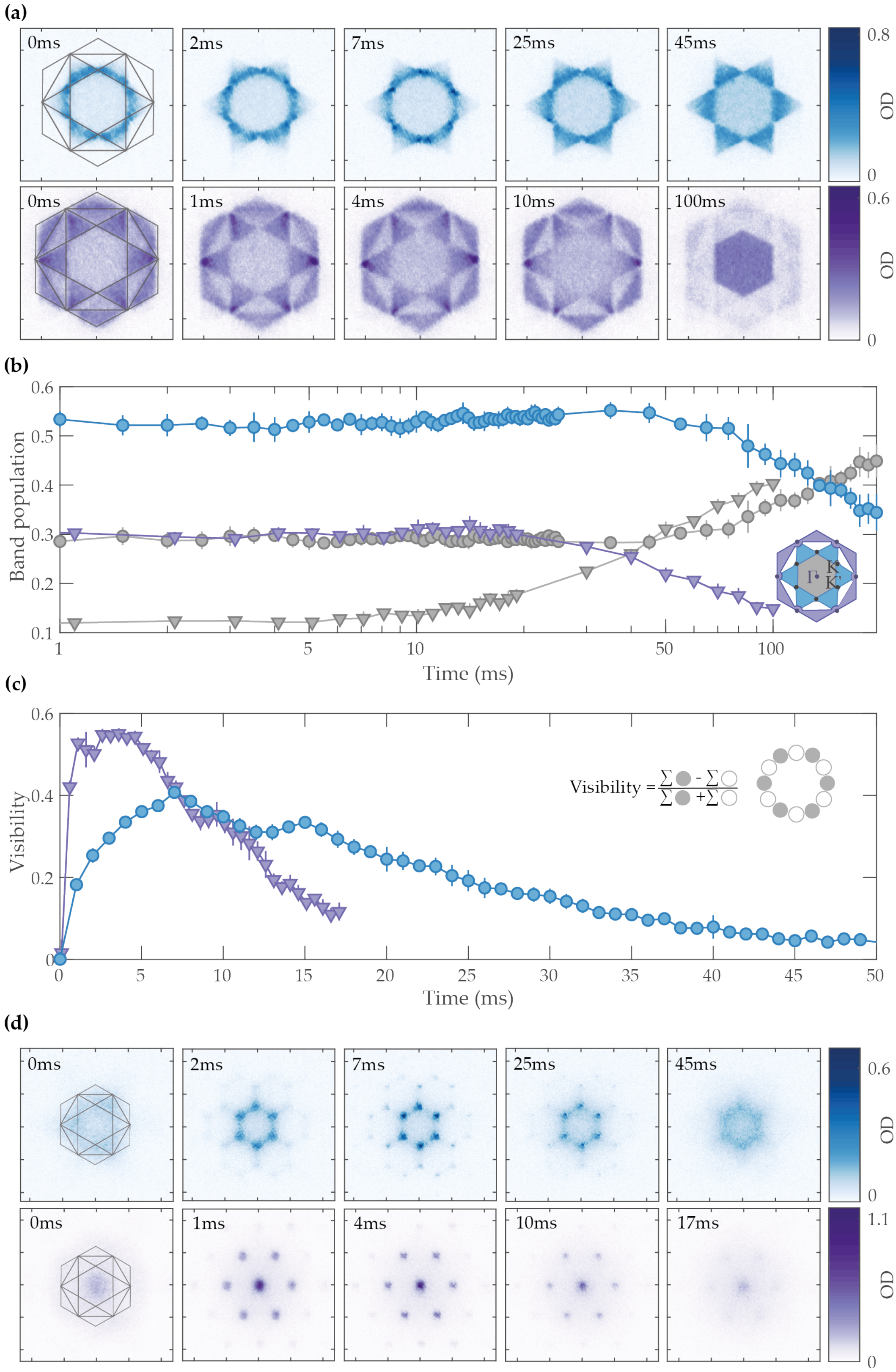

FIGURE 5.3: Visibility and band population for the second and fourth Bloch band at optimal parameters. (a) Selection of band mapping images for the second band (blue) and fourth band (violet) scaled to the optical density. (b) Relative band population for the two series of measurements. The inset shows the masks for the respective color coded bands (circles - measurement 2nd band, triangles - measurement 4th band, grey - population in the 1st band for each series). (c) Visibility for the second and fourth band with its definition in the inset. (d) Selection of TOF images for the second and fourth band scaled to the optical density.

Especially in the second band we observe oscillating features after TOF, which are reminiscent of the coherent superposition state at the Γ-points in the first and second band (see section 4.3.5). The oscillating features are strongly blurred due to the incoherence and show a strong damping. They occur within the first $\approx 0.5\,\mathrm{ms}$ and vanish as soon as the population of the K- and K′-points grows.

Stage 2: emergence of coherence

Driven by collisions atoms begin to redistribute rapidly within their respective band. They accumulate at the respective band minima (K-points - 2nd band, Γ-points - 4th band). In the TOF images Bragg peaks appear already after $\sim 1\,\mathrm{ms}$. They indicate the level of coherence growing with increasing holding time. Its maximum is reached at 7 ms for the 2nd band and at 4 ms for the 4th band. At this point second-order Bragg peaks are clearly visible.

Stage 3: decay of coherence

The atomic ensemble redistributes homogeneously within its band. In contrast to the emergence of coherence (step two), the atomic distribution is more homogeneous. For comparison, see for example BM images at 2 ms where quasimomenta $\boldsymbol{q}$ towards the K and M-points are populated stronger than in the TOF image at 45 ms (figure 5.3 (a)). This suggests that the temperature of the atomic ensemble has increased. In the TOF images the higher order Bragg peaks become less prominent indicating a loss of coherence. This is also captured by the visibility. Fitted with an exponential decay, the decay time yields $\tau_2 = 18(1)\,\mathrm{ms}$ for the second band and $\tau_4 = 12(6)\,\mathrm{ms}$ for the fourth band. In general, the coherence decays while the band populations stays constant.

Stage 4: decay of band population

When the coherence has disappeared, eventually a significant decay of the the band population in the excited bands begins. Thus, the time-scales of the decay of coherence and the relaxation to the first band are separated. In the second band relaxation begins after 50 ms, in the fourth band it begins after 20 ms. The decay from the fourth band occurs to the second band and continues then to the first band. The general behavior of the decay is further analyzed in section 5.2.1.

5.2 Exploring the parameter space

So far, the analysis has been concentrated on the island of stability, the condensation at the optimal parameters. For the second and fourth band phase coherence in the excited band has been maximized. Generally, this is influenced by the tunneling time to develop coherence and by the decay time of the coherence and the relaxation to lower bands. These parameters depend strongly on the band structure. In this section we first analyze the band decay. Second we give an overview of the parameter space supporting superfluids. Third we compare our measurements in the bipartite hexagonal lattice directly to the bipartite square lattice of the Hemmerich group based on a recent publication by Nuske et al. [36].

5.2.1 Band decay

In order to evaluate the band decay, we measured the relative band population after the transfer to either the second or fourth band for different lattice depths V_{2D} and angles α. The holding time after the transfer increased from 1 ms to 200 ms. The excited band population was fitted with an exponential decay $a\exp(-1/\tau_{\text{band}}t)+c$ to obtain a decay time τ_{band}. Data points at short holding times, where the population is constant over time (cf. figure 5.3) are omitted.

In the following a data set for the fourth band is presented, where an area around the optimal parameters ($V_{2D} = 14\,\mathrm{E}_{\text{rec}}$ and $\alpha = 122°$) is covered by 3x3 measurements varying the lattice depth V_{2D} and the potential offset $\Delta V_{\text{AB}} = \alpha$. The measurements cover a major part of the region between the band crossings in the fourth band and are marked in figure 5.4 (a) and (b). Figure 5.4 (a) depicts the calculated band gap from the fourth to second band Δ_{42} and figure 5.4 (b) depicts the bandwidth of the fourth band Γ_4. The decay time τ_{band4} is plotted in dependence of Δ_{42} in figure 5.4 (c). We observe the smallest decay for $\tau_{\text{band4}} = 37(2)$ ms at $\Delta_{42} = 13$ kHz. The decay increases strongly for smaller and larger Δ_{42}, which corresponds only to small changes of α. Further, figure 5.4 (d) shows the decay time as a function of Γ_4. The data suggest that a smaller Γ_4, thus lower tunneling leads to a slower decay.

This situation is expected to be similar for the second band. At the optimal parameters, we obtain a longer decay time of $\tau_{\text{band2}} = 57(2)$ ms than for the fourth band. Interestingly, the band gap to the lower band yields also $\Delta_{21} \approx 13$ kHz at the optimal parameters. The same also holds for the bandwidth. However, the currently available data set of the second band is too small to present a similar analysis as was conducted for the fourth band.

We conclude that both band gap and bandwith play a crucial role for the band decay. It would be interesting to compare these results to a theoretical model. A recently joint experimental and theoretical study has been recently published closely related results for the second band of the bipartite square lattice by Nuske et al. [36]. Here, instead of varying V_{2D} and ΔV_{AB} only ΔV_{AB} is varied, but the authors also find an optimum setting for ΔV_{AB}, where band relaxation is reduced. They find that the decay is driven by hopping to the lowest band in case of a smaller ΔV_{AB}, while for larger ΔV_{AB} the decay is driven by interaction decay. This is also plausible for the hexagonal lattice.

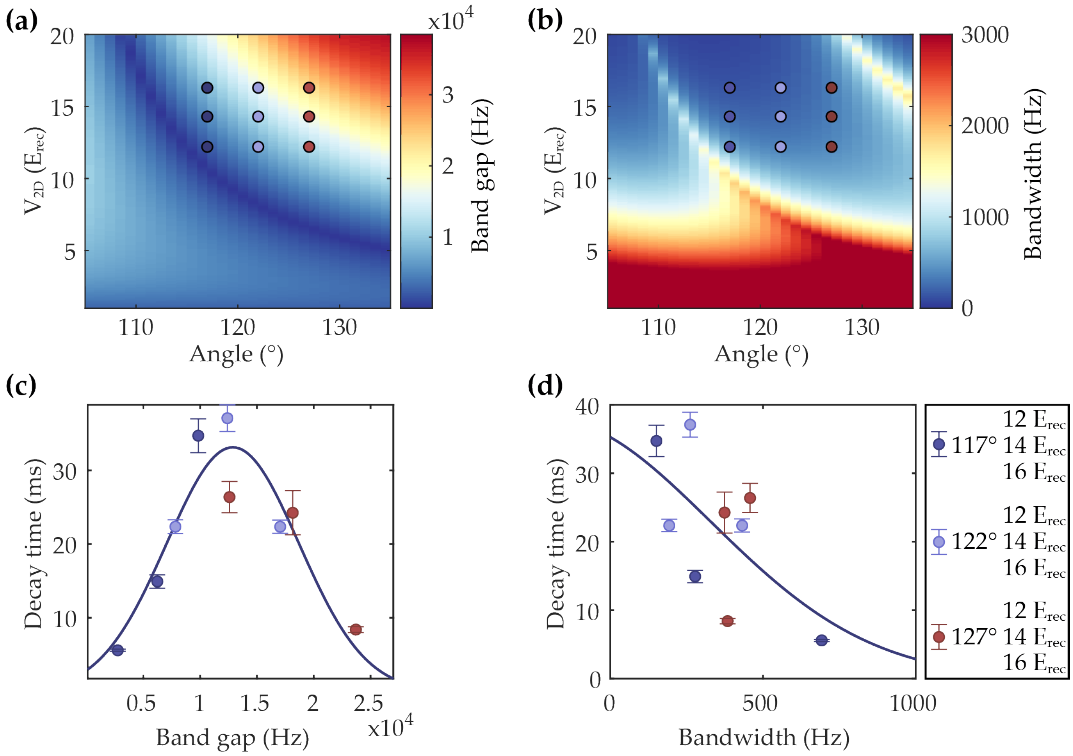

FIGURE 5.4: Band decay from the fourth band. (a) Band gap between the 4th and 2nd band as a function lattice depth V_{2D} and angle α. Colored circles mark the measured data. (b) Bandwidth of the 4th band as a function lattice depth V_{2D} and angle α. Colored circles mark the measured points. (c) Decay time versus the band gap between the 4th and 2nd band. A Gaussian fit serves as a guide to the eye. (d) Decay time versus bandwidth of the 4th band. A Gaussian fit serves as a guide to the eye.

5.2.2 Overview on the visibility

The central scope is to prepare metastable superfluid states in higher bands. Thus, the parameter space should be also explored regarding the coherence i.e. the measurable visibility.

Therefore a similar measurement as for the band decay is performed. To manipulate the band structure we use the experimentally accessible lattice depth V_{2D} and the AB-potential offset ΔV_{AB} controlled by α. In order to map the available parameter space for condensation we scan the lattice depth $V_{2D} = 4 - 12\,\mathrm{E_{rec}}$ and rotate the quantization axis in 0.5 ms to a final angle of $\alpha = 90° - 180°$. This range covers approximately a bandwidth from 1000 Hz to 100 Hz and band gap Δ of 5700 Hz to 40 000 Hz. The band crossing to the second and fourth Bloch bands are included. For completeness a full map of the band gap and the bandwidth of the first, second and fourth band is given in appendix A. After the rapid rotation we let the system evolve for 7 ms and probe it after 38 ms of TOF. The visibility is evaluated at the K-points and at the Γ-points separately. In this way the visibility is obtained for the second band and for the first and fourth band respectively. Its sum, the resulting visibility map is displayed in figure 5.5.

We distinguish three regions with higher visibility.

Region I: At and in vicinity to $\alpha = 90\,°$, which is equal to $\Delta V_{\mathrm{AB}} = 0$, the visibility reaches its highest values with 0.8. Here, the first band is populated. Even though V_{2D} is deep, the degenerate AB-sites and the higher bandwidth in the first band increase largely the tunneling, thus the coherence.

Region II: Rotating slightly further ($\alpha > 100°$) the second band is populated. An increased visibility is observed from the minimal band width of the second band (violet) up to the band crossing to the fourth band (gray line). A broad maximum is located in between the band crossings at $V_{2D} \approx 7.5\,\mathrm{E_{rec}}$ and $\alpha = 106°$ showing the optimal parameters for coherence in the second band.

Region III: The fourth band is populated beyond the band crossing to the fourth band (gray line). Like in region II the visibility is increased approximately at the band minimum up to the band crossing to the fifth band (gray dashed line). The optimal parameter for highest visibility at $V_{2D} = 14\,\mathrm{E_{rec}}$ has not been recorded in the measurement, thus the optimal parameters of the fourth band are not completely resolved.

High visibility can also occur for shorter holding times than for the 7 ms used in this measurement. This is the case for low lattice depths ($< 4\,\mathrm{E_{rec}}$), where the band relaxation is too fast to observe a signal after 7 ms of holding time. For instance, the coherent transfer described in section 4.3.5 was realized in this regime.

Furthermore, the optimal parameters for condensation in both excited bands are very similar with respect to the band structure. We depict characteristic lines of the band structure in figure 5.5: the minima of the bandwidths (violet), the band gap $\Delta =$

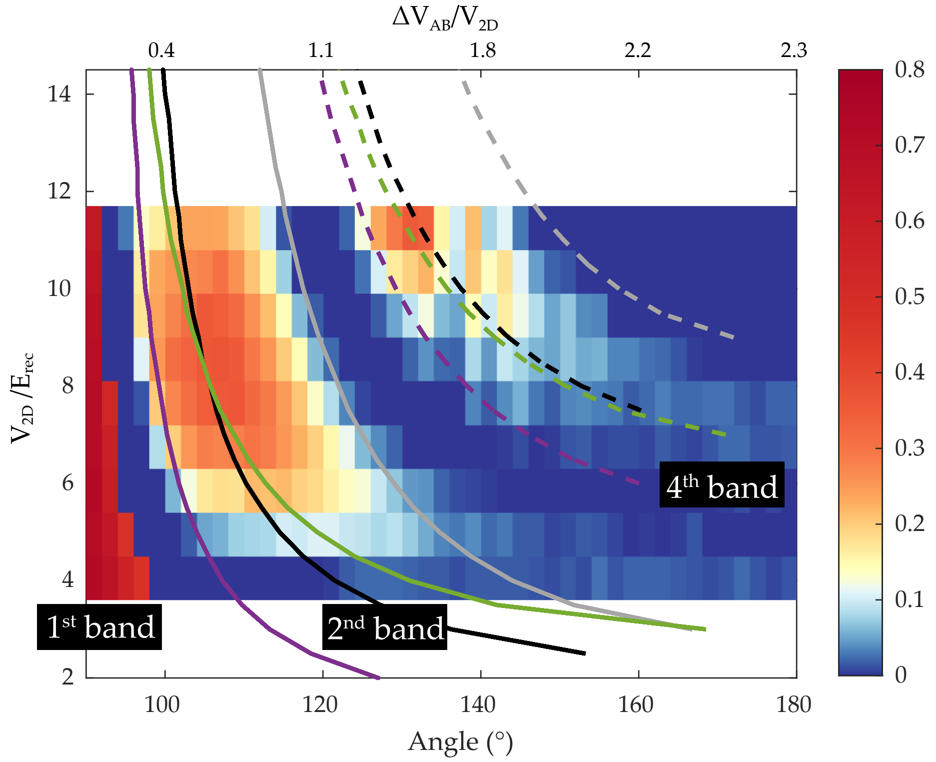

FIGURE 5.5: Exploration of the parameter space for visibility in higher bands. The figure depicts is the sum of the two visibilities defined separately at the K- and Γ-points at 7 ms holding time. Three regions with high visibility can be identified. For orientation characteristic lines for the second band (continous lines) and for the fourth band (dashed lines) are displayed: band of the bandwidth (violet), band crossing to the next highest band (grey), band gap of 13 kHz to the first (second) band (green), minimum of bandwidth over band gap (black).

13 kHz (green) to the first, respectively second band and the minimum of the ratio band width Γ over bandgap Δ (black). This allows the following conclusions: (1) the minimal bandwidth does not explain the optimal parameters for condensation; (2) The 13 kHz-band gap and the minimum of the ratio Γ/Δ agree well with the shape of the regions with enhanced visibility. Especially the good agreement of the latter is intriguing. This relation is motivated by a recently published calculation of recondensation dynamics in higher bands [134]. Here, the decay rate is proportional to $(J/\Delta)^2$. Further, systematic measurements are required to analyze this.

5.2.3 Comparison to the bipartite square lattice

In the last decade the experimental advances in preparing condensates in higher bands in a bipartite square lattice have been driven by the Hemmerich group [31–33, 35, 113]. Thus, a direct comparison of our experimental results especially with the recent publication by Nuske et al. [36] is desirable.

The authors present a joint experimental and theoretical study on the formation and decay of a coherent metastable state in the second band of the bipartite square lattice also using ^{87}Rb in $|F = 2, m_F = \pm 2\rangle$. Three different stages are identified: the condensation to the coherent metastable state, the decay to a thermalized state and the subsequent decay to the ground state. Further, the decay time to the ground state is measured at a fixed lattice depth of 7.2 E_{rec} as a function of the final AB-potential offset and compared to numerical calculations. It exists an optimal offset for slowing down the decay. For smaller potential offsets hopping decay dominates i.e. atoms in the second band tunnel to the first band. For larger potential offsets interaction decay dominates i.e. two atom in the second band collide and are transferred to the first band.

To analyze the data, the condensed, thermal and total atom number in the second band have been counted in band mapping images. We have adapted the evaluation method to our lattice and have applied it to the data presented in section 5.1.2. As depicted in figure 5.6 (a) we place Brillouin zone masks onto the image to count the atom numbers in the respective bands. We place eight candy-shaped masks and ring segments around the K-points. We assume atoms in the ring segments to be thermal and calculate their density per pixel. With the thermal density we can then subtract the thermal fraction from the condensed fraction in the K-region.

The results, the relative atom number as a function of holding time, are displayed in figure 5.6 (b) and show clearly similar behavior when evaluated with the visibility. In addition, the condensed fraction normalized to the second band yields ~ 0.17, which is in agreement to the fits in section 5.1.1. Note that at the peak of the coherence at 7 ms 30 % of all atoms are in the K-region, which corresponds to 50 % of the atoms in the second band.

However, as depicted in figure 5.6 (c), our condensate fraction is rather low compared to data from [36]. The condensate fraction in the square lattice yields $\sim$ 25 % for the hotter measurement at $\sim$ 110 nK and reaches even $\sim$ 50 % for $\sim$ 50 nK. Furthermore, when comparing the total atom number in the second band to figure 5.6 (d) the atom number and the decay in the second band of the hexagonal lattice coincide with the hotter measurement in the bipartite square lattice.

The discrepancy of the condensate fraction as well as the good agreement of the decay to the hotter measurement are rather surprising as the temperature in the dipole trap yields 25 nK. This has been the main reason to suspect heating mechanisms in our hexagonal lattice setup. Therefore, we have investigated technical noise sources e.g. intensity and phase noise (see section 3.4). Still, higher heating rates can also originate from intrinsically different experimental parameters. This concerns the transfer method itself, differences in the band structure causing higher energy dissipation and differences in the lattice potential causing higher interactions.

Concerning the energy dissipation, the recoil energy in the hexagonal lattice is by a factor of 1.6 larger. Taking this into account, the bandwidth and band gap are about a factor of 3 larger ($\sim$ 300 Hz versus $\sim$ 100 Hz, and $\sim$ 13 000 Hz versus $\sim$ 5000 Hz). Thus, the hexagonal lattice has a clear disadvantage in terms of energy, which is dissipated during condensation from the Γ to K-points or when decay from

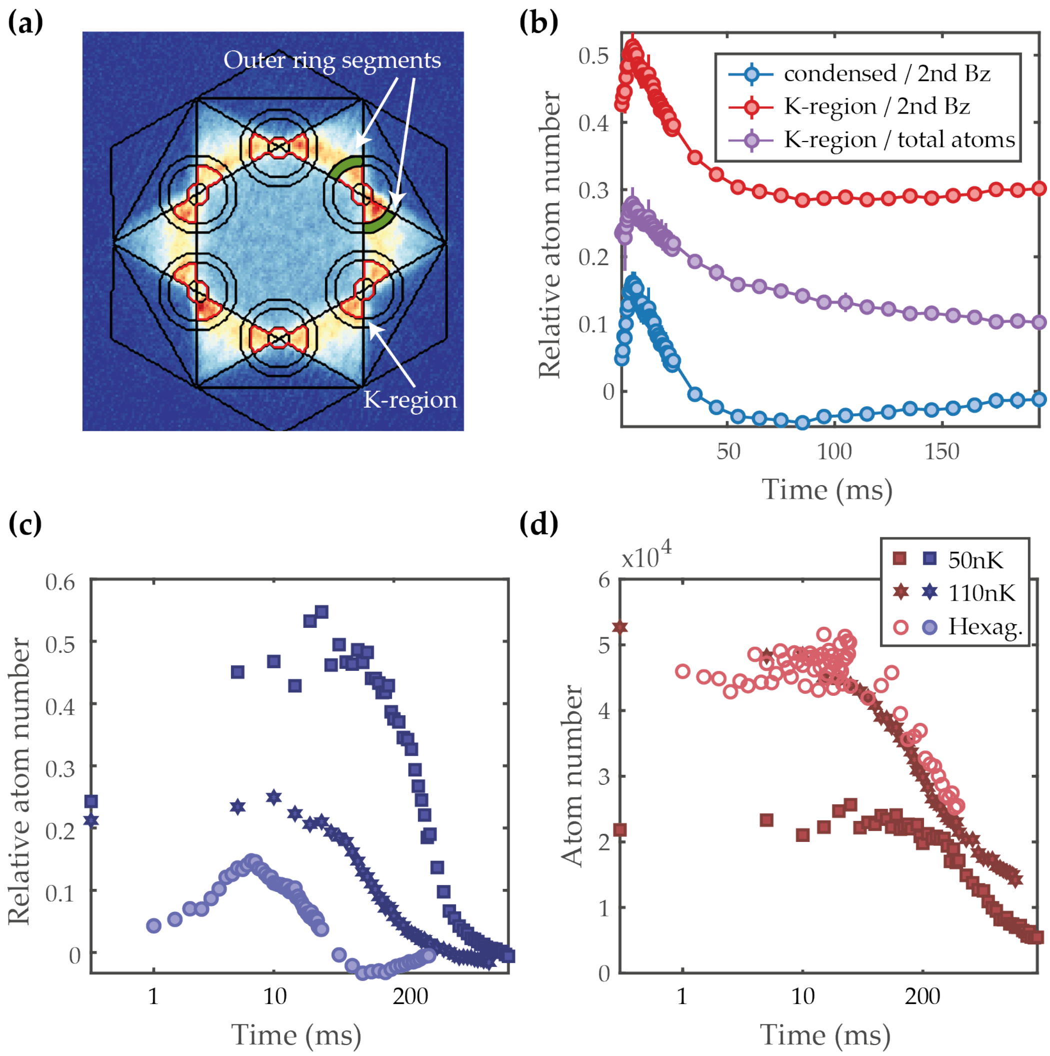

FIGURE 5.6: Comparison of the honeycomb lattice with the bipartite square lattice. (a) Definition of masks to obtain an estimate for the condensate fraction in band mapping images. (b) Condensate fraction and atoms in the K-region normalized to either the second Brillouin zone or the total atom number. (c) Condensate fraction in the hexagonal lattice (circles) compared to two different data sets at 50 nK and 110 nK in the square lattice lattice from [36]. (d) Absolute atom number in the second Brillouin zone again in comparison with the two mentioned data sets. For clarity of the presentation error bars are omitted in all data series.

the excited to the ground state occurs.

In addition, the interaction in the hexagonal lattice is increased due to the tight confinement of the lattice tubes (see section 5.3.1). For instance, the radial frequency of the initial state yields $\omega_\perp = 33.3\,\mathrm{kHz}$ compared to $\omega_\perp = 18.5\,\mathrm{kHz}$ in the square lattice. Assuming 1D-tubes, this results in an increased interaction of a factor of 1.8 ($g_{1D} = 2a\hbar\omega_\perp$). This increases the collision rate both within and likely also between the bands. Note that the differences in the lattice potential might also result in a different critical temperature for condensation. Given similar starting parameters due to the same species a lower T_c in the hexagonal lattice might explain the lower condensate fraction.

Finally, we emphasize that in the bipartite lattice the metastable state is protected by destructive interference [36]. It is unclear if a similar state also exists in the hexagonal lattice.

5.3 Key ingredients for condensation

In the following section we summarize the central experimental results and discuss the limitations of the experimental realization. For the argumentation we occasionally refer to calculations from our collaborators Georgios Koutentakis and Simos Mistakidis, which we aim to publish in a joint publication focusing on the condensation dynamics in the second band.

5.3.1 Lattice dimensionality

The lattice dimensionality is important regarding two aspects: (1) the initial state can be imagined as a 2D-array of weakly coupled tubes and (2) the lattice tubes can serve as a reservoir for energy dissipation [34, 36]. In the following we focus first on the initial state at the optimal parameters for condensation.

Probing the initial state after TOF and band mapping shows a broad momentum distribution without any visibility as depicted in figure 5.7. Since the ground bands have a bandwidth of less than 0.3 Hz tunneling is low during the holding time of the experiment (typically 2 ms) and bosonic enhancement of the tunneling between the tubes.

Ultracold gases in deep optical 2D-lattices are first of all characterized by highly anisotropic tubes $\omega_z \ll \omega_\perp$. The tubes can be classified into different regimes by a dimensionless parameter

$$\gamma = \frac{m g_{1D}}{\hbar^2 n_{1D}} \tag{5.1}$$

defining the ratio of interaction energy and kinetic energy of the ground state for zero temperature[1] [136]. Here, m denotes the atomic mass, g_{1D} the 1D interaction potential and n_{1D} the 1D density. In the case of $\gamma \ll 1$ with high densities in

[1]For the description of finite temperature interacting 1D-systems γ and an additionally reduced temperature are need to fully characterize the system [135].

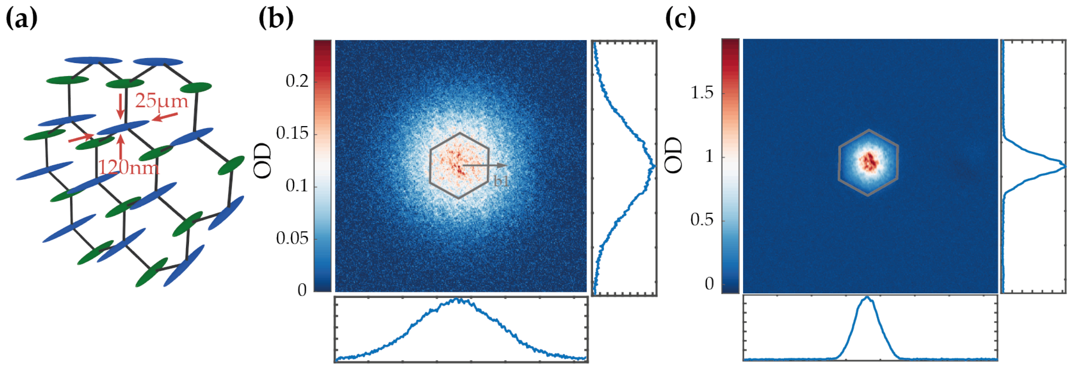

FIGURE 5.7: Initial state. (a) Geometry of the tubes in the hexagonal lattice denoted by the radial oscillator length and the Thomas-Fermi radius in the longitudinal direction. (b) TOF and (c) band mapping images after having ramped up the lattice to $V_{2D} = 8\,\mathrm{E_{rec}}$ and holding for 2 ms. Also depicted are the respective horizontal and vertical profiles. Fitting with a Gaussian the FWHM in units of the reciprocal lattice vector $\boldsymbol{b}_1$ yields for (b) 1.9 and for (c) 0.5.

harmonically confined systems the mean field description can be applied. In the strongly interacting regime called the Tonks-Girardeau regime for $\gamma \gg 1$ bosons inhibit fermionic like properties (experimentally realized [137, 138]). For our system we estimate the parameter $\gamma \approx 0.2$, which is slightly lower but in vicinity to experiments investigating 1D-systems [98, 139]. Extensive information on the physics of 1D-interacting bosonic systems can be found in the review by Cazalilla et al. [140].

Concentrating further on our system, a single tube can be described within the one-dimensional mean-field theory. Strictly speaking the 3D mean-field theory is not valid. We fulfill the condition where the radial motion of the particles freeze out: $Naa_\perp/a_z^2 \ll 1$ where N denotes the atom number in the central tube, a the s-wave scattering length, $a_\perp$ the radial and a_z the longitudinal oscillator length ($a_z = \sqrt{\hbar/m\omega_z}$. In table 5.2 we summarize the characteristic parameters for the initial state before the transfer to higher Bloch bands based on the text book by Pitaevski and Stringari [120].

In order to describe the initial state, it is important to discuss the temperature in such harmonically trapped 1D-systems. Here, reaching temperatures lower than the degeneracy temperature $T_d \approx N\hbar\omega_z \approx 720\,\mathrm{nK}$ is only sufficient for so-called quasi-condensates where phase fluctuations along the axial direction prevail but density fluctuations do not occur. For true condensation, T should be lower than the critical temperature for phase fluctuations $T_\phi = \hbar\omega_z/\mu \approx 15\,\mathrm{nK}$. Our estimation of the BEC temperature in the dipole trap yields 23 nK, thus minor phase fluctuations could occur making a quasi-condensate likely. However, large phase fluctuations seem unlikely due to the short holding time of only 2 ms in the deep lattice before the transfer. Furthermore, the broadening of the quasimomentum distribution with increasing holding time requires further investigation. This question will be further analyzed in the PhD thesis of A. Ilin.

We now turn to discussing the second aspect of the lattice dimensionality i.e. the lattice tubes can serve as a reservoir for dissipation of energy [34, 36]. To gain

	2nd band	4th band
lattice depth V_{2D} (E_{rec})	8	14
initial angle α	$0°$	$0°$
radial frequency $f_\perp$ (kHz)	33.3	47.1
axial frequency f_z, values measured (Hz)	75(1)	105(1)
radial oscil. length $a_\perp$ (nm)	59	50
axial oscil. length a_z (μm)	1.25	1.05
atoms in central tube	≈ 200	≈ 200
condition 1D mean field $Naa_\perp/a_z^2 \ll 1$	0.038	0.045
TF-radius $r_{TF,z}$ (μm)	12.7	11.3
T_d, in 1D (nK)	720	1010
T_ϕ (nK)	15	17

TABLE 5.2: Parameters of the initial state for $|2, -2\rangle$.

insights on the influence of the tube direction we benefit from the possibilities offered by our experiment. First, we applied additionally the orthogonal 1D-lattice to the 2D-hexagonal lattice. At the optimal parameters this hinders the emergence of coherence in the second band. Delaying the switch-on of the 1D-lattice to the maximum coherence rapidly destroys the coherence even for very shallow 1D-lattices. Thus, the 2D-lattice with its tubes seems to be a prerequisite for the emergence of coherence in higher bands for in deep lattices e.g. on the order of $V_{2D} \approx 8\,E_{rec}$.

Second, we have used the additional imaging axis to image the tube direction during the condensation process. We observed a strong increase of the width showing that the energy increases along the tubes. Here, a systematic study is required comparing the width in the lattice and tube plane of the first band and second band (see PhD thesis A. Ilin).

5.3.2 Critical temperature

Keeping the temperature below the critical temperature T_c is essential for condensation in higher bands. T_c has been calculated from our theory collaborators being on the order of 35 nK to 80 nK for realistic lattice parameters. This is close to the estimated temperature of the BEC ($T \approx 25$ nK) revealing a small temperature margin below T_c. Further, being close to T_c limits the condensate fraction. We evaluated the maximum condensate fraction in the experiment to be between 15 % and 25 %, which is similar to the theoretical expectation but lower than in the bipartite square lattice. This can stem from the aforementioned different lattice parameters (see section 5.2.3), a higher initial temperature in the deep lattice, intrinsically different decay or heating processes discussed further below.

Furthermore, a considerable population remains in the first band after the transfer. Here, theory currently suggests that the first band can act as a bath, which might support cooling. An experimental verification by emptying the first band would be helpful. Note that the condensed fraction is also sensitive to the absolute atom number in the system. A smaller atom number of $\sim 1.0 \times 10^5$ seems to be favorable.

5.3.3 Increasing lifetime

Identifying possible heating mechanisms is vital in order to increase the lifetime of superfluid states in higher bands. The condensed fraction and the lifetime are much smaller than the superfluids realized in the bipartite cubic lattice (section 5.2.3).

First, heating can occur in the initial state of the lattice. The initial state shows a broadening in momentum space with increasing holding time (e.g. factor 1.4 within the first 100 ms), which could indicate that the ground state of the final lattice configuration is not reached experimentally. Additionally, for longer holding times excitations to higher bands and an increased atom loss are observed. These observations explain why the transfer to the second band works best for very short holding times in the lattice and why they could be limitations for the lifetime in the excited bands. Another possible heating origin is the harmonic confinement of the lattice, which is ramped up within 100 ms. This could be minimized by using different ramps, by using larger lattice beam waists, which are currently relatively small (115 µm) or by compensating the harmonic confinement with additional light potentials. This would also increase the lengths of the tubes lowering the barrier to escape for high kinetic atoms. Phase noise cannot be completely ruled out as a heating mechanism. However, note that three other experiments with three running-waves lattice beams state explicitly that phase noise does not disturb the experiments (cf. section 3.4.3) [107, 108, 110]. Spontaneous scattering as a heating source is unlikely ($\Gamma_{sc} \approx 33\,\mathrm{s}^{-1}$).

Second, the transfer method can cause heating. The rapid rotation of the quantization axis induces a sudden single oscillation of the BEC on the scale of the BEC width. This effect will decrease with lower magnetic fields but the spin-polarization must still be maintained (see section 4.3.2). To estimate experimental artifacts induced by the rotation we have used spin-flips as a transfer method (appendix C.1). Indeed the rotation induces kinks in the visibility. Another aspect is the remaining atomic fraction in the lower band after the transfer. Even though our theory collaboration can show that the first band can serve as a bath, also heating due to the lowest band is possible.

Third the population of higher bands can also contribute to heating. Our theory collaborators have identified two important processes. Two-body collisions within the second band and two-body collisions where one of the atoms decays to the ground band. Due to the large bandgap (13 kHz) very few decay processes could lead to an evaporation of the condensate and heat the system above T_c.

Taken together, each of the stages in the preparation scheme should be optimized: (1) the preparation of the initial state, (2) the transfer method and, (3) the population of higher bands. While minimizing heating in stage (1) and (2) requires rather technical improvements, improvements in stage (3) probably require a different atomic species or tunable interactions.

5.3.4 Control of the band structure by intensity imbalance

A condensate in the second band in a perfectly adjusted and calibrated lattice is expected to emerge at the K- and K′-points after TOF. However, the locations of the minima in the second band can be easily modified by an intensity imbalance of the different lattice beams. On the one hand this is advantageous for the engineering of unconventional band structures in higher bands. On the other hand this requires a precise intensity balancing of the lattice beams for preparing the condensates at the K- and K′-points.

For a condensate in the second band in a perfectly adjusted and calibrated lattice we expect to observe the population at the K- and K′-points after TOF. Yet, after performing a pairwise 1D-calibration of all three lattice beams an asymmetric distribution is observed. Thus, the minima of the second band are apparently not located at the K- and K′-points. Most likely this is due to imperfections in the adjustment of the polarization and lattice beam angles, which also modify the band structure. These imperfections can be compensated by adjusting the lattice intensity such that the minima in the second band are located at the K-points. Figure 5.8 shows the influence of intensity imbalance. Four of the six minima merge at the M-points of the Brillouin zone for an increased intensity in a single beam. For a decrease of intensity they move apart. The beam, which produces the deformation can be inferred from the symmetry axis.

At the experiment this has been typically ensured by lattice calibration. Knowing the lattice depth V_{2D} is crucial for the presented measurements . Yet, it is not possible to directly measure the beam power in the science chamber to determine the lattice depth. Instead, a versatile toolbox of precise lattice calibration methods exists. This includes Kapitza-Dirac, Stückelberg-interferometry or amplitude modulation, which have been implemented at our experiment and will be described in detail in the PhD thesis of A. Ilin. Historically, we have done lattice calibration at our experiment via parametric heating [44]. Commonly, it was performed separately for the three pairwise 1D-lattices. Hence, each of the three beams can be calibrated to the same lattice depth and contributes equally to the overall lattice depth V_{2D}. However, this is a time-consuming procedure, especially if conducted regularly. More importantly, it is not precise enough for the condensation in the second band. Thus, we modified the procedure in order to calibrate directly the 2D-lattice by adjusting the position of the minima at K and K′.

To finish the calibration procedure, the lattice depth is calibrated directly in the 2D-lattice via parametric heating to the 7th Bloch band offering the advantage of a high coupling efficiency [44].

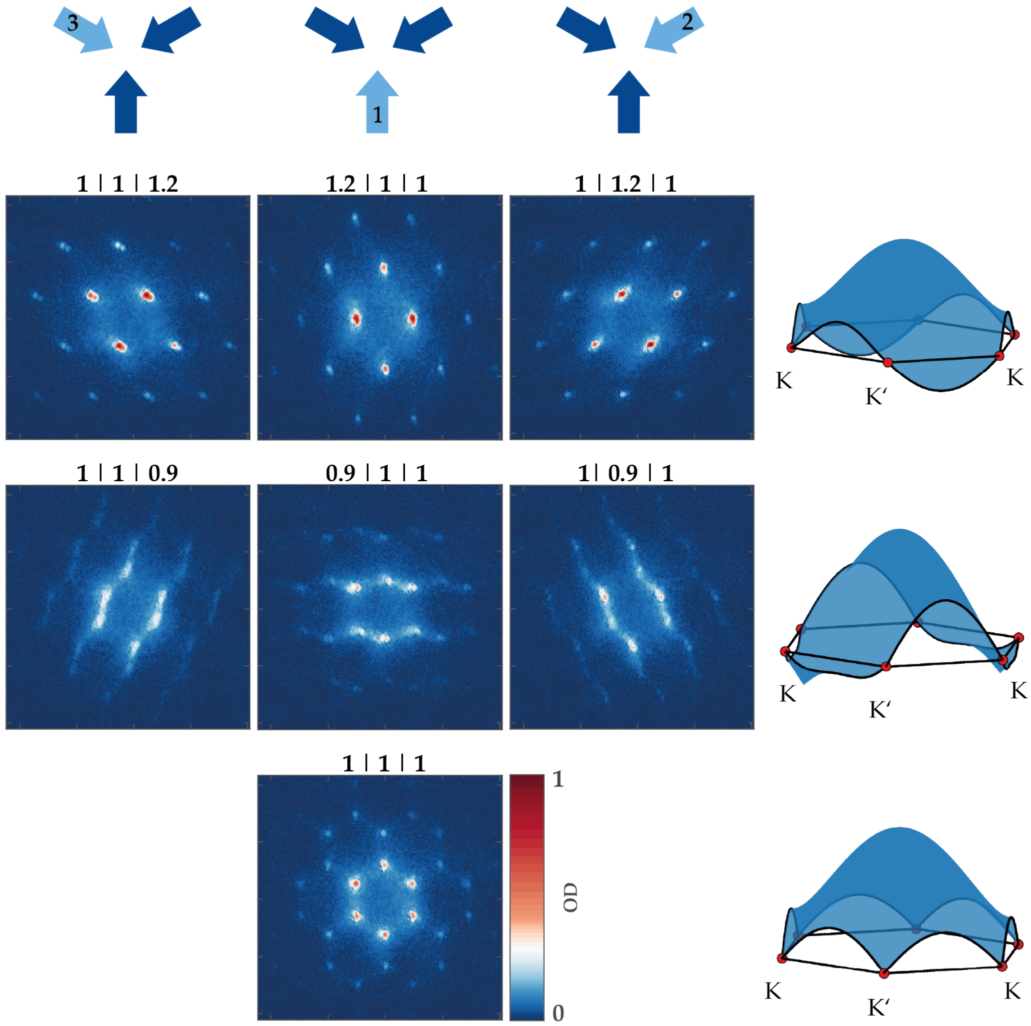

FIGURE 5.8: Control of the band structure by intensity imbalance. The three laser beams are numbered as in the experiment. The relative intensity deviation from a symmetric ordering of the K-points is denoted for each respective laser beam by the numbers above each absorption image. For higher intensities two minima at the K-points merge at the M-points. For lower intensities they move apart. This is effect is also clearly visible in the band structure of the second band in the right column.

5.4 Conclusion and outlook

To conclude, condensation in higher bands, especially for the evolution of a wave packet initially prepared at a band maximum is intriguing. Driven by interactions recondensation can occur rapidly within very few milliseconds at the band minima forming a metastable superfluid in higher bands.

We have realized condensation in the second and fourth Bloch band of the optical honeycomb lattice. The engineered band structures for the second and fourth band are similar regarding the band gap and the bandwidth despite the different band geometry i.e. the location of the band maxima and minima.

We analyze the condensation dynamics by evaluating coherence and band population and identify four characteristic stages. (1) After the transfer to the excited band a broad population of quasimomenta is observed. (2) Driven by collisions the population redistributes within a few milliseconds to the band minima. Meanwhile coherence emerges and reaches a maximum in less than 10 ms due to the increased tunneling in the excited band. The maximum condensate fraction is estimated to be between 15 % and 25 % for the second band and to be 35 % for the fourth band. For the second band the condensate fraction is about three times smaller than in the bipartite square lattice, which can originate from either intrinsic differences between the two lattices or from heating mechanisms stemming from the preparation and leading to a too large initial temperature. (3) In the following the coherence decays. This might be explained with a collisional decay to the ground band. Few decay processes already dissipate a large amount of energy and eventually lead to an evaporation of the condensate. (4) Subsequently, band relaxation to the ground band occurs on a longer timescale (e.g. for the second band $\tau_{\mathrm{coh}_2} = 18(1)$ ms versus $\tau_{\mathrm{band}_2} > 57(2)$ ms and for the fourth band $\tau_{\mathrm{coh}_4} = 7(1)$ ms versus $\tau_{\mathrm{band}_4} > 37(2)$ ms).

Furthermore, we have explored a large parameter space to identify relevant scalings for condensation and have verified experimentally the importance of the lattice tubes as an energy reservoir. The emergence of coherence has been hindered effectively by superimposing an additional 1D-lattice.

Finally, an interesting question is the nature of the engineered quantum many-body state, which will be addressed in detail in the PhD thesis of A. Ilin. Superposition states of K and K' or fragmented states are both imaginable. Here, in near future a new probing method with single-site resolution, the quantum gas magnifier, will reveal further insights. In the following two further research perspectives are presented.

Engineering sp^2-like Bloch states

So far, the realized initial Bloch state in the first band and the final Bloch state in the second band show a similar s-wave character. In figure 5.9 the densities of the Bloch functions show an occupation on the A-sites of the lattice. However, the Bloch states are modified by increasing α, which corresponds to a modification of the energy

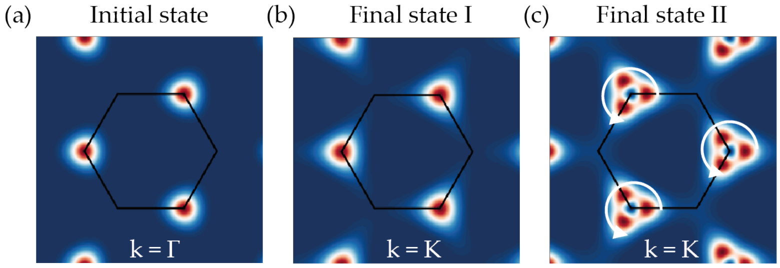

FIGURE 5.9: Density of the Bloch functions in the spin-dependent honeycomb lattice for momentum $\boldsymbol{k} = \Gamma$ or K. The lattice depth V_{2D} is kept fixed, while the angle α is varied. (a) Initial state in the first band ($\alpha = 0°$). (b) Bloch state at the optimal parameters $\alpha = 106°$. (c) Bloch state at $\alpha = 145°$. Here, a sp^2-like density pattern is depicted. The white arrows denotes a phase winding of 2π around the lattice sites.

offset ΔV_{AB}. If the increase occurs slowly, the state should adiabatically follow the second band (cf. figure 4.4). Then, the Bloch state occupies the B-site of the lattice and the density pattern shows a sp^2-like shaped form (figure 5.9 (c)). The density has a node at the lattice site but increases along the lattice bonds and the phase pattern shows a winding of 2π around the sites. As only the B-lattice sites are occupied, the state is characterized by a rectified orbital angular momentum providing an ideal example for an unconventional superfluid.

Bosonic superfluids in higher bands with tunable interactions

Throughout this thesis we have seen indications that interactions influence strongly the condensation process and lifetime in higher Bloch bands. Thus, modifying the scattering length via Feshbach resonances opens new possibilities to create longer living states. For the fermionic spin mixtures of ^{40}K such an increase in lifetime could be observed for particle-like excitations to the second band in a 1D-optical lattice [141]. As addressing the Feshbach resonance of ^{87}Rb is experimentally unfavorable we have already begun first steps to implement the bosonic species of potassium ^{39}K. This includes the integration of potassium dispensers (see section 2.1) and the setup of a compact laser system for ^{87}Rb (see A. Khan [142]) making room for an additional ^{39}K laser setup. The light shifts induced by the existing spin-dependent hexagonal lattice at 830 nm are indeed too small for significant AB-potential offsets. The development of a new lattice setup will be a central task.

Appendix A

Band structure of the explored parameter region

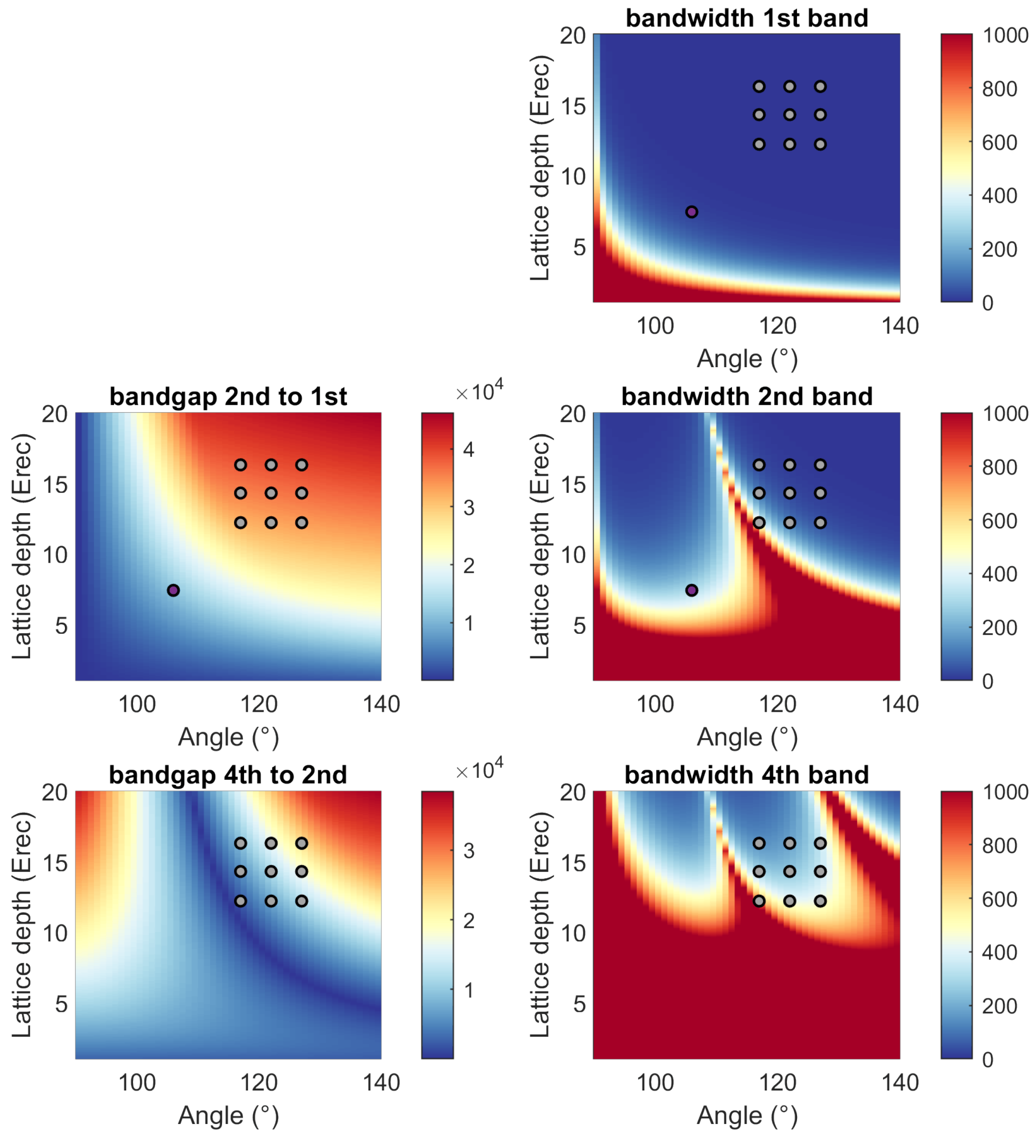

FIGURE A.1: Bandwidth and band gap with respect to the lattice depth V_{2D} and quantization axis angle α. The band gap and bandwidth are given in units of Hertz. Here, the bandwidth is defined between the K- and Γ-points and it is cut off at 1 kHz. Circles mark some of the measurements in this thesis.

Appendix B

A model-free description with PCA

Principal component analysis (PCA) constitutes a standard method in multivariate statistical analysis and offers two immense advantages for the evaluation of absorption images. First it takes all information of the input images into account and thus can reveal information that would remain hidden otherwise. Second it is model-free, which means defining masks imposing already a physical idea is not necessary. An excellent review on PCA has been written by Jolliffe and Cadima [143]. In quantum gas experiments PCA has been used e.g. for an interferometry experiment [144] or for measuring collective excitations [95]. At our experiment it has been applied for investigating symmetry breaking in artificial gauge field [46]. In the course of this PhD project the author has used PCA regularly on different data sets. In the following we perform PCA to describe the condensation process in the second band by reevaluating the band mapping images from section 5.1.2.

B.1 Principal component analysis

Our data sets consist of about 300 absorption images (measurements) n with about four images per time step. Each image has a size of $215x215 \approx 4 \times 10^4$ pixels (number of variables) p and is expressed as a row vector. The aim is now to find a new set of uncorrelated variables, the principal components, which contain most of the the variation of the original variables [145]. Here, we only outline the procedure and refer the reader to the references given above.

First, the n images of the series are expressed as row vectors $\boldsymbol{r}_i = (r_1, r_2, ..., r_p)$ with the row index $i = 1, 2, ...n$. The mean image $\bar{r}$ of the data set is subtracted from each image $\boldsymbol{r}_i$ and the resulting centered images are expressed in a so-called centered data matrix X^* of the size $n \times p$ and with typically $n \ll p$. The matrix product

$$X^{*T} \cdot X^* = S(n-1) \tag{B.1}$$

denotes the covariance matrix S for the centered data. S contains the variance of the pixels on the diagonal and the correlations in between the pixels in the off-diagonal elements. Then, the idea is to find a set of new basis vectors (basis images), which are uncorrelated. Different algorithms exist for PCA. The scheme relies on diagonalization of the covariance matrix S. Its eigenvectors represent the principal components (PC), which when applying the PCA method are ordered with decreasing variance. Finally, each image of the series can be reconstructed by

$$\boldsymbol{r}_i = \bar{r} + \sum_{j=1}^{p} Y_{ji} \boldsymbol{u}_j, \tag{B.2}$$

which is the sum of the mean image $\bar{r}$ and the linear combination of the weight (score) Y_{ji} and the eigenvectors $\boldsymbol{u}_j$ of the matrix S. Typically, it is sufficient to take only the first few principal components into account as they capture most of the variance in the data set. In the following we present the principal components and plot their weight (score) as a function of holding time.

B.2 Condensation dynamics in band mapping images

In general PCA finds the same behavior as is observed with the mask evaluations of the band mapping images. In figure B.1 (a) we show the first three principal components, which represent together a variation of 80 % in the data set. Comparing all three orthogonal basis images we recognize the shape of the Brillouin zones and the regions of higher atomic density i.e. at the K- and K′-points. PC 1 illustrates the population at the K-points for negative pixel values (blue) and a broad distribution in the first and in the second Brillouin zone for positive pixel values (red). The scores of each PC as a function of time in figure B.1 (b) show that PC 1 represents best the emergence and decay of condensation and also the band decay. In addition, PC 2 shows the heating in the second band followed by band decay to the first band and represents the separation of timescales for the decay of coherence and band population. Also note the increasing population in higher bands (band index > 3), which could indicate heating processes. PC 3 illustrates dynamics likely stemming from dipole oscillations and at the same time shows a redistribution from a predominate K- and K′-point population (red) to a broad momentum occupation in the second band.

(a)

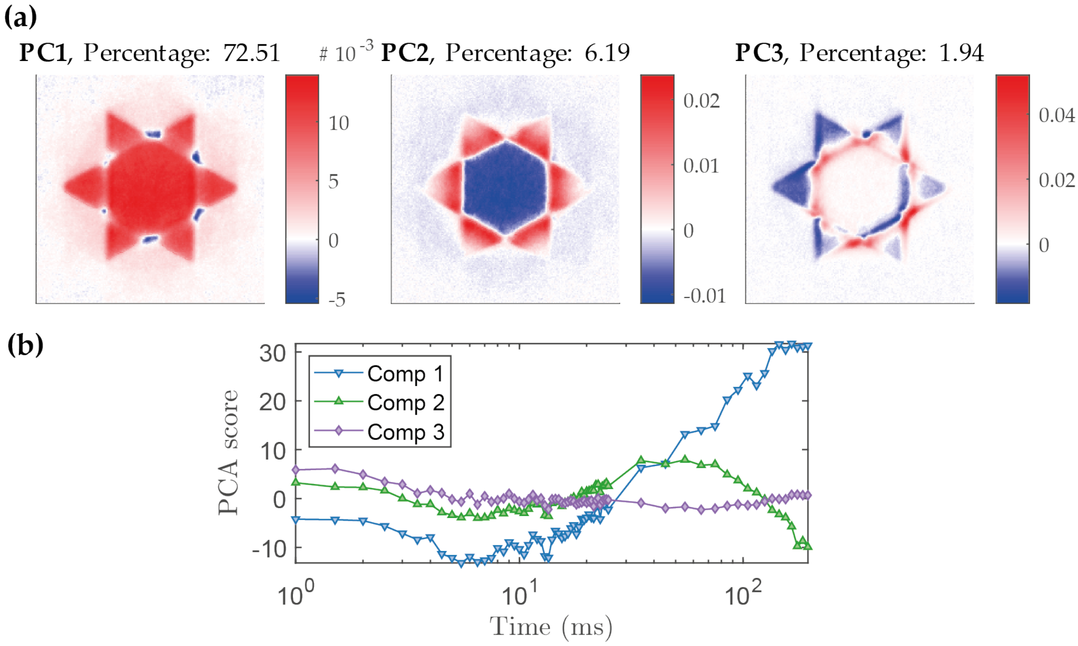

FIGURE B.1: Principal component analysis of band mapping images depicting the condensation dynamics in the second band (see section 5.1.2). (a) The first three principal components (PCs) of the data set. (b) Score of the principal components plotted as a function of holding time after the transfer to the second band.

Appendix C

Further measurements

C.1 Condensation in second band in $|F = 1, m_F = -1\rangle$ and comparison of two different transfer methods

In this section we present complementary measurements to the condensation dynamics in chapter 5. In the same manner as in $|2, -2\rangle$ a coherent state in the second band can also be prepared in $|1, -1\rangle$. Generally, we observe a slightly higher optical density in higher bands in $|2, -2\rangle$ than $|1, -1\rangle$ ($\sim 10\,\%$), which is the reason for using predominately $|2, -2\rangle$ during this PhD project. Nevertheless it is useful to discuss the differences between the two realizations.

- The interaction in $|1, -1\rangle$ is slightly higher than in $|2, -2\rangle$, which is relevant for heating processes (compare the s-wave scattering lengths $a_0 = 110\, a_B$ versus $a_0 = 89.4\, a_B$).
- Assuming 1D-tubes in the initial state ($\alpha = 0\,°$), the interaction can be estimated by g_{1D} (see section 5.3.1). Even though radial confinement $f_\perp = 30.9\,\mathrm{kHz}$ is lower by 10 % in $|1, -1\rangle$, the increased scattering length cannot be compensated in g_{1D}. Thus, also in the initial state the interaction is increased.
- Although the experimental parameters for optimal condensation are different ($\alpha = 125\,°$ for $|1, -1\rangle$ instead of $\alpha = 106\,°$ for $|2, -2\rangle$), the relevant physical quantities are similar. Both potentials are linked by the effective magnetic quantum number $m = (-1)^{F+1} m_F \cos\alpha$, which is the same for both states (cf. [38]). The band structure in term of band gap and bandwidth are the same.
- Note that due to the available lattice laser power with $|F = 1, m_F = -1\rangle$ at $\lambda = 830\,\mathrm{nm}$ the optimal condensation parameters for the fourth band cannot be reached as V_{2D} remains too low. This disadvantage and the observation to reach slightly higher optical densities with $|2, -2\rangle$ are the reasons for using typically $|2, -2\rangle$ during this PhD project.

In general condensation dynamics for $|1, -1\rangle$ and $|2, -2\rangle$ are very similar. Both feature the same timescales and shape of the visibility and optical density for the optimal parameters. In figure C.1 we present a precise measurement for $|1, -1\rangle$ where each data point has been averaged 14 times (blue curve). Thus, the shape of the

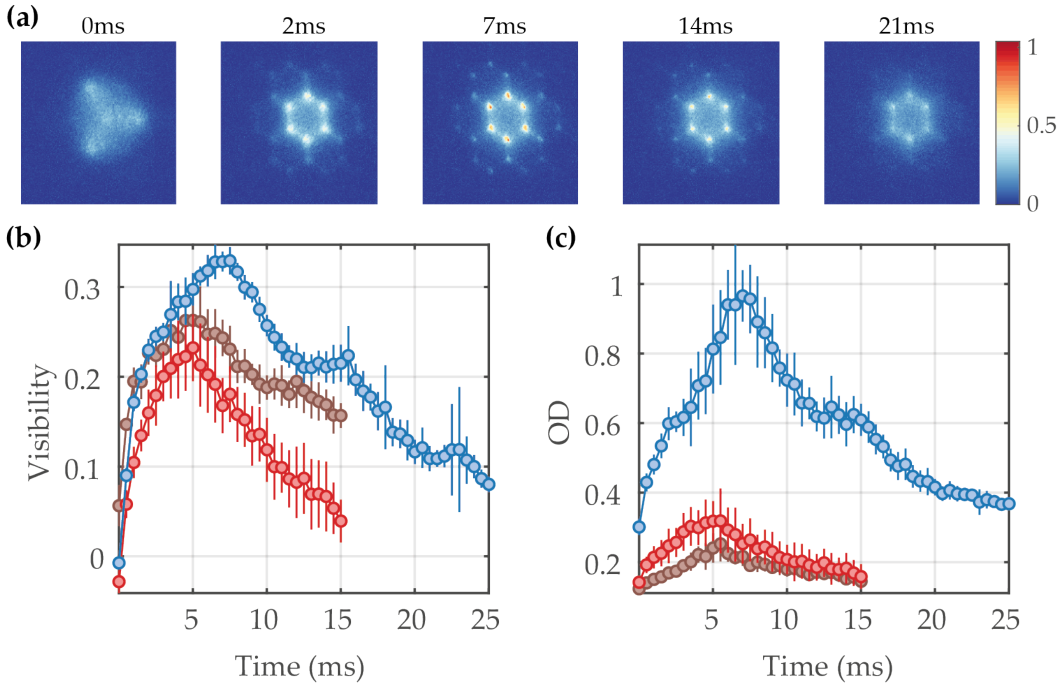

FIGURE C.1: Visibility and the maximum optical density after transfer to the second band at optimal parameters in $|F = 1, m_F = -1\rangle$. (a) Exemplary TOF-images scaled to the maximum optical density of the blue data points. (b) Visibility for different holding times comparing three different measurements. First, a measurement at optimal parameters where each data point has been averaged 14 times (blue curve). Second, a measurement where the transfer has been done with an rf-pulse (red curve) and third, a reference measurement in equal conditions (brown curve). The rf-pulse and reference measurement both use the same initial AB-offset for comparability. (c) Maximum of the optical density of the three different measurements in dependence of holding time.

visibility with the plateau-like structure at 14 ms and 23 ms is reliably resolved. In section 4.3.2 we state as a possible reason the induced motion by the magnetic field rotation. Indeed this hypothesis is supported by the fact that these plateau-like features are not present in the measurement where the transfer to the second band has been performed by an rf-pulse (red curve). For direct comparison we also present a reference measurement (brown curve) in equal conditions e.g. atom number and experimental adjustments. Here the rotation of the quantization axis as a transfer method inhibits also small plateau-like features (brown curve).

For completeness we show here in the following table the experimental parameters of the three measurements. In conclusion the plateaus in the shape of the visibil-

	precision measurement	**Rf-pulse measurement**	**reference measurement**
depth V_{2D} (E_{rec})	8.1	8.4	8.4
initial angle α	0°	54°	54°
final angle α	125°	rf-pulse equal 126°	126°

TABLE C.1: Central parameters of the three measurements presented in figure C.1. Note that the initial angle at the rf-pulse measurement is necessary to realize the same AB-offset being equivalent to a rotation to $\alpha = 106°$.

ity can likely be attributed to artifacts from the rotation of the quantization axis. The overall time scale of the condensation and the decay of the coherence remain similar with both transfer methods. The rotation method reaches a marginally higher visibility but future studies will need to show if this also yields for a more carefully prepared rf-pulse. Movements of e.g. the center-of-mass are clearly reduced in comparison to the rotation which can exert forces by magnetic field gradients.

C.2 Choice of masks for evaluation of visibility

Visibility is a widely used quantity to analyze TOF images for quantifying the coherence in optical lattices (see section 3.3. The visibility introduced by Gerbier et al [133] has been weakly dependent on the mask sizes (3x3 pixels). For the comparison of different measurements it is crucial to be aware of the variations.

In the following we analyze the influence of different mask sizes on the visibility for the data series presented in section 5.1.2. In addition, we compare the visibility for the different Bragg peaks orders in TOF images. Figure C.2 depicts the results. The visibility of the zeroth order depends still significantly on the mask sizes. The maximum visibility for 10 pixel radii yields about 0.4 while it reaches 0.7 for radii of 3 pixels. For higher orders this discrepancy shrinks as the incoherent background of the first band attributes less to the contrast. Normalizing the different visibilities to their respective maximum shows that it is independent of the circular masks sizes which proved advantageous for comparisons to theory.

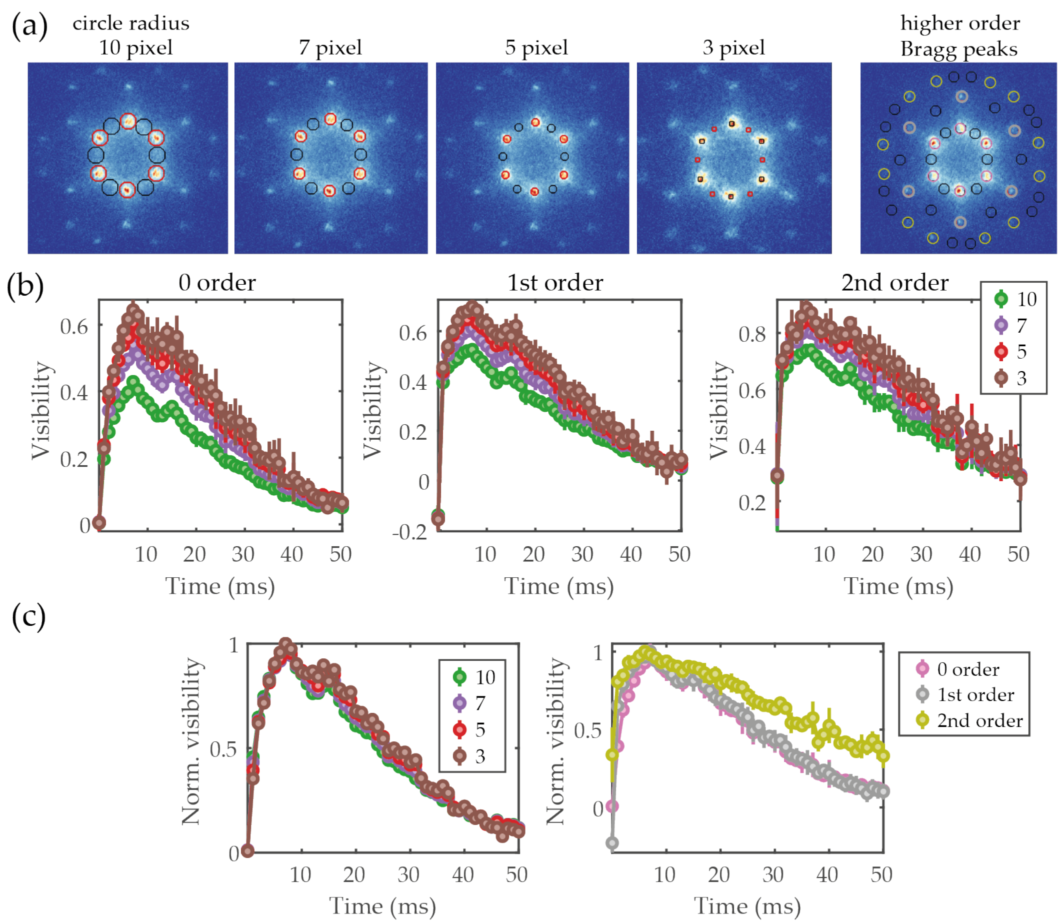

FIGURE C.2: Influence of the circular masks on the visibility. (a) Different radii in pixels of the circular visibility masks. In the far right image masks are placed around the higher order Bragg peaks. (b) Comparison of the visibility for different masks sizes for the zeroth, first and second order of the Bragg peaks. (c) *Left:* visibility for different circle radii of the zeroth order normalized to its respective maximum. *Right:* Visibility of the different order normalized to its maximum.

Bibliography

[1] M. H. Anderson et al. "Observation of Bose-Einstein Condensation in a Dilute Atomic Vapor". In: *Science* 296,5221 (1995). ISSN: 0036-8075 (cit. on p. 1).

[2] C. C. Bradley et al. "Evidence of Bose-Einstein Condensation in an Atomic Gas with Attractive Interactions". In: *Physical Review Letters* 75.9 (1995), pp. 1687–1690. ISSN: 0031-9007. DOI: `10.1103/PhysRevLett.75.1687` (cit. on p. 1).

[3] K. B. Davis et al. "Bose-Einstein Condensation in a Gas of Sodium Atoms". In: *Physical Review Letters* 75.22 (1995), pp. 3969–3973. ISSN: 0031-9007. DOI: `10.1103/PhysRevLett.75.3969` (cit. on p. 1).

[4] D. S. Jin et al. "Collective Excitations of a Bose-Einstein Condensate in a Dilute Gas". In: *Physical Review Letters* 77.3 (1996), pp. 420–423. ISSN: 0031-9007. DOI: `10.1103/PhysRevLett.77.420` (cit. on p. 1).

[5] M.-O. Mewes et al. "Collective Excitations of a Bose-Einstein Condensate in a Magnetic Trap". In: *Physical Review Letters* 77.6 (1996), pp. 988–991. ISSN: 0031-9007. DOI: `10.1103/PhysRevLett.77.988` (cit. on p. 1).

[6] M. R. Andrews et al. "Observation of Interference Between Two Bose Condensates". In: *Science* 275.5300 (1997), pp. 637–641. ISSN: 00368075. DOI: `10.1126/science.275.5300.637` (cit. on p. 1).

[7] I. Bloch, T. W. Hänsch, and T. Esslinger. "Measurement of the spatial coherence of a trapped Bose gas at the phase transition". In: *Nature* 403.6766 (2000), pp. 166–170. ISSN: 0028-0836. DOI: `10.1038/35003132` (cit. on p. 1).

[8] M. R. Matthews et al. "Vortices in a Bose-Einstein Condensate". In: *Physical Review Letters* 83.13 (1999), pp. 2498–2501. ISSN: 0031-9007. DOI: `10.1103/PhysRevLett.83.2498` (cit. on p. 1).

[9] K. W. Madison et al. "Vortex Formation in a Stirred Bose-Einstein Condensate". In: *Physical Review Letters* 84.5 (2000), pp. 806–809. ISSN: 0031-9007. DOI: `10.1103/PhysRevLett.84.806` (cit. on p. 1).

[10] J. R. Abo-Shaeer et al. "Observation of vortex lattices in Bose-Einstein condensates". ENG TS - PubMed. In: *Science (New York, N.Y.)* 292.5516 (2001), pp. 476–479. ISSN: 0036-8075. DOI: `10.1126/science.1060182PM-11264525M4-Citavi` (cit. on p. 1).

[11] B. DeMarco and D. Jin. "Onset of Fermi Degeneracy in a Trapped Atomic Gas". In: *Science* 285.5434 (1999), pp. 1703–1706. ISSN: 00368075. DOI: `10.1126/science.285.5434.1703` (cit. on p. 1).

[12] J. Bardeen, L. N. Cooper, and J. R. Schrieffer. "Theory of Superconductivity". In: *Physical Review* 108.5 (1957), pp. 1175–1204. ISSN: 0031-899X. DOI: 10.1103/PhysRev.108.1175 (cit. on p. 1).

[13] M. W. Zwierlein et al. "Observation of Bose-Einstein Condensation of Molecules". In: *Physical Review Letters* 91.25 (2003), p. 250401. ISSN: 0031-9007. DOI: 10.1103/PhysRevLett.91.250401 (cit. on p. 1).

[14] T. Bourdel et al. "Experimental Study of the BEC-BCS Crossover Region in Lithium 6". In: *Physical Review Letters* 93.5 (2004), p. 050401. ISSN: 0031-9007. DOI: 10.1103/PhysRevLett.93.050401 (cit. on p. 1).

[15] C. I. Westbrook et al. "Localization of atoms in a three-dimensional standing wave". In: *Physical Review Letters* 65.1 (1990), pp. 33–36. ISSN: 0031-9007. DOI: 10.1103/PhysRevLett.65.33 (cit. on p. 1).

[16] G. Grynberg et al. "Quantized motion of cold cesium atoms in two- and three-dimensional optical potentials". In: *Physical Review Letters* 70.15 (1993), pp. 2249–2252. ISSN: 0031-9007. DOI: 10.1103/PhysRevLett.70.2249 (cit. on p. 1).

[17] A. Hemmerich and T. W. Hänsch. "Two-dimesional atomic crystal bound by light". In: *Physical Review Letters* 70.4 (1993), pp. 410–413. ISSN: 0031-9007. DOI: 10.1103/PhysRevLett.70.410 (cit. on p. 1).

[18] D. Jaksch et al. "Cold Bosonic Atoms in Optical Lattices". In: *Physical Review Letters* 81.15 (1998), pp. 3108–3111. ISSN: 0031-9007. DOI: 10.1103/PhysRevLett.81.3108 (cit. on p. 1).

[19] M. Greiner et al. "Exploring Phase Coherence in a 2D Lattice of Bose-Einstein Condensates". In: *Physical Review Letters* 87.16 (2001), p. 160405. ISSN: 0031-9007. DOI: 10.1103/PhysRevLett.87.160405 (cit. on pp. 1, 64).

[20] M. Lewenstein et al. "Ultracold atomic gases in optical lattices: mimicking condensed matter physics and beyond". In: *Advances in Physics* 56.2 (2007), pp. 243–379. ISSN: 0001-8732. DOI: 10.1080/00018730701223200 (cit. on p. 1).

[21] I. Bloch, J. Dalibard, and W. Zwerger. "Many-body physics with ultracold gases". In: *Reviews of Modern Physics* 80.3 (2008), pp. 885–964. ISSN: 0034-6861. DOI: 10.1103/RevModPhys.80.885 (cit. on pp. 1, 37).

[22] I. Bloch, J. Dalibard, and S. Nascimbène. "Quantum simulations with ultracold quantum gases". In: *Nature Physics* 8.4 (2012), pp. 267–276. ISSN: 1745-2473. DOI: 10.1038/nphys2259 (cit. on p. 1).

[23] C. Gross and I. Bloch. "Quantum simulations with ultracold atoms in optical lattices". In: *Science* 357.6355 (2017), pp. 995–1001. ISSN: 0036-8075. DOI: 10.1126/science.aal3837 (cit. on p. 1).

[24] C. Wu. "Unconventional Bose-Einstein condensations beyond the "no-node" theorem". In: *Modern Physics Letters B* 23.01 (2009), pp. 1–24. ISSN: 0217-9849. DOI: `10.1142/S0217984909017777`. arXiv: `0901.1415` (cit. on p. 1).

[25] O. Dutta et al. "Non-standard Hubbard models in optical lattices: a review". In: *Reports on Progress in Physics* 78.6 (2015), p. 066001. ISSN: 0034-4885. DOI: `10.1088/0034-4885/78/6/066001` (cit. on p. 1).

[26] X. Li and W. V. Liu. "Physics of higher orbital bands in optical lattices: a review". In: *Reports on Progress in Physics* 79.11 (2016), p. 116401. ISSN: 0034-4885. DOI: `10.1088/0034-4885/79/11/116401` (cit. on p. 1).

[27] C. Wu et al. "Quantum Stripe Ordering in Optical Lattices". In: *Physical Review Letters* 97.19 (2006), p. 190406. ISSN: 0031-9007. DOI: `10.1103/PhysRevLett.97.190406` (cit. on p. 1).

[28] M. Di Liberto, A Hemmerich, and C Morais Smith. "Topological Varma Superfluid in Optical Lattices". In: *Physical Review Letters* 117.16 (2016), p. 163001. ISSN: 0031-9007. DOI: `10.1103/PhysRevLett.117.163001` (cit. on p. 1).

[29] A. Browaeys et al. "Transport of atoms in a quantum conveyor belt". In: *Physical Review A* 72.5 (2005), p. 053605. ISSN: 1050-2947. DOI: `10.1103/PhysRevA.72.053605` (cit. on pp. 1, 51).

[30] T. Müller et al. "State Preparation and Dynamics of Ultracold Atoms in Higher Lattice Orbitals". In: *Physical Review Letters* 99.20 (2007), p. 200405. ISSN: 0031-9007. DOI: `10.1103/PhysRevLett.99.200405` (cit. on pp. 1, 62).

[31] G. Wirth, M. Ölschläger, and A. Hemmerich. "Evidence for orbital superfluidity in the P-band of a bipartite optical square lattice". In: *Nature Physics* 7.2 (2011), pp. 147–153. ISSN: 1745-2473. DOI: `10.1038/nphys1857` (cit. on pp. 1, 51, 73).

[32] M. Ölschläger, G. Wirth, and A. Hemmerich. "Unconventional Superfluid Order in the F-Band of a Bipartite Optical Square Lattice". In: *Physical Review Letters* 106.1 (2011), p. 015302. ISSN: 0031-9007. DOI: `10.1103/PhysRevLett.106.015302` (cit. on pp. 1, 51, 73).

[33] T Kock et al. "Orbital optical lattices with bosons". In: *Journal of Physics B: Atomic, Molecular and Optical Physics* 49.4 (2016), p. 042001. ISSN: 0953-4075. DOI: `10.1088/0953-4075/49/4/042001` (cit. on pp. 1, 42, 51, 73).

[34] S. Paul and E. Tiesinga. "Formation and decay of Bose-Einstein condensates in an excited band of a double-well optical lattice". In: *Physical Review A* 88.3 (2013), p. 033615. ISSN: 1050-2947. DOI: `10.1103/PhysRevA.88.033615`. arXiv: `1308.4449` (cit. on pp. 1, 76, 77).

[35] T Kock et al. "Observing Chiral Superfluid Order by Matter-Wave Interference". In: *Physical Review Letters* 114.11 (2015), p. 115301. ISSN: 0031-9007. DOI: `10.1103/PhysRevLett.114.115301` (cit. on pp. 1, 51, 73).

[36] M Nuske et al. “Metastable order protected by destructive many-body interference”. In: (2020). DOI: 10.1103/PhysRevResearch.2.043210. arXiv: 2004.00620 (cit. on pp. 1, 51, 63, 70, 73–77).

[37] S. Jin et al. “Evidence of Potts-Nematic Superfluidity in a Hexagonal sp2 Optical Lattice”. In: *Physical Review Letters* 126.3 (2021), p. 035301. ISSN: 0031-9007. DOI: 10.1103/PhysRevLett.126.035301 (cit. on p. 2).

[38] D.-S. Lühmann et al. “Quantum phases in tunable state-dependent hexagonal optical lattices”. In: *Physical Review A* 90.1 (2014), p. 013614. ISSN: 1050-2947. DOI: 10.1103/PhysRevA.90.013614 (cit. on pp. 2, 31, 34, 36, 91).

[39] M Weinberg et al. “Breaking inversion symmetry in a state-dependent honeycomb lattice: artificial graphene with tunable band gap”. In: *2D Materials* 3.2 (2016), p. 024005. ISSN: 2053-1583. DOI: 10.1088/2053-1583/3/2/024005 (cit. on pp. 2, 36, 50).

[40] H. Schmaljohann. “Spindynamik in Bose-Einstein Kondensaten”. PhD thesis. Universität Hamburg, 2004 (cit. on pp. 5, 7).

[41] M. Erhard. “Experimente mit mehrkomponentigen Bose-Einstein-Kondensaten”. PhD thesis. Universität Hamburg, 2004 (cit. on pp. 5–7).

[42] J. Kronjäger. “Coherent Dynamics of Spinor Bose-Einstein Condensates”. PhD thesis. 2007. DOI: 10.7328/jurpcb/2007228131T5-PhDM4-Citavi (cit. on pp. 5, 7).

[43] C. Becker. “Multi component Bose-Einstein Condensates: From mean field physics to strong correlations”. PhD thesis. Universität Hamburg, 2008, pp. 1–202. ISBN: 978-3868530612. DOI: 10.1.1.427.3541 (cit. on pp. 5, 27, 31).

[44] P. Soltan-Panahi. “Multi–Component Quantum Gases in Hexagonal Lattices”. PhD thesis. Universität Hamburg, 2010 (cit. on pp. 5, 27, 31, 60, 80).

[45] J. Struck. “Artificial Gauge Fields in Driven Optical Lattices”. PhD thesis. Universität Hamburg, 2013. ISBN: 978-3-8439-1327-0 (cit. on pp. 5, 27, 31).

[46] M. Weinberg. “Band structure engineering of ultracold quantum gases in optical lattices”. PhD thesis. Hamburg: Universität Hamburg, 2015. ISBN: 978-3-8439-1968-5 (cit. on pp. 5, 27, 31, 33, 50, 87).

[47] C. Ölschläger. “Floquet Engineering of Bloch Bands in Shaken Optical Lattices”. PhD thesis. Universität Hamburg, 2016 (cit. on pp. 5, 27, 31, 53, 54).

[48] R. Dinter. “Aufbau und Simulierung einer Magnetfalle zur simultanen Speicherung von K-40 und R-87”. PhD thesis. Univerität Hamburg, 2004 (cit. on p. 6).

[49] M. Erhard et al. “Measurement of a mixed-spin-channel Feshbach resonance in Rb87”. In: *Physical Review A* 69.3 (2004). ISSN: 1050-2947. DOI: 10.1103/PhysRevA.69.032705M4-Citavi (cit. on p. 7).

[50] P. D. Lett et al. “Observation of atoms laser cooled below the doppler limit”. In: *Physical Review Letters* 61.2 (1988), pp. 169–172. ISSN: 00319007. DOI: 10.1103/PhysRevLett.61.169 (cit. on p. 8).

[51] J. Dalibard and C. Cohen-Tannoudji. “Laser cooling below the Doppler limit by polarization gradients: simple theoretical models”. In: *Journal of the Optical Society of America B* 6.11 (1989), p. 2023. ISSN: 0740-3224. DOI: 10.1364/JOSAB.6.002023 (cit. on p. 8).

[52] M. Weidemüller et al. “A Novel Scheme for Efficient Cooling below the Photon Recoil Limit”. In: *Europhysics Letters (EPL)* 27.2 (1994), pp. 109–114. ISSN: 0295-5075. DOI: 10.1209/0295-5075/27/2/006 (cit. on p. 8).

[53] G. Grynberg and J.-Y. Courtois. “Proposal for a Magneto-Optical Lattice for Trapping Atoms in Nearly-Dark States”. In: *Europhysics Letters (EPL)* 27.1 (1994), pp. 41–46. ISSN: 0295-5075. DOI: 10.1209/0295-5075/27/1/008 (cit. on pp. 8, 27).

[54] D. Boiron et al. “Three-dimensional cooling of cesium atoms in four-beam gray optical molasses”. In: *Physical Review A* 52.5 (1995), R3425–R3428. ISSN: 1050-2947. DOI: 10.1103/PhysRevA.52.R3425 (cit. on p. 8).

[55] T. Esslinger et al. “Purely optical dark lattice”. In: *Optics Letters* 21.13 (1996), p. 991. ISSN: 0146-9592. DOI: 10.1364/OL.21.000991 (cit. on p. 8).

[56] Q. Bouton et al. “Fast production of Bose-Einstein condensates of metastable helium”. In: *Physical Review A* 91.6 (2015), p. 061402. ISSN: 1050-2947. DOI: 10.1103/PhysRevA.91.061402. arXiv: arXiv:1504.06197v1 (cit. on p. 8).

[57] A. Burchianti et al. “Efficient all-optical production of large Li6 quantum gases using D1 gray-molass”. In: *Physical Review A* 90.4 (2014), p. 043408. ISSN: 1050-2947. DOI: 10.1103/PhysRevA.90.043408 (cit. on p. 8).

[58] F. Sievers et al. “Simultaneous sub-Doppler laser cooling of fermionic Li6 and K40 on the D1 line: Theory and experiment”. In: *Physical Review A* 91.2 (2015), p. 023426. ISSN: 1050-2947. DOI: 10.1103/PhysRevA.91.023426 (cit. on p. 8).

[59] A. T. Grier et al. “Λ-enhanced sub-Doppler cooling of lithium atoms in D1 gray molasses”. In: *Physical Review A* 87.6 (2013), p. 063411. ISSN: 1050-2947. DOI: 10.1103/PhysRevA.87.063411. arXiv: 1304.6971 (cit. on p. 8).

[60] D. Nath et al. “Quantum-interference-enhanced deep sub-Doppler cooling of 39K atoms in gray molasses”. In: *Physical Review A* 88.5 (2013), p. 053407. ISSN: 1050-2947. DOI: 10.1103/PhysRevA.88.053407 (cit. on p. 8).

[61] G. Salomon et al. “Gray-molasses cooling of 39 K to a high phase-space density”. In: *EPL (Europhysics Letters)* 104.6 (2013), p. 63002. ISSN: 0295-5075. DOI: 10.1209/0295-5075/104/63002 (cit. on p. 8).

[62] D. Rio Fernandes et al. "Sub-Doppler laser cooling of fermionic 40 K atoms in three-dimensional gray optical molasses". In: *EPL (Europhysics Letters)* 100.6 (2012), p. 63001. ISSN: 0295-5075. DOI: 10.1209/0295-5075/100/63001 (cit. on p. 8).

[63] H.-Z. Chen et al. "Production of large 41 K Bose-Einstein condensates using D 1 gray molasses". In: *PHYSICAL REVIEW A* 94 (2016), p. 33408. DOI: 10.1103/PhysRevA.94.033408 (cit. on p. 8).

[64] S. Rosi et al. "Λ-enhanced grey molasses on the D2 transition of Rubidium-87 atoms". In: *Scientific Reports* 8.1 (2018), p. 1301. ISSN: 2045-2322. DOI: 10.1038/s41598-018-19814-z (cit. on pp. 8, 10, 11, 13).

[65] R. Conrad. *Graue Melasse für ultrakaltes Rubidium*. 2020 (cit. on p. 8).

[66] G. Janik, W. Nagourney, and H. Dehmelt. "Doppler-free optical spectroscopy on the Baˆ+ mono-ion oscillator". In: *Journal of the Optical Society of America B* 2.8 (1985), p. 1251. ISSN: 0740-3224. DOI: 10.1364/JOSAB.2.001251 (cit. on p. 8).

[67] B. Lounis and C. Cohen-Tannoudji. "Coherent population trapping and Fano profiles". In: *Journal de Physique II* 2.4 (1992), pp. 579–592. ISSN: 1155-4312. DOI: 10.1051/jp2:1992153 (cit. on pp. 8, 9).

[68] F. Bardou et al. *Levy Statistics and Laser Cooling*. Cambridge: Cambridge University Press, 2002. ISBN: 9780511755668. DOI: 10.1017/CBO9780511755668 (cit. on p. 9).

[69] A. T. Grier et al. "Λ-enhanced sub-Doppler cooling of lithium atoms in D1 gray molasses". In: *Physical Review A* 87.6 (2013), p. 063411. ISSN: 1050-2947. DOI: 10.1103/PhysRevA.87.063411 (cit. on p. 9).

[70] D. A. Steck. "Rubidium 87 D Line Data". 2019 (cit. on p. 11).

[71] G. Salomon. "All optical 39K BEC : a quantum gas with tunable interactions to study disorder physics in low dimensions". PhD thesis. Institut d'Optique Graduate School, 2014 (cit. on p. 13).

[72] I. Bloch. "Quantum coherence and entanglement with ultracold atoms in optical lattices". In: *Nature* 453.7198 (2008), pp. 1016–1022. ISSN: 0028-0836. DOI: 10.1038/nature07126 (cit. on p. 14).

[73] J. Kronjäger et al. "Spontaneous Pattern Formation in an Antiferromagnetic Quantum Gas". In: *Physical Review Letters* 105.9 (2010), p. 090402. ISSN: 0031-9007. DOI: 10.1103/PhysRevLett.105.090402 (cit. on p. 14).

[74] D. M. Stamper-Kurn and M. Ueda. "Spinor Bose gases: Symmetries, magnetism, and quantum dynamics". In: *Reviews of Modern Physics* 85.3 (2013), pp. 1191–1244. ISSN: 0034-6861. DOI: 10.1103/RevModPhys.85.1191 (cit. on p. 14).

[75] A. D. Ludlow et al. "Optical atomic clocks". In: *Reviews of Modern Physics* 87.2 (2015), pp. 637–701. ISSN: 0034-6861. DOI: 10.1103/RevModPhys.87.637 (cit. on p. 14).

[76] A. Mager. "Magnetic shields". In: *IEEE Transactions on Magnetics* 6.1 (1970), pp. 67–75. ISSN: 0018-9464. DOI: 10.1109/TMAG.1970.1066714 (cit. on p. 14).

[77] T. J. Sumner, J. M. Pendlebury, and K. F. Smith. "Convectional magnetic shielding". In: *Journal of Physics D: Applied Physics* 20.9 (1987), pp. 1095–1101. ISSN: 0022-3727. DOI: 10.1088/0022-3727/20/9/001 (cit. on p. 14).

[78] E. Baum and J. Bork. "Systematic design of magnetic shields". In: *Journal of Magnetism and Magnetic Materials* 101.1-3 (1991), pp. 69–74. ISSN: 03048853. DOI: 10.1016/0304-8853(91)90682-Z (cit. on p. 14).

[79] R Wynands and S Weyers. "Atomic fountain clocks". In: *Metrologia* 42.3 (2005), S64–S79. ISSN: 0026-1394. DOI: 10.1088/0026-1394/42/3/S08 (cit. on p. 14).

[80] C. J. Dedman et al. "Active cancellation of stray magnetic fields in a Bose-Einstein condensation experiment". In: *Review of Scientific Instruments* 78.2 (2007), p. 024703. ISSN: 0034-6748. DOI: 10.1063/1.2472600 (cit. on p. 15).

[81] M Skakala, V Zrubec, and J Manka. "Active compensation for ambient magnetic noise in the unshielded environment". In: *Measurement Science and Technology* 4.4 (1993), p. 468. DOI: 10.1088/0957-0233/4/4/005 (cit. on p. 15).

[82] S. J. Seltzer and M. V. Romalis. "Unshielded three-axis vector operation of a spin-exchange-relaxation-free atomic magnetometer". In: *Applied Physics Letters* 85.20 (2004), pp. 4804–4806. ISSN: 0003-6951. DOI: 10.1063/1.1814434 (cit. on p. 15).

[83] J. Belfi et al. "Stray magnetic field compensation with a scalar atomic magnetometer". In: *Review of Scientific Instruments* 81.6 (2010), p. 065103. ISSN: 0034-6748. DOI: 10.1063/1.3441980 (cit. on p. 15).

[84] D. Spemann et al. "Active compensation of stray magnetic fields at LIPSION". In: *Nuclear Instruments and Methods in Physics Research Section B: Beam Interactions with Materials and Atoms* 210 (2003), pp. 79–84. ISSN: 0168583X. DOI: 10.1016/S0168-583X(03)01027-9 (cit. on p. 15).

[85] D. Budker and M. Romalis. "Optical magnetometry". In: *Nature Physics* 3.4 (2007), pp. 227–234. ISSN: 1745-2473. DOI: 10.1038/nphys566 (cit. on p. 15).

[86] N. F. Ramsey. "Experiments with separated oscillatory fields and hydrogen masers". In: *Reviews of Modern Physics* 62.3 (1990), pp. 541–552. ISSN: 0034-6861. DOI: 10.1103/RevModPhys.62.541M4-Citavi (cit. on pp. 15, 18).

[87] T. Klafka. *Towards active magnetic field compensation for ultracold atom experiments*. 2016 (cit. on pp. 15, 55).

[88] J. Seeger. *Aktive Magnetfeldkompensation und Magnetometrie in Quantengasexperimenten*. 2017 (cit. on pp. 15, 23).

[89] Honeywell. *Datasheet HMC 1001 1- and 2-Axis Magnetic Sensors (900248 Rev. B)*. Tech. rep. (cit. on p. 17).

[90] S. Wildermuth et al. "Sensing electric and magnetic fields with Bose-Einstein condensates". In: *Applied Physics Letters* 88.26 (2006), p. 264103. ISSN: 0003-6951. DOI: 10.1063/1.2216932 (cit. on p. 18).

[91] M. Vengalattore et al. "High-Resolution Magnetometry with a Spinor Bose-Einstein Condensate". In: *Physical Review Letters* 98.20 (2007), p. 200801. ISSN: 0031-9007. DOI: 10.1103/PhysRevLett.98.200801 (cit. on p. 18).

[92] D. Ramírez Muñoz et al. "Temperature compensation of Wheatstone bridge magnetoresistive sensors based on generalized impedance converter with input reference current". In: *Review of Scientific Instruments* 77.10 (2006), p. 105102. ISSN: 0034-6748. DOI: 10.1063/1.2358696 (cit. on p. 20).

[93] R. Grimm, M. Weidemüller, and Y. B. Ovchinnikov. "Optical Dipole Traps for Neutral Atoms". In: 2000, pp. 95–170. DOI: 10.1016/S1049-250X(08)60186-X (cit. on p. 27).

[94] J. Dalibard and C. Cohen-Tannoudji. "Dressed-atom approach to atomic motion in laser light: the dipole force revisited". In: *Journal of the Optical Society of America B* 2.11 (1985), p. 1707. ISSN: 0740-3224. DOI: 10.1364/JOSAB.2.001707 (cit. on p. 27).

[95] R. Dubessy et al. "Imaging the collective excitations of an ultracold gas using statistical correlations". In: *New Journal of Physics* 16.12 (2014), p. 122001. ISSN: 1367-2630. DOI: 10.1088/1367-2630/16/12/122001 (cit. on pp. 31, 87).

[96] N. W. Ashcroft and N. D. Mermin. *Solid state physics*. College ed. Melbourne South: Brooks/Cole Thomson Learning, 2005, p. 826. ISBN: 0-03-083993-9 (cit. on p. 34).

[97] R. Gross. *Festkörperphysik*. 2nd. Berlin/Boston: Walter de Gruyter GmbH, 2018, p. 340 (cit. on p. 34).

[98] H. Moritz et al. "Exciting Collective Oscillations in a Trapped 1D Gas". In: *Physical Review Letters* 91.25 (2003), p. 250402. ISSN: 0031-9007. DOI: 10.1103/PhysRevLett.91.250402 (cit. on pp. 37, 77).

[99] F. Gerbier et al. "Expansion of a Quantum Gas Released from an Optical Lattice". In: *Physical Review Letters* 101.15 (2008), p. 155303. ISSN: 0031-9007. DOI: 10.1103/PhysRevLett.101.155303 (cit. on pp. 38, 39, 65).

[100] S. Trotzky et al. "Suppression of the critical temperature for superfluidity near the Mott transition". In: *Nature Physics* 6.12 (2010), pp. 998–1004. ISSN: 1745-2473. DOI: 10.1038/nphys1799 (cit. on pp. 38, 56, 64).

[101] H. Cayla et al. "Single-atom-resolved probing of lattice gases in momentum space". In: *Physical Review A* 97.6 (2018), p. 061609. ISSN: 2469-9926. DOI: 10.1103/PhysRevA.97.061609 (cit. on pp. 38, 64).

[102] J. Struck et al. "Quantum Simulation of Frustrated Classical Magnetism in Triangular Optical Lattices". In: *Science* 333.6045 (2011), pp. 996–999. ISSN: 0036-8075. DOI: 10.1126/science.1207239 (cit. on p. 40).

[103] B. Gadway et al. "Analysis of Kapitza-Dirac diffraction patterns beyond the Raman-Nath regime". In: *Optics Express* 17.21 (2009), p. 19173. ISSN: 1094-4087. DOI: 10.1364/OE.17.019173 (cit. on p. 42).

[104] X. Zhou, S. Jin, and J. Schmiedmayer. "Shortcut loading a Bose–Einstein condensate into an optical lattice". In: *New Journal of Physics* 20.5 (2018), p. 055005. ISSN: 1367-2630. DOI: 10.1088/1367-2630/aac11b (cit. on pp. 42, 61).

[105] A. Kerkmann. "A novel apparatus for quantum gas microscopy of lithium atomsitle". PhD thesis. Universität Hamburg, 2019, p. 109 (cit. on p. 44).

[106] D. Vogel. "Measuring Geometry and Topology of Floquet-Bloch States in and out of Equilibrium with ultracold fermions Dissertation". PhD thesis. Universität Hamburg, 2018 (cit. on p. 44).

[107] R. Yamamoto et al. "Single-site-resolved imaging of ultracold atoms in a triangular optical lattice". In: *New Journal of Physics* 22.12 (2020), p. 123028. ISSN: 1367-2630. DOI: 10.1088/1367-2630/abcdc8 (cit. on pp. 45, 79).

[108] J. Yang et al. "Site-resolved imaging of ultracold fermions in a triangular-lattice quantum gas microscope". In: (2021). arXiv: 2102.11862 (cit. on pp. 45, 79).

[109] S. Blatt et al. "Low-noise optical lattices for ultracold Li6". In: *Physical Review A* 92.2 (2015), p. 021402. ISSN: 1050-2947. DOI: 10.1103/PhysRevA.92.021402 (cit. on p. 45).

[110] L. Asteria et al. "Quantum gas magnifier for sub-lattice-resolved imaging of three-dimensional quantum systems". In: (2021). arXiv: 2104.10089 (cit. on pp. 45, 64, 79).

[111] J. H. Denschlag et al. "A Bose-Einstein condensate in an optical lattice". In: *Journal of Physics B: Atomic, Molecular and Optical Physics* 35.14 (2002), p. 307. ISSN: 09534075. DOI: 10.1088/0953-4075/35/14/307 (cit. on p. 49).

[112] M. C. Fischer et al. "Observation of Rabi oscillations between Bloch bands in an optical potential". In: *Physical Review A* 58.4 (1998), R2648–R2651. ISSN: 1050-2947. DOI: 10.1103/PhysRevA.58.R2648 (cit. on p. 49).

[113] M. Ölschläger et al. "Topologically Induced Avoided Band Crossing in an Optical Checkerboard Lattice". In: *Physical Review Letters* 108.7 (2012), p. 075302. ISSN: 0031-9007. DOI: 10.1103/PhysRevLett.108.075302 (cit. on pp. 51, 73).

[114] M. Ben Dahan et al. "Bloch Oscillations of Atoms in an Optical Potential". In: *Physical Review Letters* 76.24 (1996), pp. 4508–4511. ISSN: 0031-9007. DOI: 10.1103/PhysRevLett.76.4508 (cit. on p. 51).

[115] O. Morsch et al. "Bloch Oscillations and Mean-Field Effects of Bose-Einstein Condensates in 1D Optical Lattices". In: *Physical Review Letters* 87.14 (2001), p. 140402. ISSN: 0031-9007. DOI: 10.1103/PhysRevLett.87.140402 (cit. on p. 51).

[116] M Cristiani et al. "Experimental properties of Bose-Einstein condensates in one-dimensional optical lattices: Bloch oscillations, Landau-Zener tunneling, and mean-field effects". In: *Physical Review A* 65.6 (2002), p. 063612. ISSN: 1050-2947. DOI: 10.1103/PhysRevA.65.063612 (cit. on p. 51).

[117] S. Kling et al. "Atomic Bloch-Zener Oscillations and Stückelberg Interferometry in Optical Lattices". In: *Physical Review Letters* 105.21 (2010), p. 215301. ISSN: 0031-9007. DOI: 10.1103/PhysRevLett.105.215301 (cit. on p. 51).

[118] T. Li et al. "Bloch state tomography using Wilson lines". In: *Science* 352.6289 (2016), pp. 1094–1097. ISSN: 0036-8075. DOI: 10.1126/science.aad5812. arXiv: 1509.02185 (cit. on p. 51).

[119] M. Neundorf. *Floquet Engineering of Frustrated Spin Models in Optical Lattices*. 2018 (cit. on p. 54).

[120] L. Pitaevskii and S. Stringari. *Bose-Einstein Condensation*. Oxford University Press, 2003, p. 382. ISBN: 978-0-19-850719-2 (cit. on pp. 56, 77).

[121] P. B. Blakie and J. V. Porto. "Adiabatic loading of bosons into optical lattices". In: *Physical Review A* 69.1 (2004), p. 013603. ISSN: 1050-2947. DOI: 10.1103/PhysRevA.69.013603 (cit. on p. 56).

[122] F. Gerbier. "Boson Mott Insulators at Finite Temperatures". In: *Physical Review Letters* 99.12 (2007), p. 120405. ISSN: 0031-9007. DOI: 10.1103/PhysRevLett.99.120405 (cit. on p. 56).

[123] L. Pollet et al. "Temperature changes when adiabatically ramping up an optical lattice". In: *New Journal of Physics* 10.6 (2008), p. 065001. ISSN: 1367-2630. DOI: 10.1088/1367-2630/10/6/065001 (cit. on p. 56).

[124] J. Zakrzewski and D. Delande. "Breakdown of adiabaticity when loading ultracold atoms in optical lattices". In: *Physical Review A* 80.1 (2009), p. 013602. ISSN: 1050-2947. DOI: 10.1103/PhysRevA.80.013602 (cit. on p. 56).

[125] J. Wernsdorfer, M. Snoek, and W. Hofstetter. "Lattice-ramp-induced dynamics in an interacting Bose-Bose mixture". In: *Physical Review A* 81.4 (2010), p. 043620. ISSN: 1050-2947. DOI: 10.1103/PhysRevA.81.043620 (cit. on p. 56).

[126] T. Gericke et al. "Adiabatic loading of a Bose–Einstein condensate in a 3D optical lattice". In: *Journal of Modern Optics* 54.5 (2007), pp. 735–743. ISSN: 0950-0340. DOI: 10.1080/09500340600777730 (cit. on p. 56).

[127] D. McKay, M. White, and B. DeMarco. "Lattice thermodynamics for ultracold atoms". In: *Physical Review A* 79.6 (2009), p. 063605. ISSN: 1050-2947. DOI: 10.1103/PhysRevA.79.063605 (cit. on p. 56).

[128] C. Carcy et al. “Certifying the Adiabatic Preparation of Ultracold Lattice Bosons in the Vicinity of the Mott Transition”. In: *Physical Review Letters* 126.4 (2021), p. 045301. ISSN: 0031-9007. DOI: 10.1103/PhysRevLett.126.045301 (cit. on p. 56).

[129] L. Niu et al. “Observation of a Dynamical Sliding Phase Superfluid with P-Band Bosons”. In: *Physical Review Letters* 121.26 (2018), p. 265301. ISSN: 0031-9007. DOI: 10.1103/PhysRevLett.121.265301 (cit. on p. 62).

[130] T. Zhou et al. “Dimension Crossing Turbulent Cascade in an Excited Lattice Bose Gas”. In: (2019). arXiv: 1912.13252 (cit. on p. 62).

[131] D. Hu et al. “Ramsey interferometry with trapped motional quantum states”. In: *Communications Physics* 1.1 (2018), p. 29. ISSN: 2399-3650. DOI: 10.1038/s42005-018-0030-7 (cit. on p. 62).

[132] P. Groß. *Design of a Hybrid Trap for Ultracold Rubidium*. University of Hamburg, 2020 (cit. on p. 62).

[133] F. Gerbier et al. “Phase Coherence of an Atomic Mott Insulator”. In: *Physical Review Letters* 95.5 (2005), p. 050404. ISSN: 0031-9007. DOI: 10.1103/PhysRevLett.95.050404 (cit. on pp. 64, 93).

[134] V. Sharma, S. Choudhury, and E. J. Mueller. “Dynamics of Bose-Einstein recondensation in higher bands”. In: *Physical Review A* 101.3 (2020), p. 033609. ISSN: 2469-9926. DOI: 10.1103/PhysRevA.101.033609 (cit. on p. 73).

[135] K. V. Kheruntsyan et al. “Finite-temperature correlations and density profiles of an inhomogeneous interacting one-dimensional Bose gas”. In: *Physical Review A* 71.5 (2005), p. 053615. ISSN: 1050-2947. DOI: 10.1103/PhysRevA.71.053615 (cit. on p. 76).

[136] D. S. Petrov, G. V. Shlyapnikov, and J. T. M. Walraven. “Regimes of Quantum Degeneracy in Trapped 1D Gases”. In: *Physical Review Letters* 85.18 (2000), pp. 3745–3749. ISSN: 0031-9007. DOI: 10.1103/PhysRevLett.85.3745 (cit. on p. 76).

[137] B. Paredes et al. “Tonks–Girardeau gas of ultracold atoms in an optical lattice”. In: *Nature* 429.6989 (2004), pp. 277–281. ISSN: 0028-0836. DOI: 10.1038/nature02530 (cit. on p. 77).

[138] T. Kinoshita. “Observation of a One-Dimensional Tonks-Girardeau Gas”. In: *Science* 305.5687 (2004), pp. 1125–1128. ISSN: 0036-8075. DOI: 10.1126/science.1100700 (cit. on p. 77).

[139] N Fabbri et al. “Energy and momentum transfer in one-dimensional trapped gases by stimulated light scattering”. In: *New Journal of Physics* 17.6 (2015), p. 063012. ISSN: 1367-2630. DOI: 10.1088/1367-2630/17/6/063012 (cit. on p. 77).

[140] M. A. Cazalilla et al. “One dimensional bosons: From condensed matter systems to ultracold gases”. In: *Reviews of Modern Physics* 83.4 (2011), pp. 1405–1466. ISSN: 0034-6861. DOI: `10.1103/RevModPhys.83.1405`. arXiv: `1101.5337` (cit. on p. 77).

[141] J. Heinze et al. “Intrinsic Photoconductivity of Ultracold Fermions in Optical Lattices”. In: *Physical Review Letters* 110.8 (2013), p. 085302. ISSN: 0031-9007. DOI: `10.1103/PhysRevLett.110.085302` (cit. on p. 83).

[142] A. Khan. *Design und Aufbau eines kompakten Lasersystems zur Kühlung von Rubidium-87*. Hamburg, 2020 (cit. on p. 83).

[143] I. T. Jolliffe and J. Cadima. “Principal component analysis: a review and recent developments”. In: *Philosophical Transactions of the Royal Society A: Mathematical, Physical and Engineering Sciences* 374.2065 (2016), p. 20150202. ISSN: 1364-503X. DOI: `10.1098/rsta.2015.0202` (cit. on p. 87).

[144] S. R. Segal et al. “Revealing buried information: Statistical processing techniques for ultracold-gas image analysis”. In: *Physical Review A* 81.5 (2010), p. 053601. ISSN: 1050-2947. DOI: `10.1103/PhysRevA.81.053601` (cit. on p. 87).

[145] I. Jolliffe. *Principal Component Analysis*. 2nd Editio. Springer Series in Statistics. New York: Springer-Verlag, 2002. ISBN: 0-387-95442-2. DOI: `10.1007/b98835` (cit. on p. 87).

Acknowledgements

Throughout this PhD project I have received an immense amount of support by a large number of people, to whom I would like to express my gratitude.

First of all I would like to thank my supervisor Klaus Sengstock for his continuous support and expertise. I am also extremely grateful to him for providing such an inspiring research environment, for the profound confidence in my work and for his empathetic nature. I would like to extend my sincere thanks to Andreas Hemmerich for the evaluation of this thesis and stimulating discussions within the SFB C1-project. Many thanks also to Ulrike Frühling for the guidance within the graduate school of the SFB.

I would like to express my deepest gratitude to Juliette Simonet. Her constant support and immense optimism have had a huge impact on the success of this thesis. I would like to especially thank her for the constructive feedback on this thesis.

I gratefully acknowledge the work at the experiment with my fellow PhD student Alexander Ilin. It has been a great privilege and joy to work with Alexander. I am still impressed by his drive to understand and solve mathematical and experimental questions. Moreover, I am very happy that Julia Bergmann has begun her PhD at our project. I am looking forward to exciting times in the lab and passing on the secrets of the quantum gas machine. Further I would like to thank our bachelor's and master's students David Nak, Ruven Conrad, Amir Khan, Mario Großmann and Phillip Groß.

I am also grateful for the insights into the art of theory within our collaboration with Peter Schmelcher, Simos Mistakidis and Georgios Koutentakis. Their immense passion for numerous calculations and explanations have been more than impressive.

Thanks to all the YAO organizers for the fun times and all members of the research group for an extremely enjoyable and friendly working atmosphere.

Last but not least, I am deeply grateful for the unconditional support of my wife, family and friends.

Eidesstattliche Erklärung

Hiermit versichere ich an Eides statt, die vorliegende Dissertationsschrift selbst verfasst und keine anderen als die angegebenen Hilfsmittel und Quellen benutzt zu haben.

Hamburg, den

Unterschrift: